AFGL-TR-88-0293

EXCITATION AND DIAGNOSTICS OF OPTICAL CONTAMINATION IN THE SPACECRAFT ENVIRONMENT

I. L. Kofsky
J. L. Barrett
T. E. Brownrigg
P. N. McNicholl
N. H. Tran
C. A. Trowbridge

PhotoMetrics, Inc.
4 Arrow Drive
Woburn, MA 01801-2057

01 July 1988

Final Report
13 August 1985-30 June 1988

Approved for public release; distribution unlimited.

AIR FORCE GEOPHYSICS LABORATORY
AIR FORCE SYSTEMS COMMAND
UNITED STATES AIR FORCE
HANSCOM AFB, MASSACHUSETTS 01731-5000

UNCLASSIFIED
SECURITY CLASSIFICATION OF THIS PAGE

AD-A202 429

REPORT DOCUMENTATION PAGE

1a. REPORT SECURITY CLASSIFICATION Unclassified	1b. RESTRICTIVE MARKINGS
2a. SECURITY CLASSIFICATION AUTHORITY N/A since Unclassified	3. DISTRIBUTION/AVAILABILITY OF REPORT Approved for public release; distribution unlimited.
2b. DECLASSIFICATION/DOWNGRADING SCHEDULE N/A since Unclassified	
4. PERFORMING ORGANIZATION REPORT NUMBER(S) PhM-88-06	5. MONITORING ORGANIZATION REPORT NUMBER(S) AFGL-TR-88-0293
6a. NAME OF PERFORMING ORGANIZATION PhotoMetrics, Inc. — 6b. OFFICE SYMBOL (If applicable)	7a. NAME OF MONITORING ORGANIZATION Air Force Geophysics Laboratory
6c. ADDRESS (City, State, and ZIP Code) 4 Arrow Drive Woburn, MA 01801	7b. ADDRESS (City, State, and ZIP Code) Hanscom AFB, MA 01731-5000
8a. NAME OF FUNDING/SPONSORING ORGANIZATION — 8b. OFFICE SYMBOL (If applicable)	9. PROCUREMENT INSTRUMENT IDENTIFICATION NUMBER F19628-85-C-0148
8c. ADDRESS (City, State, and ZIP Code)	10. SOURCE OF FUNDING NUMBERS

PROGRAM ELEMENT NO.	PROJECT NO.	TASK NO.	WORK UNIT ACCESSION NO.
62101F	7661	11	AK

11. TITLE (Include Security Classification)
EXCITATION AND DIAGNOSTICS OF OPTICAL CONTAMINATION IN THE SPACECRAFT ENVIRONMENT

12. PERSONAL AUTHOR(S)
Kofsky, I.L., Barrett, J.L., Brownrigg, T.E., McNicholl, P.N., Tran, N.H., and Trowbridge, C.A.

13a. TYPE OF REPORT	13b. TIME COVERED	14. DATE OF REPORT (Year, Month, Day)	15. PAGE COUNT
Final Technical	FROM 850813 TO 880630	880701	156

16. SUPPLEMENTARY NOTATION

17. COSATI CODES			18. SUBJECT TERMS (Continue on reverse if necessary and identify by block number)	
FIELD	GROUP	SUB-GROUP	Spacecraft Glow,	Excitative Recombination,
			Surface Chemistry,	Photometry and Radiometry,
			Optical Contamination,	Chemical Kinetics. (TR-5)

19. ABSTRACT (Continue on reverse if necessary and identify by block number)

The ultraviolet and infrared contaminant glows produced by spacecraft traversing the thermosphere are identified and their spatial extents and brightnesses estimated from laboratory reaction-rate data, in support of planning of systematic spectroradiometric measurements from space shuttle. A formalism is developed for calculating radiances and irradiances of the emissions from metastable molecules formed at vehicle surfaces exposed to the atmosphere, which serves in selecting the view projections and angular fields of optical sensors. The principal ultraviolet features expected from surface-catalyzed desorptive recombination of ambient species are the Herzberg I ($A \rightarrow X$) bands of O_2 (which extend into the blue); the β ($B \rightarrow X$) bands of NO; and the Lyman-Birge-Hopfield ($a \rightarrow X$) bands of N_2, which have in fact been observed from at least one airglow- and aurora-characterizing satellite in low earth orbit and whose excitation and spectroscopy are treated in detail. The infrared features predicted to have the highest brightnesses are the pseudocontinuous electronic band systems of NO_2 that extend above 0.8 μm and the ensuing rovibrational-bands

20. DISTRIBUTION/AVAILABILITY OF ABSTRACT	21. ABSTRACT SECURITY CLASSIFICATION
☐ UNCLASSIFIED/UNLIMITED ☐ SAME AS RPT ☐ DTIC USERS	Unclassified

22a. NAME OF RESPONSIBLE INDIVIDUAL	22b. TELEPHONE (Include Area Code)	22c. OFFICE SYMBOL
Edmund Murad		AFGL/PHK

DD FORM 1473, 84 MAR — 83 APR edition may be used until exhausted. All other editions are obsolete.

SECURITY CLASSIFICATION OF THIS PAGE
UNCLASSIFIED

19. ABSTRACT (continued)

cascade. A similar cascade from NO(X, v>0) would also produce short- and medium-wavelength infrared photons, from a volume extending considerably farther from the ram-exposed vehicle surfaces. In addition some recombination radiation in the N_2 Wu-Benesch (W→B) system may be expected, originating from essentially the same near-surface volume as the NO_2 electronic and N_2 (a→X) bands. The principal ultraviolet and visible emission that would result from excitative reactions with atmospheric species of the most abundant combustion products from shuttle's control rocket engines are identified from the exothermicities, spectroscopic selection rules, radiative lifetimes, and available thermochemical-molecular beam interactions data. The cross sections for atom-exchange reactions with O are estimated from the interpreted laboratory data base (no similar information is available for N_2) and compared with the predicted cross sections for elastic scattering, which co-determine the photon yields in and spectral extents of UV-visible glows excited by the high-directed kinetic energy rocket exhaust. In support of the analysis and interpretation of infrared images of a rocket exhaust plume taken with a groundbased telescope, expected spectral distributions of the hot plume gas, radiances of the calibrating hard body in the field of view, and transmission of the intervening atmosphere are calculated.

FOREWORD

This report describes PhotoMetrics' work for the Spacecraft Interactions Branch of Air Force Geophysics Laboratory in characterizing spacebased experiment- and surveillance-degrading optical emissions from and near low altitude satellites and suborbital vehicles, in the period August 1985 - May 1988. An overview of the topics covered appears in Section 1 (the journal articles published and presentations made during the program are listed in Table 1.1). Sections 2-4 predict the spacecraft passage-induced optical contamination at ultraviolet and infrared wavelengths, for which little observational data are currently available; Section 5 derives brightness distributions of these glow volumes from the transport and radiative properties of the emitting species, for application in forthcoming measurement programs; Section 6 reviews the information available on the electronic-bands glows excited in collisions of the energetic exhaust gases from rocket engines with the atmosphere, and identifies the principal expected transitions; and Section 7 archives the results of calculations of spectral emission/scattering/atmosphere transmission made in support of an AFGL analysis of groundbased measurements of the infrared radiances from a space shuttle exhaust plume.

PhotoMetrics also contributed to several related AFGL projects in spacecraft survivability; this work was largely administrative, with its immediate results communicated in quarterly program reports. The principal such task was the determination of pointing directions of shuttle-based photographic cameras that documented natural energetic-particle precipitation into the atmosphere (the Auroral Photography Experiment), on the basis of positions of known stars within their image fields. A further task was a critical analysis of the performance of the initial configurations of a multichannel camera-spectrograph, in diagnosing spacecraft-induced, chemical-

release, and earth-limb glows at UV-visible-near IR wavelengths, as part of AFGL's design reviews of this instrument. This work led to major changes in the optical systems of this [Arizona] Imager/Spectrograph as well as an improved understanding of the signal/noise ratios that it can be expected to provide. In connection with applying this instrument for remote sensing from space shuttle and free-flying subsatellite platforms, where it will operate in conjunction with a high-performance infrared spectrometer and radiometer array, PhotoMetrics participated in working groups responsible for planning the overall experiment mission.

The authors express their thanks to Ms. C. Griffin for typing the manuscript and contributing to the preparation of its illustrations and tables. The support and encouragement of E. Murad, C. Pike, and W. Denig of AFGL/PHK branch is gratefully acknowledged.

TABLE OF CONTENTS

LIST OF TABLES

TABLE (Continued) PAGE

LIST OF ILLUSTRATIONS

FIGURE PAGE

SECTION 1

INTRODUCTION AND OVERVIEW

Background

Visible and near-ultraviolet glows with radiances comparable with that of the natural nightglow from the upper atmosphere's limb have been found in the last few years to extend from the ram-directed surfaces of satellites in low earth orbits (as reviewed in Ref's 1-3). These emissions appear to be a general property of spacecraft moving through the thermosphere and, by inference, of exo-reentry and launch vehicles also. This "foreground" optical contamination would have the effect of reducing the signal/noise ratios achievable by spaceborne surveillance sensors, as well as of measurements from onboard of the atmospheric and astronomical backgrounds. In addition, since their spectral intensities vary with the composition (Ref 4) and perhaps temperature (Ref 5) of the exposed outer-surface material--at least at visible wavelengths, where the most data are available--these glows have potential to provide a technical basis for remote optical discrimination among orbiting satellites and ballistic missiles.

This report summarizes PhotoMetrics' work in interpreting the information available on these spacecraft-induced glows, and in predicting their emission spectra and absolute intensities at wavelengths where the data--most of which was taken as an offshoot of airglow-characterization experiments--are sparse or non-existent. A principal purpose of this effort is to help plan systematic glow measurements with a set of spectrometers and diode array cameras sensitive from the vacuum ultraviolet through the mid-wavelength infrared (including the specially-designed Arizona Imager/Spectrograph, now being constructed for USAF), in space shuttle missions.

The report in addition addresses (in final Sections 6) a further major issue of spacecraft optical contamination and

signatures, that of the UV, visible, and infrared chemiluminescence excited when the energetic exhaust gases from the rocket engines that control the aspect and trajectory of space vehicles impact on the ambient low-density air. The chemical processes producing electronic-bands radiation differ from those responsible for spacecraft-induced glows, in that the reactions of interest are endothermic by several electron volts--the energy needed to overcome the potential barriers is supplied by the high translational velocities of the orbiting vehicle and the directed exhaust stream--, and involve combustion products as well as ambient aeronomic species.

Spacecraft Glow Literature

Table 1.1 lists the publications on spacecraft glow phenomenology prepared by the authors of this report in connection with, and also prior to, the program reviewed here. These journal articles reference the original field and laboratory data sources, and other approaches to interpreting the observed spectral and spatial distributions of the emissions.

Ref's 6 and 7 provide the initial basis for analyses of glow features at wavelengths shorter and longer than the more easily-accessible visible range, which appear in Sections 2 and 3 respectively. Ref 8 (also from the refereed literature) is the original interpretation of the ultraviolet glow resulting from surface-catalyzed recombination of nitrogen atoms--closely related to the well-known Lewis-Rayleigh afterglow--, which is presented in further detail in Section 4. Ref 1 is a general statement of the hypothesis that most if not all of the off-surface glows represent manifestations of this recombination phenomenon, and contains many of the fundamental ideas explored and quantified in Sections 2-4. Most of the material in Ref 1 was initially reported at a NASA-sponsored conference on glow-producing processes held in May 1985 (see Ref's 9-11), and Ref's 2, 3 and 12 are invited review papers at three other symposiums.

Table 1.1. PhotoMetrics literature publications on spacecraft-induced optical glows

Reference* (date)	Topic	Section
13 (1983) 14 (1984)	Glows from plasmas produced at ram surfaces (no longer judged of critical importance)	---
9-11(1985)	Preliminary to Ref's 1 and 2	---
3 (1986)	Early review of data	---
1 (1986)	General statement of surface-catalyzed excitative recombination	All
7* (1987)	Prediction of IR from NO, NO_2	3
6* (1986)	Prediction of UV glows	2,4
12* (1986)	Overview of phenomenology	---
2* (1987)	Overview of phenomenology	All
8* (1988)	Theory of N_2 Lyman-Birge-Hopfield bands glow	4

*Supported under the program reported here.

Ref's 13 and 14, which predate the program reported here, are largely of historic interest, in that they show that the measured spectral distributions fail to support an early hypothesis of how the visible-near UV glow is excited:--by particle impact in a ~10's-eV off-surface plasma (Ref 15).

Table 1.2 is a listing of the perceivedly highest-radiance glows induced at spacecraft surfaces, both observed and expected, whose properties are reviewed in this report. As is alluded to above, these emissions would arise from chemiluminous recombination reactions of ambient atoms and molecules incident on the windward exposed surfaces of vehicles orbiting in the thermosphere. (The concentrations of one reactive species may be locally enhanced by high-kinetic energy gas collisions; see Section 4.) A further description of this catalytic process appears in Section 2 (and also in Ref 1). The radiations, with the exception of the vibrational cascades from NO and NO_2 (final four entries in Table 1.2), are tabulated in order of increasing emission wavelength (second column). The spatial extents of these glows (third column) are expected to be reasonably accurate provided that the excited species are thermally accommodated with the surface before effusing from it. (This may not always be so; some laboratory counterexamples and a theoretical model of a non-equilibrated desorption mechanism are discussed in Ref 16.) In contrast the radiances in the bands (fourth column) are in general no more than planning estimates, for the reasons explained in this report. (Principally, few probabilities of desorptive electronic excitation from model surfaces have been adequately measured in the laboratory, and even if these were known no guarantee exists that they would be similar under the more chemically contaminated and otherwise much less controlled conditions of space flight.) The final column of Table 1.2 lists the Section in this report in which the phenomenology of the molecular emission feature is reviewed.

Table 1.2. Principal spacecraft surface-catalyzed recombination glows

Band System	Δλ	Spatial Extent*	Radiance**	Comments	Section
N_2 Lyman-Birge-Hopfield (a→X)†	1200-2100 Å	6 cm	2 kR	Strong dependence on altitude unexplained	4
NO Beta (B→X)††	2400-3800 Å	1½ mm	1 kR	Excited at exposed sensor surfaces; A→X, C→X not observed	2
O_2 Herzberg I (A→X)	2500-4900 Å	80 m	2 kR	Other recombinant O_2 states produce weak emission radiances	2
NO_2 pseudocontinuum ($^2B_1$, $^2B_2$→$^2A_1$)†	3900 Å - 2½ μm	5-10 cm	10 kR	"Shuttle glow" from NO + O	(Ref's 1, 17)
N_2 Wu-Benesch (W→B), First Positive B→A††	1 - 3 μm & 5000-11000 Å	4-40 cm (& ¼ cm)	1 kR each	First Positive cascade follows W→B; A→X weak; other recombinant N_2 features weak also	3
NO Δv = 2	2.7 - 3 μm	100 m	½x10^{-13} w/cm^{2}ster	Vibrational cascade follows B→X, v > 0	3
NO Δv = 1	5.3 - 6 μm	100 m	2x10^{-13} w/cm^{2}ster	Same as Δv = 2	
NO_2 $\nu'_1 + \nu'_3$	3.4 - 3.8 μm	2½ m	3x10^{-11} w/cm^{2}ster	Vibrational cascade follows $\tilde{X}$, ν'_1,$\nu'_2\nu'_3$	3
NO_2 ν'_3	6.0 - 6.6 μm	2 m	4x10^{-10} w/cm^{2}ster	Strongest cascade component of NO_2	3

* (mean effusive desorption velocity)·(radiative lifetime of excited upper state). See Sections 2.5.

** Nominal planning estimate, perpendicular projection (see Section 5), complete band system at 225 km orbital altitude.

† Identified from spacecraft. †† possible identification.

Brightness Considerations

In most glow-measurement geometries the observable is surface radiance, which is proportional to the number of emission events per unit time within columns directed along the optic axis of the radiometer or spectrometer. This quantity depends not only on the rate at which the upper state of the radiative transition is populated, but also on the lifetime in this state and desorption velocity of the excited species and, obviously, the projection of the sensor's field of view relative to the volume in which the emissions take place. In practice, the principal projections have been near-perpendicular and near-parallel to the surfaces catalyzing the excitation, that is, pointing into the ram hemisphere and about "sidewise" to these areas. The photographs and visible spectra of so-called shuttle glow from electronically excited NO_2 (Ref's 4, 17, 18) were obtained in the latter viewing geometry, and the photometric observations extending into the near UV (Ref's 19-21) in the former.

Section 5 develops a formalism for calculating the relative radiances of glow features, for arbitrary sensor projections to simple surface configurations. Its development also applies to estimating the irradiance that would be measured when the glow volume underfills the optical sensor's field of view, such as when instruments sensitive over wide angles are located long distances away (at ground stations, for example). The results in Section 5 are intended for use in positioning and setting sensitivity thresholds/exposure times of spectroradiometers, to maximize the signal from spacecraft glows relative to the noise from the terrestrial and celestial backgrounds and the instrument itself.

Rocket Exhaust Interactions

Section 6 of this report is a review of the separate topic of excitation of ultraviolet and visible emissions that results when the combustion products of high-performance

rocket engines, which themselves are moving at orbital speeds (~7½ km/sec), strike the thermosphere's principal neutral components O and N_2. In practice, the laboratory database on molecular collisions in this ~1-10 eV energy range does not lend itself to reliable prediction of the partial cross sections for atom interchange and other reactions that leave one or more products in an electronically excited state. Nonetheless the abundances and relative (center-of-mass) velocities of the exhaust species, the spectroscopic selection rules for conservation of spin angular momentum in reactions, and the radiative lifetimes in the accessible excited states do serve to identify those molecular band systems in which the highest brightnesses of the exhaust-interaction volume can be expected.

Furthermore the data from reaction chambers and shock tubes operated at high temperatures, and from colliding molecular-beam experiments performed with species other than those present in rocket exhaust, provide a modest basis for rough estimates of the cross sections for exciting some low-lying electronic radiative states of O_2 and OH when major combustion products collide with the atmosphere's oxygen atoms. The estimates involve physically plausible but largely untested assumptions about application and extrapolation of these laboratory data--and of results of the guiding ab initio molecular potential theory, with which they are in qualitative agreement--to excitative interactions. (Uncertainty in the actual vibrational distributions of the exhaust molecules, and of the part played by vibrational excitation in lowering reaction barriers, is a further source of error here.) These cross sections appear to be about two orders of magnitude smaller that those for elastic collisions, most of which lower the kinetic energies of the exhaust species below the few-eV endothermicities of the principal chemiluminescence-producing reactions. The estimates in Section 6 are intended for use in models of the optical radiation patterns of rocket exhaust plumes.

Final Section 7 describes a calibration of the short

wavelength-infrared radiances of such an exhaust plume from a space shuttle rocket engine against the sunlight scattered from the vehicle's tile outer protective surfaces, in connection with an analysis by AFGL of the plume's surface brightness distribution and total sterance. The images reduced had been taken with a long-focal length camera tracked on Orbiter as it passed near Hawaii. The work involved calculating spectral shapes of the vibrational-bands emission from the plume gas at its expected radiating temperatures, applying the appropriate transmission of the atmosphere in the path to the groundbased optical sensor, and relating the solid angles subtened by and apparent brightnesses of the luminous volume to those of the reflecting spacecraft body. The results lead to an interpretation of the actual infrared-radiance pattern in terms of a model of the interaction of the thruster rocket engine combustion products with the atmosphere, which has been submitted for journal publication by the Air Force Geophysics Laboratory.

SECTION 2

ULTRAVIOLET GLOWS FROM RECOMBINATION ON SPACECRAFT SURFACES

Introduction

We review in this Section the emissions at wavelengths shorter than the 3990 Å ultraviolet cutoff of chemiluminescence from the reaction of NO with O to produce NO_2^* ("shuttle glow"), that would be expected to result from recombination of atmospheric species on the exposed surfaces of spacecraft in low earth orbits. Such radiations have been seen in the near UV by multichannel photometers on Atmosphere Explorer satellites as described in Section 3 (see Ref's 19, 20); in the vacuum UV by a spectrograph as described in Section 4 (see Ref's 22, 23); and perhaps also by a spectrometer (Ref 24), as noted in this Section. These observations were made in connection with other (airglow-aurora) experiments, and a coherent program to characterize the UV glows using the Arizona Imager/Spectrograph is only now being planned. We will show that the principal expected off-surface radiations are the Herzberg I (A→X) bands of O_2; the β (B→X) bands of NO; and the Lyman-Birge-Hopfield (a→X) bands of N_2, whose phenomenology is discussed in detail in Section 4. Potential curves of these three recombinant molecules, which identify some of the excitation paths to the upper states of these and other transitions, are reproduced in Figure 2.1.

Technical Background

A review and interpretation of the data on spacecraft glows at the readily-detected visible wavelengths appears in Ref's 1 and 2, and further information about glow excitation is presented in connection with our predictions in Section 3 of the spatial extents and intensities at infrared wavelengths. To provide further context and additional background for assessing the

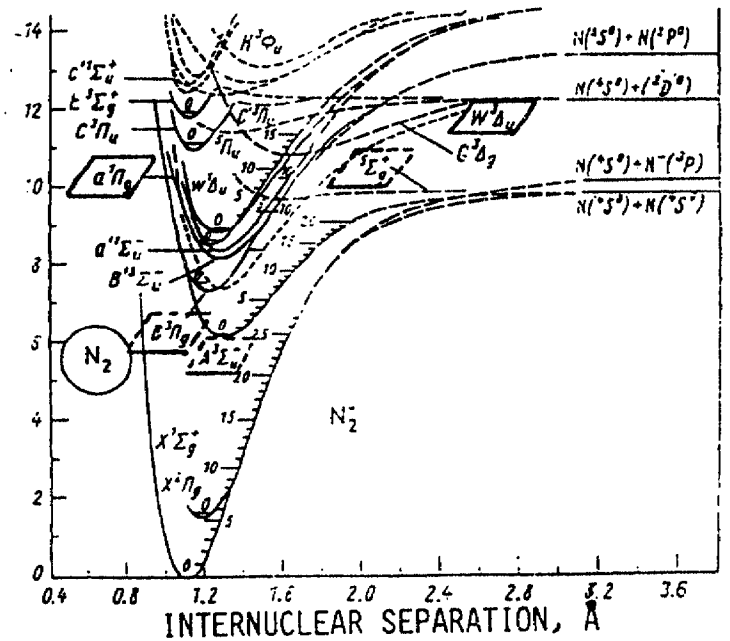

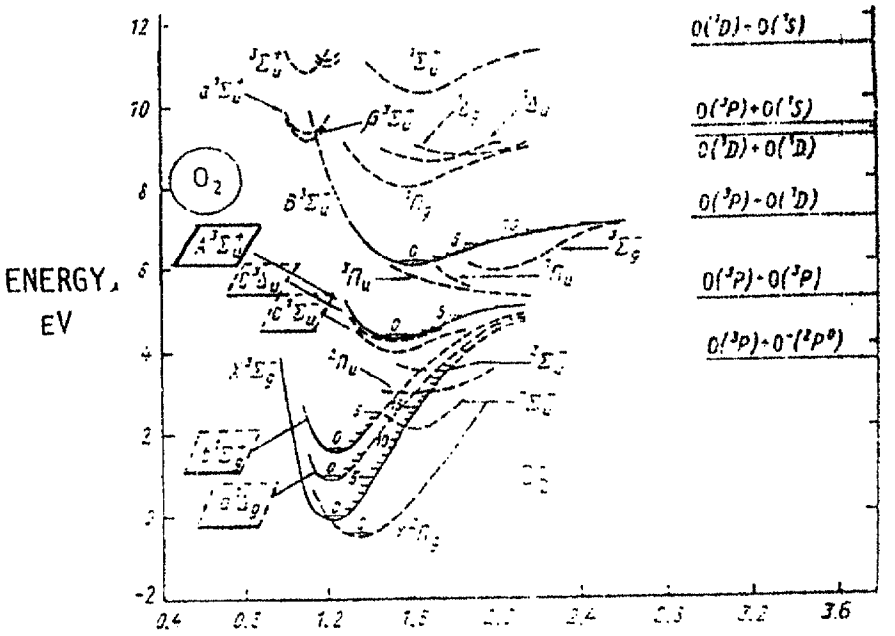

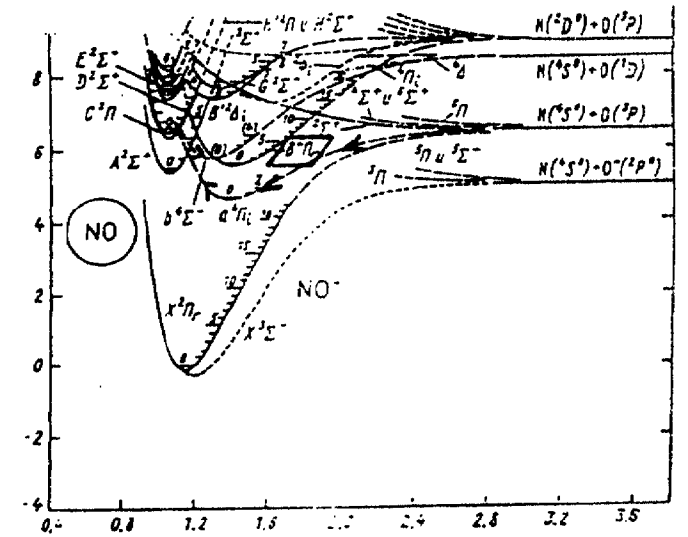

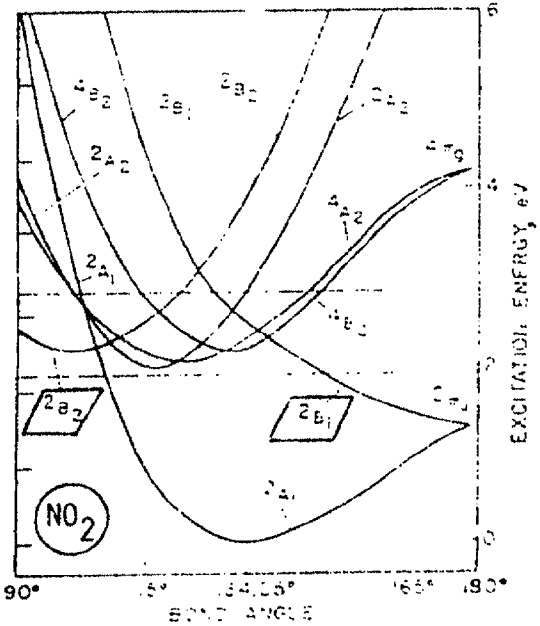

Figure 2.1. Potential curves of the four principal atmospheric recombination species.

ultraviolet--as well as IR--radiations, we repeat here the most relevant ideas about surface-catalyzed desorptive recombination.

Chemiluminescence can at least in principle be expected from species formed on spacecraft outer surfaces exposed to the incident atmospheric O^3P ($\sim 10^{15}$ particles/cm^2-sec to ram hemisphere-directed areas at 250 km orbital altitude) and O^1D ($\sim 10^{11}$ by day, 10^9 at night), O^+ ($\sim 10^{11}$), O_2 ($\sim 10^{14}$) and O_2 $a^1\Delta_g$ ($\sim 10^{10}$), N_2 ($\sim 10^{15}$) and N_2 v=1 ($\sim 10^{13}$), N^4S ($\sim 10^{13}$), NO ($\sim 10^{12}$), H($\sim 10^{12}$), H^+ and He^+ ($\sim 10^{10}$ and 10^9 above 500 km), other atoms and ions present at lower concentrations, and to some extent even ionospheric electrons. As the airflow at all but the very lowest orbital altitudes is essentially free-molecular, the fluxes to outer surfaces oriented parallel to the spacecraft's direction of motion are only about ¼ x [mean thermal velocity]/[spacecraft velocity] ($\approx 1/50$) times these nominal figures, and those to backward-facing (wake) areas are considerably lower still; hence radiation off other than ram areas has been below the detection thresholds of those optical instruments that have viewed the off-surface volumes. The potential curves of N_2, O_2, and NO in Figure 2.1 indicate the electronic states accessible from recombination of the high-concentration O^3P and N^4S atoms, many of which are the upper levels of ultraviolet (>3 eV) transitions.

Satellite orbital decay ("drag") and mass spectrometer data have shown (Ref's 25-27) that at altitudes below at least 300 km a high fraction of these incident ~7½ km/sec relative velocity air atoms and molecules collide inelastically with most materials used as vehicle outer surfaces. Some small fraction of these accommodated particles react together (or with preexisting contaminants) before desorbing, in what are called Langmuir-Hinshelwood recombination processes: both species adsorbed on, and diffusing over, the substrate. Adsorbed atoms and molecules may also combine directly with later-arriving incident gas, in so-called Rideal-Eley processes.

As the rate coefficients of most of the gas-phase exothermic recombination reactions of these thermospheric species decrease with increasing relative velocity, L-H processes are judged to be a much more probable cause of the chemiluminescence. The surface is not needed to lower potential barriers or break chemical bonds, but rather serves as a medium that allows atoms and molecules to approach one another and align sterically. These ideas are supported by the emission spectrum distribution (see Section 3) and dependence on angle to the airstream of the visible pseudocontinuum glow off Shuttle Orbiter (Ref's 1, 7): the high translational energy of the air particles does not appear to play a direct part in the reaction that produces this radiation. At least some of this kinetic energy may, however, be required for creating and maintaining of defect sites that promote reactions among adsorbates that result in escape of internally-excited products; that is, the high-velocity air may be "conditioning" the substrate. (A counter view, based on uncalibrated photographic images of visible glow from Orbiter's vertical stabilizer region, is presented in Ref 28. In any case, the question of how much particle kinetic energy is needed to produce a reactive site for NO + O recombination--if any--has not been seriously addressed, much less answered.)

Exothermic oxidizing reactions of the arriving air species with exposed materials (such as plastics) are thought to have potential barriers of the order of 1 eV. These would therefore proceed much faster on-orbit in ram, where the available center-of-mass kinetic energy is a few eV, than when the "cold" gaseous reactant is flowed to these surfaces in the laboratory. To date, however, no relation between the rate of ablation (and associated texturing) of actual spacecraft-surface materials and the intensity of optical radiations from the volume near them has been identified--: that is, surface damage so far appears to be independent of surface-catalyzed emission of visible light.

We look, then, to the database from experiments done with reactants having lower velocities in chemical-kinetics and

surface-science laboratories for guidance in determining the excited states into which neutral aeronomic species associate. The results of a survey of the literature (Ref 1) on surface-catalyzed excitation of N_2, O_2, NO, and NO_2 desorbate molecules formed from the principal incident reactive species ground-state O, N, and NO are reproduced in Table 2.1. Chemiluminescent reactions in the gas involving precursors produced at the surface, a common artefact in the laboratory but a potential source of only very low-brightness glows at the much longer collision mean free paths of low earth orbit, have been expressly omitted (where they are clearly identifiable from the laboratory results).

The upper states listed in this fourth column of Table 2.1 are almost certainly not the only ones populated in these recombination reactions, but are merely those detected by the experiments' necessarily-limited diagnostic equipment. Further states of most of these molecules are observed when they are formed by homogeneous--gas-phase--recombination, as is suggested by Figure 2.1. Insofar as chemical theory would predict that all energetically-accessible, angular momenta-conserving electronic states are initially populated, those that are not detected following heterogeneous--surface-catalyzed--recombination may be presumed to be deactivated by the substrate (or, perhaps, by other species chemisorbed or physisorbed on it). Interaction of the excited fragment with the surface before it desorbs into the gas phase tends to make the distribution in vibrational states differ from the initial distribution from homogeneous recombination, as is discussed in the context of excitation of $N_2(a)$ in Section 4. (Furthermore, this distribution usually differs from that from impact excitation, as would be expected from the potential curves of the upper states of the electronic transitions relative to the ground state.)

The survey of laboratory results (Ref 1 and Table 2.1) identified no surface-promoted association into excited O_3, N_2O, OH, or any of the many other energetically-accessible

Table 2.1. Surface recombination of O, N, NO resulting in desorption in excited states

Species	Surface	Conditions	Excitation state	Comments*
N_2	Poly Fe	N permeates, 1150K	X, high v	T_v depends on sulfur coverage
	Poly Co, Ni	N in flow tube	W, v≈11 (inferred)	Nitrides necessary for excitation
	Co, Ni, Ag	N and O flow	A? (B detected)	May be W state; see text
	Co	N flow, 333-413K	A (inferred)	$\sim[N]^2$, negative dependence on T_s
O_2	Ni	O flow, 303-343K	A (Herzberg I)	$\sim[O]^2$, little dependence on T_s
	Ni, Co, Glass	O flow	A, 0.1/recomb	Glass requires conditioning
	Poly Ni	O flow	A (v=0 & 1), b	No OI lines
	Poly Ni	O flow	A, A' (a, b?)	No c, or O^1S, is excited
NO	Ni	N, O flow, 300K	B (beta bands)	Non-statistical T_v, no excitation detectable on teflon surface
	Ni, Co, Ag	N, O flow, 300K	B	$N_2(B)$ also detected
NO_2	Ni	NO, O flow, 303-353K 22 millitorr	$^2B_1$, $^2B_2$	First order in each reactant, small positive T_s dependence, emission lies to red of gas-phase spectrum

*T_s = surface temperature ≈293K unless stated otherwise, T_v = vibrational temperature.

recombination products of the aforementioned thermospheric species. It also failed to turn up reports of desorption of O^1S or ^1D, or N^2P or ^2D, which low-lying states could in principle be products of fragmentation of reaction complexes or of the recombination of positive ions with electrons that we make note of later. (Passive optical detection of these long-lived metastable atoms would pose substantial experimental difficulties, for the reason discussed in Section 5.) Other recombinant molecules found to desorb from laboratory surfaces with unequilibrated internal excitation (or translational energy) are H_2 and D_2; CO; and CO_2 and SO_2, which emit pseudocontinua similar to that from NO_2^*. Additionally, the carbon atoms in some materials exposed on spacecraft may ablate compounded with incident O and O_2 to produce CO^* (and perhaps also CO_2^*). The ultraviolet-emission consequences of this last--and so far unobserved--process are discussed in Ref 29; as noted above, the reactions might require some of the few-eV translational energy of the incident oxygen.

In fact in most of the surface-catalyzed exothermic recombination reactions that have been studied, energy equilibration between the desorbate and substrate was found to be incomplete. This laboratory result is at least qualitatively supported by theoretical arguments (Ref's 30, 31). Further, contaminants, even at sub-monolayer coverage, are known to increase many reaction rates, as does the physical conditioning (principally, production of surface defects) alluded to above. Conversely, interferences among incident species, presumably due to their selective occupation or saturation of reaction-promoting sites, reduce the magnitude and alter the order of recombination rates: contaminants are well known to "poison" catalysts. (For example, as noted in Section 4, O_2 molecules incident with $\lesssim$ 1/10 eV kinetic energy decrease the probability of recombination of N atoms on glass while increasing it on teflon (Ref 32); they poison--in the sense of industrial catalysis--active sites on the former, and chemically create them on the latter, non-polar,

material.) Experience shows that the total probabilities of desorptive recombination with internal excitation (i.e., failure of the surface to quench the excited state) are typically low, rarely exceeding 10^{-2} per incident participant at intermediate surface coverages. Therefore the column brightnesses in perpendicular projections, even when the emission extends outward a distance less than the characteristic surface dimension (see Section 5), will typically be more than two orders of magnitude lower than the fluxes of arriving reactive species.

In these "exothermic small molecule reactions and atom recombination reactions" (Ref 33), excess chemical energy is distributed among internal and translational states of the products and the modes of the substrates. This process is much too complex to allow the resulting population distribution to be reliably predicted ab initio. Thus, for example, the emission spectrum--even from a single desorbate species--as well as the total radiant intensity could depend on the properties of the surface material and its contaminants. The concentration of available adsorption and reaction sites determines the excitative recombination rates of species accommodated upon impact, that is, it controls the absolute spectral distribution of the off-surface radiation(s). This idea is illustrated by the weakness of visible glow off polyethylene and anodized aluminum patches attached to orbiting spacecraft compared with that off paints having unsaturated chemical bonds (Ref's 4, 18), as well as the known low rates of recombination on laboratory teflon (Ref's 32, 34)--a material commonly applied as a passivating surface in laboratory experimentation and process chemistry.

Even for species on (or approaching) atomically clean and otherwise well characterized regular model laboratory surfaces--"perfect crystals"--, far too little information about the chemical interaction potential is available to predict the desorption rates of excited recombinant molecules. Furthermore, the mix of atmospheric species incident on spacecraft over their range of low earth-orbital altitudes is a potential source of

both negative and positive interferences that would alter the order of reactions on these engineering (and usually dirty) outer surfaces. (The incident flux of ground-state O atoms is about one monolayer in one second even at 250 km altitude, which is considerably larger than achievable in most laboratory apparatus.) In consequence we have not attempted to estimate the absolute column intensities of the ultraviolet band systems that laboratory experience suggests would be excited at spacecraft surfaces.

Radiance and Measurement Considerations

As is discussed in in detail Section 5, the glows detectable by passive optical methods are those that arise from upper states whose radiative lifetime τ is sufficiently short to result in radiances that exceed the noise from the instrument and atmospheric/astronomical background. Since the mean normal effusion velocity of low molecular-weight desorbates from 300K surfaces is near 500 m/sec under the commonly-encountered conditions 1) the desorption process is indeed effusion at this substrate temperature rather than a mechanism resulting in higher velocity (such as that identified in Ref 16), and 2) the offcoming species is not confined and/or deactivated by collisions with the local gas, the mean radiative pathlength--the glow "thickness"--is ~500τ m. As an example, NO molecules effusively desorbed in the $B^2\Pi$ electronic state, which have 3.2 μsec radiative lifetime, would emit β-bands (B→X) principally over a ~1½ mm outward distance if their probability of colliding with off-surface gas is negligible. If on the other hand these molecules are confined by collisions--as appeared to be the case in one laboratory experiment (Ref 35)--the glow volume would be even smaller. In any case, the ~1½-mm radiative pathlength is small compared with the typical dimensions of laboratory reaction chambers, and thus a reasonable fraction of the excited molecules could be counted.

Permitted optical transitions with shorter lifetimes produce still "thinner" glows, which in practice are passively detectable

only when the excitation-producing surface itself lies within the field of view of the sensor. (Refer again to Section 5.) When this field is directed into ram, the short-lived excitation detected is taking place within the sensor's own optical system. The 3700-sec lifetime of O_2 in the (near infrared-radiating) $a^1\Delta_g$ state represents the other measurement extreme: so small a fraction of any such desorbate molecules emit spontaneously under laboratory conditions that indirect-chemical or tuned laser-pumping methods are needed to detect them. In orbit (or during re-entry), virtually all of the $O_2(^1\Delta)$ molecules directed into the nadir hemisphere would experience momentum-transfer and/or depopulating collisions with the atmosphere before radiating, and furthermore the a→X glow volume would be so widely spread spatially that it would almost certainly have subthreshold surface brightnesses. (This point is brought up again in Section 3.)

In view projections from or to spacecraft, background optical noise is present from both celestial sources (stars, zodiacal light) and terrestrial sources (airglow and aurora, natural and man-made light scattered by the atmosphere). As these radiations also are reflected off surfaces of space objects, these surfaces must be held outside the instrument's instantaneous field of view to minimize the background count rates. The signal from induced glows obviously depends on the sensor's view projection and r, in a way quantified in Section 5. Considering that the probabilities of excitative recombination per incident air particle are not known, some of the radiations discussed in the next subsection may provide inadequate optical signal above this noise no matter what sensor projection (or inherent instrument "sensitivity", and/or integration time) is applied.

Excitation States and Ultraviolet Emissions

Table 2.2 is a listing of the energetically-allowed upper electronic states that result from recombination of the ground-state neutral atoms and molecules abundant at orbital altitudes.

Table 2.2. UV recombination radiations at low earth orbital altitudes

Recombinant Species	Upper Electronic States Accessible,* lifetime	Ultraviolet Band Systems Radiated	Radiative Pathlength**
$O^3P + O^3P \rightarrow O_2^*$	$A^3\Sigma_u^+$, 0.18 sec $\underline{A}'$ (or C) $^3\Delta_u$, ~20 sec $\underline{c}$, a, b	Herzberg I ($\rightarrow X$) Herzberg II (Visible and IR)	80 m 10 km 5 - 100's km
$N^4S + N^4S \rightarrow N_2^*$	$a^1\pi_g$ 120 μsec $A^3\Sigma_u^+$ with v^*20, ~1000 μsec $A^3\Sigma_u^+$ with v^*5, 2 sec $B^3\pi_g$ a',B',W ~0.04, 10^{-5}, and 10^{-3}-10^{-2} sec (mostly IR)	L-B-H ($\rightarrow X$) ($\rightarrow B$, IR; $B \rightarrow A(v^* 5)$, Visible and IR) Vegard-Kaplan Visible but produces A, low v	6 cm 1 km
$N^4S + O^3P \rightarrow NO^*$	$\underline{B}^2\pi$, 3.2 μsec $\underline{A}$, 0.2 μsec C, 0.025 μsec a, b, 0.16 and 6 sec	β ($\rightarrow X$) γ ($\rightarrow X$) δ ($\rightarrow X$) (Visible and IR)	1-1/2 mm 1/10 mm
$NO + O \rightarrow NO_2^*$	$^2\underline{B}_1$, $^2\underline{B}_2$, 25-250 μsec	Pseudocontinuum, no UV component	1-10 cm
[CO	Refer to Ref 29]		

*Those underlined have been detected in the laboratory; refer to Table 2.1.

**Assuming the desorbate molecules have equilibrated-effusive desorption velocities.

(The lower fluxes of the other naturally-occurring--including metastable--species would be expected to produce weaker glows; radiations from recombination of ions with electrons are briefly discussed later.) The entries are derived from the standard potential energy diagrams for N_2, O_2, and NO in Figure 2.1, which show the vibrational levels of the molecules relative to the association energy of the two recombining atoms and some of the curve-crossings thought to lead to transfer between electronic states. Those excited molecules that have been seen to desorb from some laboratory surface materials are underlined (refer to Table 2.1).

We have chosen to include in Table 2.2 all the accessible excited states, many of which appear in homogeneous recombination (albeit in some cases through kinetically complex reaction processes rather than simple direct association). The laboratory database is far to sparse to preclude population of these "undiscovered" states on all exposed spacecraft materials at all outer-surface temperatures encountered in orbit, and furthermore (as noted above) no compelling theoretical arguments exist for their absence. This listing should be viewed in the context that no dramatic surprises in the electronic or vibrational states that are populated by surface catalysis have so far been observed; that is, no excited molecules appearing only under special gas-phase conditions (electrical discharges with foreign species, for example) have been found to desorb from laboratory surfaces. Whether further upper states with long lifetime and/or small probability of branching to ultraviolet transitions are excited is a moot question, because of the expected undetectably-low brightnesses of the resulting UV glows. To date most heterogeneous recombination to excited N_2 (Ref 36), O_2 (Ref's 37, 38), and NO (Ref 34) has resulted in emission from generally lower vibrational levels than from the analogous homogeneous reactions, which (as mentioned earlier) implies some degree of vibrational accommodation before the electronically-excited molecules desorb.

In the interest of completeness we have also included in Table 2.2 upper states from which no ultraviolet (>3 eV) photons are emitted due to their insufficient potential energy or, more commonly, which produce very weak UV emission in gas-phase experiments due to spectroscopic selection rules. Radiation in the latter band systems would in general be correspondingly weak upon surface-catalyzed recombination and thus is not included in the discussion here.

O_2 molecules have three closely-lying excited states ($A^3\Sigma_u^+$, A' [formerly C] $^3\Delta_u$, and $c^1\Sigma_u^-$), the lowest vibrational levels of which are within ½ eV of the 5.1 eV energy of recombination of two O^3P (ground electronic state) atoms (see Figure 2.1). Transitions to the ground ($^3\Sigma_g^-$) or the two other low-lying electronic states of O_2 ($a^1\Delta_g$ and $b^1\Sigma_g^+$), however, all are strongly forbidden (i.e., the radiative lifetimes and thus pathlengths are long); the only transitions that provide significant UV column intensities are the A→X (Herzberg I) bands. The largely blue but partially near-ultraviolet electronic bands originating from very low vibrational levels of the A state have been found to be catalytically excited by both metallic and insulating surfaces (first entry in Table 2.2); these would be emitted over a ~80 m path [assuming as usual effusive desorption]. Any A'→X (Herzberg II band) radiation, which is qualitatively spectrally similar because of the closeness of the potential curves of the A and A' states, would arise from a two order of magnitude longer radiative path; thus even if these two levels were populated with equal probability the Herzberg II system would present two orders of magnitude less glow brightness in all view projections than the Herzberg I system (as is shown in Section 5).

The radiance in the Herzberg I system in projections directly into the windward hemisphere from ~30 m x 7 m-projected area Shuttle Orbiter can be shown from the geometry arguments in Section 5 to be 10^{-8} rayleighs per excitative recombination per sec from each square centimeter of spacecraft surface exposed.

Since the flux of oxygen atoms incident at 250 km orbital altitude is $10^{15}/cm^2$-sec, the resulting system brightness in this view would be about 5 x 10^7 x [probability that incident O + O → $O_2(A)$] rayleighs. The assumtion that this excitative desorption probability averaged over the surface is 10^{-4} would lead to a column intensity of 5 kilorayleighs. Even though this UV scene radiance is spread over many individual bands of the Herzberg I system (with an unknown distribution), it would appear to be measurable against the ~1 rayleigh/Å blue and near-UV astronomical background.

N_2 molecules in excited states are known to result from surface-catalyzed recombination of N^4S atoms. As is discussed in further detail in Section 3, the process that excites the off-surface yellow-red First Positive (B→A) bands in Table 2.2 has not been definitely identified. Nonetheless the ultimate electronic state of whatever radiational "cascade" is taking place within the N_2 triplet system is $A^3\Sigma_u^+$, which from its lower vibrational levels leads to the Vegard-Kaplan (A→X) intercombination system between about 2300 and 3000 Å. (The highest vibrational levels of the A state are thought to produce some infrared photons; see Section 3.) However as the lifetime against this spin-forbidden UV transition is as long as 2 sec, the radiances of any spacecraft glow in the Vegard-Kaplan bands would be correspondingly low. In the natural atmosphere, these bands (from $N_2(A)$ at ~350K, excited by electron impact in the aurora and dayglow) are collisionally quenched by O atoms at altitudes below approximately 130 km.

The ~6 cm radiative pathlength of N_2 in its $a^1\Pi_g$ state [again assuming effusive desorption] is favorable for drift of the excited molecules into the fields of outward-viewing sensors. Evidence for the important spacecraft-induced N_2 a→X (Lyman-Birge-Hopfield bands) glow, with spectral distributions and some information on absolute intensities, is reviewed in detail in Section 4.

NO molecules in their $A^2\Sigma^+$, $B^2\Pi_r$, and $C^2\Pi$ (lowest v only) states are produced by homogeneous recombination of N^4S and O^3P atoms. The much longer-lived quartets $a^4\Pi_i$ and $b^4\Sigma^-$ are also energetically accessible, but if they are populated in laboratory gas-reaction chambers have so far been collisionally quenched or curve-cross to the A, B, and C states before the NO molecule can radiate. The presence of these three NO doublets in gaseous recombination is evidenced by emission of the ultraviolet γ, β, and δ bands respectively in transitions to the molecule's ground electronic state; these bands are seen from planetary atmospheres (including the earth's thermosphere), as well as in laboratory reaction chambers.

In contrast, when the recombination is catalyzed by surfaces only the β bands, which lie between ~2400 and 3800 Å, have so far been spectroscopically detectable (Ref's 34, 36). Their vibrational distribution differs from that from the gas-phase reaction, which has led to the interpretation (Ref 34) that the NO B state is populated "directly" at/by some substrates without participation of the bridging electronic states illustrated in Figure 2.1. When NO bound in solid frozen argon matrixes is bombarded by energetic electrons, x-rays, or UV photons, the resulting fluorescence spectrum shows that the B and $a^4\Pi$ states are excited (Ref 39); and in solid nitrogen only the B state appears. This finding further indicates that material surfaces ineffectively quench the $B^2\Pi$ electronic configuration (which has a smaller electric dipole moment than the A and C states, and thus is less strongly coupled to the substrate).

Nonetheless the two laboratory experiments so far performed on excitative N + O recombination--both on similar polycrystalline metals (the glow was undetectable off teflon (Ref 34))--represent an insufficient database to rule out some catalyzed excitation of these latter states of NO on all spacecraft surface materials. The outward extent of these two glows, however, would be one and two orders of magnitude less than the ~1½ mm of the β-bands glow. (The radiative lifetimes

of the upper states are listed in Table 2.2.) Thus UV sensors with fields of view directed outward would measure only that γ- and δ-band radiation excited on areas within or extremely close to these optical fields that are exposed to inflowing atmospheric N and O atoms (such as the first objective lens or mirror surface).

The interference filter photometer of the Visible Airglow Experiment, which pointed into ram on Atmosphere Explorers, measured about equal radiances from vehicle-induced glow at 3370 ± 10 Å and 2800 ± 10 Å (Ref 20). As mentioned in Section 3, when the wavelength sensitivity profiles of the two photometer channels are taken into account this ratio is at least semiquantitatively consistent with the relative intensities of the (0,9) and (1,6) NO β bands measured (Ref 34) off a laboratory metal surface. Thus recombination into the NO B state--presumably, on the edges of the forward-mounted baffles or the objective lens of this photometer, whose optical system is diagrammed in Ref 40--is a plausible explanation for the vehicle-associated UV radiation observed from these low earth-orbiting satellites.

However, in view of the fact that the Visible Airglow Experiment photometer sampled only two UV wavelength intervals this spectral identification can of course be only tentative. For example the bandheads of the (3,5) and (5,2) O_2 Herzberg I transitions are at 3370 and 2820 Å; and while in laboratory gas-discharge afterglows the intensity ratio of these bands is closer to 3 (Ref 41) than to the 1 that was measured off Atmosphere Explorer, the conditions for excitation of $O_2(A,v)$ on surfaces are not the same as those in discharges. On the other hand, the observation that NO molecules (in unknown electronic and vibrational states) are copiously produced by recombination of N with O atoms on glass as well as metal walls of spacecraft pressure gauges (Ref's 42, 43) supports the idea that the UV signals from Atmosphere Explorers are due to NO β-bands. Furthermore, the column intensity of this UV glow--within the narrow photometer

bandpasses, only a few x 10^6 photons/cm^2-column-sec at ~200 km orbital altitude--is several orders of magnitude less than the flux of nitrogen atoms incident on Atmosphere Explorer's surface, so that a low excitative recombination probability would suffice to explain the intensities as due to NO(B→X). The aforementioned spectrographic measurements planned from Shuttle Orbiter are expected to resolve the question of the origin of this middle- and near-ultraviolet spacecraft glow.

Ion Recombination Radiations

A further potential source of UV excitation of is neutralization of atomic ions from the ionosphere on exposed vehicle surfaces. This process could in principle produce both free-bound and bound-bound (cascade) multiplet emission from O, H, N, and He atoms, extending over a broad wavelength range. The sole evidence for such recombination radiative is the observation of excess nighttime vacuum ultraviolet signals from the STP78-1 spacecraft (Ref 24) orbiting at low latitudes near 600 km, at which altitude the concentration of H^+ becomes about equal to that of O^+. These measurements indicate the presence of ~1.5 kR of vehicle-associated hydrogen Lyman-α (near 1216 Å) radiation in the ram direction, along with a small excess over natural nightglow in the OI ^5S-^3P (1356 Å) intercombination lines and near the 911 Å long-wavelength limit of the recombination continua of H or O. (These lie very close to one another, as both H and O coincidentally have almost the same ionization potential.) However, no statistically-significant enhancement in the strong--and multiply-scattered--OI 1304 Å ^3S-^3P resonance triplet was observed. The >10 eV energy required to excite the H Lyman-α line could be provided by neutralization of atmospheric H^+, whose flux to ram surfaces at the satellite altitude is about 10 times the excess column emission rate that was measured in Ref 24.

This surface-catalyzed recombination of atomic ions has not to our knowledge been reported from the laboratory (for example,

from off the walls of plasma generators). If it takes place in the space environment, the process would lead also to smaller amounts of radiation of hydrogen Lyman-β at 1026 Å, -γ at 972 Å, and in other lines of the Lyman series; the above-mentioned UV lines of O (as well as others at longer wavelengths); and also He lines (principally at 537, 584, 3188, 3889 Å). (Radiation from neutralization of the less-abundant N^+ ions would be expected to be weaker.) As the lifetimes of most of the upper electronic states populated are less than 200 nanosec, the initial radiative pathlengths would be so small that only excitation on surfaces within the sensor fields themselves would be detectable. Note that ion recombination would become relatively more important with increasing spacecraft altitude (all other physical factors being equal), since the neutral density of the atmosphere decreases upward much more rapidly than its ion density (which varies by a factor of only 2 to 3 between 200 and 600 km).

Summary

The principal glows at ultraviolet wavelengths expected from recombination of ambient upper-atmosphere neutral species at spacecraft surfaces are the Herzberg I bands of O_2 (potentially intense due to the high fluxes of O atoms, and moderately spatially widespread due to the ~2/10-sec radiative lifetime of the molecules in the desorbing "beam"); the β bands of NO (which in strong contrast are emitted over a $\leq$2 mm path if the NO molecules leave the surface translationally accommodated); and the Lyman-Birge-Hopfield and to a much lesser extent Vegard-Kaplan bands of N_2 (whose radiative pathlengths are near 10^1 and 10^5 cm respectively). The apparently-dominant off-surface feature at visible-wavelengths $NO_2(^2B_{1,2} \rightarrow X)$ has a very weak extremely near-UV tail; and the γ and δ bands of NO, while accessible from recombination of ground-state N and O atoms (see Figure 2.1) and commonly observed from homogeneous reactions, have not so far been experimentally detectable off laboratory surfaces. Very strong experimental evidence exists for

excitation of the vacuum-ultraviolet N_2 Lyman-Birge-Hopfield bands (Section 4); moderately strong evidence exists for the middle-ultraviolet NO β bands; inferential (negative) evidence exists for the expected low radiances in the middle-ultraviolet Vegard-Kaplan band system; and the prediction of near-ultraviolet (and blue) Herzberg I radiations off low earth orbiting spacecraft is based solely on laboratory experience. In addition, unverified data from one satellite survey suggest that neutralization of the ionosphere at (or perhaps near) spacecraft can result in the population of upper states of ultraviolet atomic lines.

The observed variation of visible-glow excitation with exposed material (Ref 4) suggests the possibility of discriminating among low earth-orbiting or exo-reentering target vehicles on the basis of the rates of excitive recombination of ambient atmospheric species on their ram surfaces. A larger database on the relationship between specific catalytic reaction rates and surface material properties would be needed to predict altitude profiles of absolute column intensity; the mix of possibly-interfering incident atmospheric atoms and molecules is a potentially complicating factor.

SECTION 3

INFRARED GLOWS FROM RECOMBINATION ON SPACECRAFT SURFACES

Introduction

We review in this Section the emissions at wavelengths longer than the ~8000 Å (S-20 photoemissive response) cutoff of the spectroradiometers so far applied in measuring off-surface glow brightnesses, that would result from recombination of incident atmospheric species on areas of low earth orbiting spacecraft exposed to the airflow. Table 3.1 is a listing of the infrared-radiating molecular states expected from exothermic reactions between the most abundant chemically active atmospheric species O, N, and NO (none involve incident O_2 or N_2). Refer to Section 2 for nominal fluxes of these reaction participants, and to Figure 2.1 for potential curves of four of the molecules of Table 3.1.

Infrared photons from radiative cascade (first and second entries in Table 3.1) accompany both the pseudocontinuum chemiluminescence of NO_2 recombined in the gas phase into its $^2B_2$ and $^2B_1$ electronic states (Ref's 7, 44, 45) and the β bands of NO ($B^2\Pi \rightarrow X^2\Pi$) populated by the N + O recombination process discussed in Section 2 (Ref 7). Spectrally similar IR emission would result when the upper states are excited by formation/desorption of these molecules at spacecraft surfaces. The principal discrete NO_2 features expected are the ν_3 fundamental sequence centered at 6.2 μm and $\nu_1 + \nu_3$ intercombination bands near 3.6 μm. In addition the manifold of overlapping electronic transitions of the nitrogen dioxide molecule--its pseudocontinuum--is known to extend through the short-wavelength infrared (third entry). Nitric oxide molecules would emit their familiar fundamental and first overtone bands above 5.3 and 2.7 μm. The relatively long (~1/10 sec) radiative lifetimes of the upper vibrational states of these two odd-nitrogen species lead to infrared emission from volumes having dimensions comparable with or greater than those typical of spacecraft, with correspondingly reduced column intensities in most view

Table 3.1. Infrared (≥ 8000 A) surface recombination species

Excited Molecule	Source	Comments
$NO(\tilde{X}^2\Pi, v>0)$	Cascade from $NO(B^2\Pi)$	Present if β bands (Section 2) are excited, 2.7 and 5.3 μm
$NO_2(\tilde{X}^2A_1, \nu_1\nu_2\nu_3)$	Cascade from $^2B_{1,2} \rightarrow X,v$	Several band systems, strong; 3.6 and 6.2 μm, extending to 13 μm
$NO_2(^2B_1, ^2B_2)$	NO + O Recombination	Long-wavelength tail of pseudo-continuum extends to ~3 μm
$N_2(W^3\Delta_u)$	N + N Recombination	Inferred from laboratory results; Wu-Benesch (W→B) bands
$N_2(B^3\Pi_g)$	Cascade from W (or A) state	Seen in the laboratory; First Positive bands (B→A) extend into the near-IR
$O_2(a^1\Delta_g)$	O + O	IR Atmospheric bands (a→X), 1 hr radiative lifetime results in extremely low brightness
$O_2(b^1\Sigma_g^+)$	O + O	Near-IR Atmospheric bands (b→X) 12 sec radiative lifetime results in low brightness
$NO(b^4\Sigma^-)$	N + O	Near-IR Ogawa (b→a) bands, 6 sec radiative lifetime
$O_3(\nu_3)$	$O + O_2$	Not identified in laboratory; improbable, but if excited 001-000 at 9.6 μm, + hot bands

projections (refer to Section 5). We will estimate from their spectroscopic properties the numbers of photons per recombination reaction in each infrared band sequence (and in the long-wavelength tail of the NO_2 pseudocontinuum), and the resulting IR radiances relative to those of the observed (Ref's 4, 18) visible spacecraft glow from NO_2^* and the anticipated (Section 2) ultraviolet glow from NO^*.

The final four entries in Table 3.1 are included for completeness, as the long lifetimes of the excited desorbates--most of which, for this reason, have not been identified in the laboratory--lead to very low IR glow radiances; these species are discussed only briefly here. The visible (yellow red) transitions of the N_2 First Positive (B→A) system, which extends into the near infrared, are commonly seen in laboratory surface-catalyzed recombination of N atoms but have not been definitely identified off spacecraft (see Ref 1). Excitation of the $N_2(B)$ state may follow further infrared radiation in the W→B (Wu-Benesch) bands, as discussed below.

$NO_2^\dagger$: Formation Process

We proceed from the by now-familiar interpretation (Ref 1) that the species responsible for the orange-red (Ref 46), spectrally-continuous radiation that dominates the visible glow from the first ~10 cm to ramward from the silica-borosilicate glass protective tiles of Shuttle Orbiter is NO_2 ($^2B_1$, $^2B_2$), which is formed on these outer surfaces by reaction of ambient (or under some conditions exhaust-related) NO and O.

The maximum spectral intensity of this spacecraft glow lies some 1000 cm^{-1} (~1/8 eV) to the red of the peak of the chemiluminescence spectrum from third-body stabilized gas phase NO + O reactions. (Its less accurately-measured threshold appears to be shifted less if at all). This lower average photon energy is probably due to weak physisorption of the O atoms on, and reaction exothermicity taken up by, the substrate, as similar displacements of the emission spectrum are observed when O is bound in O_3

molecules. As pointed out in Ref 1, the differences in wavenumber of the spectrum peak are

-- ~4000 cm^{-1} when NO reacts with vibrationally excited O_3 (Ref 47);
-- ~7500 cm^{-1} in reactions with O_3 molecules that have absorbed a 1040 cm^{-1} photon and thus are probably in their 001 vibrational state (Ref 48); and
-- 8000 cm^{-1} in reactions with ground-state O_3 (Ref 49), in which the binding energy of the O atom is 8500 cm^{-1} or 1.05 eV.

The peak moves in the other direction--that is, the pseudo-continuous spectral distribution exhibits higher average photon energies--when no third body is involved; specifically, the difference is

-- 2500 cm^{-1} to the blue when the NO + O reaction is stabilized by radiation (Ref 50).

An alternative explanation of the longer wavelength of the spectrum maximum that results from the mix of the many overlapping electronic bands of NO_2 is, that the NO molecules are initially lying in shallow surface potential wells; a contribution from this mechanism would not materially affect the conclusions here.

In view of the only ~1/8 eV red shift of the spectrum peak (and the smaller or comparable shift of its threshold), the surface-catalyzed excitation reaction can be considered as chemically much more similar to NO + O + M attachment than NO + O_3 rearrangement reactions, which involve breaking the O-O_2 bond. We nonetheless present also the appropriate information from the literature about the electronic- and vibrational-band radiations that result from reaction of nitric oxide with ground-state ozone molecules, for reasons that will become apparent shortly. Table 3.2 summarizes the wavelengths of infrared emission and total photon yields and spatial extents that we derived from the laboratory and theoretical database on formation of NO_2 by oxidation of NO.

Table 3.2. NO_2 infrared radiations

Gas-phase reaction	*)	Wavelengths, μm ±HWHM	Vibrational Band	Photons per electronic transition	Radiative lifetimes, sec	Lifetime x 4×10^4 cm/sec, m
NO + O + M	0.45	3.61 +0.35, −0.25	$(\nu_1 + \nu_3)$ each $\Delta v=1$ sequences, with some $2\nu_3$	0.24 ±0.1	0.0078 near 3.5 μm (101→000, 0.077 sec)	3
NO + $O_3(\tilde{X})$	0.93	3.55 +0.24, −0.13		0.37 ±0.05	~0.002 near 3.7 μm ($\nu_1 + \nu_3 \approx 4$)	½
Both of above		6.2 ±0.35	ν_3 fundamental	3 (O) 4 (O_3)	0.0066 (001→000)	2, to ~½ at longer wavelengths
		13.3 ±1	ν_2	$\sim 10^{-3}$		
		7.6	ν_1	2×10^{-2}		
		2.5 ±0.13	unidentified	$\sim 10^{-3}$		

*) Fraction of electronic band photons at wavelengths >0.8 μm in the gas-phase reactions proceeding via the $^2B_1$ and $^2B_2$ states.

$NO_2^{\dagger}$: Infrared Emission

Virtually all the gas-phase NO + O recombinations (Ref 44) but only 7% of the NO + $O_3(X^1A_1)$ rearrangements (Ref's 49, 51) proceed through the $^2B_1$ and $^2B_2$ states of NO_2. The second column in Table 3.2 lists the fractions of photons in the resulting pseudo-continuums terminating in the ground ($^2A_1$) state of NO_2 that lie at wavelengths longer than 0.8 μm. (This is the nominal cutoff of the S-20 photocathode of the image intensifier used in the space shuttle spectrograph (Ref 17), and is near the long-wavelength limit of the existing photographic and photometric measurements on spacecraft glows.) We derived these fractional yields from the laboratory chemiluminescence spectrums, which tail off toward 2-3 μm with generally upward curvature (Ref's 52, 53) from flat peaks near 0.64 μm (Ref's 50, 54, 55) in the three-body recombination, and near 1.2 μm (Ref 49) in the rearrangement reaction with $O_3(X)$. As noted the peak from the distribution of NO_2 electronic bands excited in radiation-stabilized (two-body) recombination is close to 0.55 μm, which is ~1/3 eV above that from reactions stabilized by a kinetic energy-sharing third body.

In view of the modest shift to the red of the glow off Orbiter relative to that from the homogeneous NO + O + M reaction, we would expect that very closely half of the electronic-band photons from excitation by orbiting spacecraft would lie at wavelengths above 0.8 μm. Since this near-infrared radiation originates from essentially the same distribution of upper states as the visible radiation (Ref 49), its spatial distribution would follow the observed orange-red glow. That is, the column emission rates in the near-IR pseudocontinuum would be about equal to the more easily measured rates of emission of visible photons. The characteristic distances over which 0.4 - 0.8 μm radiation is emitted have been found to be about the same off recombination-promoting materials other than Orbiter's glass tiles (Ref 18). Nonetheless the initial population of vibrational states of NO_2^*, and thus the emission spectrum distributions, would not necessarily be the same off all spacecraft ram surfaces.

In laboratory third body-stabilized recombination of NO and O the NO_2 molecules are left with an average vibrational energy of about 6000 cm^{-1} after the electronic transition has taken place, with $\nu_1 + \nu_3 \approx 4$ (Ref 46). At low gas pressures (i.e., few energy-redistributing collisions) these excited molecules decay principally by radiating the ν_3 fundamental bands in a spectrum centered near 6.2 μm (Ref's 51, 52) and, with a factor 10 less probability, a superposition of $\nu_1 + \nu_3$ (each $\Delta v = 1$) intercombination bands (Ref's 45, 49, 53) near 3.6 μm. (Some ν_3 overtone radiation may also be present at the latter wavelengths.) In the laboratory, the intensities of these infrared bands (after the data are corrected for collisional deactivation and state transfer) are proportional to that of the pseudocontinuum, and the same dependence on temperature is also observed. These findings indicate that the discrete infrared bands all originate from upper vibrational levels of the lower (ground) electronic state of the visible-near IR transitions of the NO_2 molecule. Further, the observation that the ratio of intensities of the two principal infrared band systems does not change with concentration of the reactants shows that both systems arise from the same distribution of upper vibrational states.

The third and fourth columns of Table 3.2 give the approximate wavelength at which the spectral intensity is a maximum and the spectral width from the (unquenched) radiative-relaxation cascade, calculated applying an estimate of the ν_3 mode's anharmonicity. These spectrum distributions apply to optical projections normal to recombination surfaces with sides large compared with the characteristic radiation length ($S_o/L \gg 1$ in Figure 5.2), so that photons from all transitions have equal probability of reaching the (outward-pointed) remote sensor. The nominal errors in IR yield are estimated from the uncertainties in the total initial vibrational energy of NO_2 (X) and the branching ratios from states with vibrational quantum numbers > 1.

We estimated the number of photons emitted per recombination (fifth column) from the radiative lifetimes of NO_2 in the 101 and

001 states (sixth column), making the reasonable assumptions that 1) these transition probabilities increase linearly with vibrational quantum number (as in diatomic harmonic-oscillator molecules), 2) essentially all of the $\nu_1\nu_2\nu_3$ excitation is radiated in these two band systems, and 3) collisional deactivation of $NO_2^\dagger$ can be neglected. This last assumption is justified by the fact that the mean free paths for elastic collisions of $NO_2^\dagger$ at typical shuttle altitudes are at least comparable to the distances over which these molecules radiate [if they desorb from the surface at thermal-effusive velocities], and therefore their mean free paths against inelastic scatterings would be even longer. (We return to this point shortly.) The infrared yields are $\underline{3}$ ν_3 fundamental and $\underline{\frac{1}{4}}$ intercombination band photons per NO + O (+ surface) reaction. Since (as discussed above) only half of the accompanying electronic radiation is at visible wavelengths, the ratios of infrared vibrational-band to visible electronic-band photons are a factor two higher than shown in the fifth column of Table 3.2. The infrared estimates for NO + O_3 rearrangements refer only to that 7% of these reactions that proceed through the upper electronic states of NO_2 and therefore produce visible and near-IR pseudocontinuum photons.

The ν_1 (symmetric stretch) and ν_2 (bending mode) systems of NO_2 near 7.6 μm and 13.2 μm have been below detection threshold in laboratory emission experiments to date (Ref's 51, 52). This finding is understandable in view of their low Einstein coefficients relative to the $\nu_1 + \nu_3$ intercombination transitions. We have included estimates of the yields in these weak vibrational sequences in Table 3.2. One experiment group (Ref 51) has reported an unidentified small peak near 2.5 μm in the NO_2 emission spectrum, which appears also to be present (with ~10% of the amplitude of the underlying unresolved "continuum") in the spectrum measured earlier (Ref 53). This may be the unidentified feature reported in absorption by NO_2 in Herzberg's 1945 compilation (Ref 56).

$NO_2^\dagger$: Spatial Distribution

The off-surface spatial distribution of all the rovibrational radiations listed in Table 3.2 is controlled by the rapid ν_3 fundamental ($\Delta v = 1$) transitions. Since both the radiative lifetimes and vibrational spacings decrease with increasing quantum number, the longer-wavelength photons within each infrared sequence arise from narrower layers lying closer to the recombination surface; and conversely the shorter-wavelength photons of the vibrational cascade are on the average emitted later, that is, when the desorbed $NO_2^\dagger$ gas has moved farther away from the spacecraft. Thus the infrared spectral distributions that are measured will depend on the projection of the field(s) of the remote optical sensor. (As noted above, the spectral distributions characterized by the wavelengths of peak and halfwidth-to-half-maximum emission in Table 3.2 refer to views normal to a flat ram surface of dimensions at least comparable to the radiation pathlengths.)

The characteristic emission distances listed in the seventh column of Table 3.2 are approximate, as the laboratory identification of the upper vibrational states of NO_2 is imprecise and the information available about transition probabilities and branching from them is limited. (The band strengths measured by absorption spectroscopy refer only to transitions terminating in the ground state.) NO_2^* molecules are again assumed to desorb with the velocities that would result from thermal accommodation, close to a mean of 400 m/sec. The predicted radiation lengths are comparable with the collisional mean free paths of the desorbate molecules near 230 km (~20 m when corrected for the spacecraft velocity), so that at low orbital altitudes correction for quenching and conversion of $NO_2^\dagger$ to NO by the atmosphere's O atoms might in fact be required. The cross-section for the latter (exothermic) process is $\sim 3 \times 10^{-16}$ cm^2 at laboratory temperatures (Ref 45), which implies a quenching distance of the order of 100 m at 230 km if this cross-section has only a weak dependence on relative kinetic energy of the participants (as expected). Deactivation of $NO_2^\dagger$ by this reaction would be more probable than

collisional quenching by the atmosphere's less-abundant O_2 and N_2 molecules.

The characteristic emission distance of the visible glows so far measured from Orbiter is about 10 cm (Ref's 17, 18, 28). The arguments in Section 5 applied to the infrared yields and radiation lengths in Table 3.2 indicate that the corresponding maximum photon radiances viewing closely parallel to ram-directed spacecraft surfaces--that is, in the geometry shown in Figure 5.1--are two to three orders of magnitude lower than the visible radiances in the spectrum peak near 3.6 μm, and about an order of magnitude lower at 6.2 μm. In contrast, the similarly-estimated infrared photon radiances would be of the same order as the total radiances in the visible pseudocontinuum from NO_2 in perpendicular projections.

At 222 km altitude the brightness of the 0.4 - 0.8 μm glow viewing normal to the ram-directed tiles of Shuttle Orbiter was found to be 25 x 10^9 photons/4π ster-cm^2-sec (Ref 18). As Table 3.2 shows, 6 NO_2 ν_3-fundamental photons with 1/5 eV energy are emitted per visible photon, in an emission band of halfwidth 0.7 μm. The spectral radiance near 6.2 μm viewing normal to Orbiter ram surfaces would thus be about

$$(([2 \times 10^9] \times [6] \times [1/5])/[0.7]) \times [1.6 \times 10^{-19} \text{ watt sec/eV}]$$
$$\approx 5 \times 10^{-10} \text{ watts/cm}^2 \text{ ster } \mu\text{m}.$$

This example foreground-contamination radiance may be compared with a) some astronomical backgrounds:

$$1 \times 10^{-10} \text{ watts/cm}^2 \text{ ster } \mu\text{m}$$

in the ecliptic plane at 45° solar elongation from zodiacal light, and

$$0.05 \text{ and } 0.2 \times 10^{-10} \text{ (average) watts/cm}^2 \text{ ster } \mu\text{m}$$

outside and within the galactic plane respectively; and b) the atmospheric thermal background:

$$10^{-10} \text{ and } 10^{-11} \text{ watts/cm}^2 \text{ ster } \mu\text{m}$$

at a tangent intercept altitude of 220 km (i.e., in the limb) and in the zenith from that altitude (due to the H_2O ν_2 band; see Ref 57). Where the brightness of the glow induced by passage of the spacecraft is first order in the ambient density of atomic

oxygen, this example can be directly scaled to other orbital altitudes using model-atmospheric [O].

These brightness estimates implicitly assume that all surface-catalyzed recombination proceeds through electronically excited states of NO_2 only, as in homogeneous NO + O reactions. Direct recombination into vibrationally excited $^2A_1$--for example at surface sites with complex-activating characteristics different from those causing recombination with exit channels favoring $^2B_2$ and $^2B_1$--would of course lead to higher ratios of infrared to visible column intensity. (This takes place in the reactions of NO with O_3, which is the principal reason that these are also reviewed here.) Heterogeneous surface-catalyzed recombination into a vibrationally-excited ground electronic state has been identified in CO_2 (Ref 58), CO (Ref 59), and N_2 (Ref 60). In consequence the photon ratios in Table 3.2 and the 6.2 μm-bands radiance estimated above may be lower limits to the actual infrared emission from $NO_2^\dagger$ off surfaces of Shuttle Orbiter.

$NO^\dagger$: Origin

While no measurements have been made of rates of recombination of N with O into excited states of NO on spacecraft surfaces, evidence exists that this process can take place on at least some of the materials exposed in low earth orbit--including Shuttle's glass ceramic tiles. Nitrogen atoms have been found to have high probability of recombining with oxygen atoms on metallic interior surfaces of satellite mass spectrometers (Ref 42), and indeed atmospheric N usually converts to NO (and perhaps other molecules) in spaceborne pressure gages with glass or metal walls (Ref 27). In the laboratory, as discussed in Section 2, these two species recombine into nitric oxide molecules in a single electronically excited state at room temperature on several polycrystalline metals (Ref's 34, 36) and glass (Ref 36). The process may be "direct", or may proceed by way of the potential curve-crossing path of the homogeneous recombination indicated in Figure 2.1. (The absence of detectable recombination-indicating optical radiations off teflon

surfaces (Ref 34) is most likely due to this saturated polymer's commonly-applied property of inhibiting reactions or deactivation at laboratory chamber walls.)

The radiation from this NO $B^2\Pi$ recombination state fits the measured (Ref's 19, 20) ultraviolet component of the Atmosphere Explorer ram glows, as was described in Section 2. Applying the laboratory spectral distribution to these Atmosphere Explorer data leads to a total perpendicular-column intensity of 2×10^{11} photons/cm^2-sec in the complete β-band (B⇒X) system at 140-145 km orbital altitude. (This is at least two orders of magnitude less than the incident flux of N atoms.) The laboratory reports (Ref's 34, 36) present no information about the absolute yields in these ultraviolet bands when N and O are flowed to the surfaces investigated, and thus provide no guidance for estimating the rates of excitation of NO(B) by the materials exposed on spacecraft. (The absolute radiances the ensuing infrared cascade glow can be determined from the brightness ratios calculated here when better information about these excitative recombination rates becomes available.)

As discussed in Section 2, excitation of the $A^2\Sigma^+$ and $C^2\Pi$ states of NO--the upper states of the γ and δ bands otherwise familiar from homogeneous recombination--was not detectable in the heterogeneous-recombination experiments (Ref's 34, 36). Were these states populated through the aforementioned curve-crossing fewer infrared photons would be produced than from the B state, since their internuclear separations line up more closely with those of the ground electronic state and therefore the average vibrational excitation of NO(X) would be lower--: by about factor 3, as Figure 2.1 shows. Similarly radiation originating from the $a^4\Pi_i$ and $b^4\Sigma^-$ states is absent or weak in homogeneous recombination; and furthermore, if NO(b) molecules were to desorb their 6-sec lifetime would result in such long radiative paths that the near-infrared b⇒X bands (Table 3.1) would almost certainly be experimentally undetectable.

We applied the relative intensities of the NO β-bands from laboratory metallic surface-catalyzed reactions (Ref 34) to calculate the relative cascade infrared radiances from $NO^{\dagger}$ (X, v" > 0) that would arise from NO(B, v'). (That is, we assume the same vibrational distribution in excitations at surfaces of spacecraft.) The initial populations in the zeroth to third vibrational states of $B^2\Pi$ were found from an analysis of the emission spectrum to be in the ratios 1:0.23:0.22:0.21 (Ref 34). The distribution in vibrational states of NO(X) that we derived is given in Figure 3.1, along with the theoretically-calculated (Ref 61) radiative lifetimes of $NO^{\dagger}$ in these states. Results of our calculations, and the radiative pathlengths, are in Table 3.3.

No attempt was made in these laboratory experiments to measure the initial vibrational excitation distribution of, or for that matter the total rate of recombination into, the ground electronic state of NO. Should recombination into NO(X, v > 0) be taking place--as is altogether probable--, the relative infrared radiances that we estimate here would again be lower limits.

$NO^{\dagger}$: Infrared Emission

The horizontal offset of the potential curves of the B and X states of NO results (through the Franck-Condon factors; refer to Figure 2.1) in an average vibrational quantum number v" of about 7 after the β-band photon has been emitted. We calculated the numbers of photons emitted in the fundamental and overtone bands from this vibrational distribution and the branching ratios derived from the radiative lifetimes plotted in Figure 3.1, with the assumption that collisional deactivation (or upward pumping) by the atmosphere plays no part in the cascade to the ground vibrational level. The result is that 5 ± 1 fundamental-sequence (extending above 5.3 μm) and 1 ± ½ overtone-sequence (near 2.8 μm) photons follow each surface-catalyzed recombination into NO (B, v' as in Ref 34). These error estimates are based on the uncertainties in the distribution in population of NO(X, v') and the theoretically-derived (Ref 61) Einstein coefficients for $\Delta v = 1$ and 2 transitions

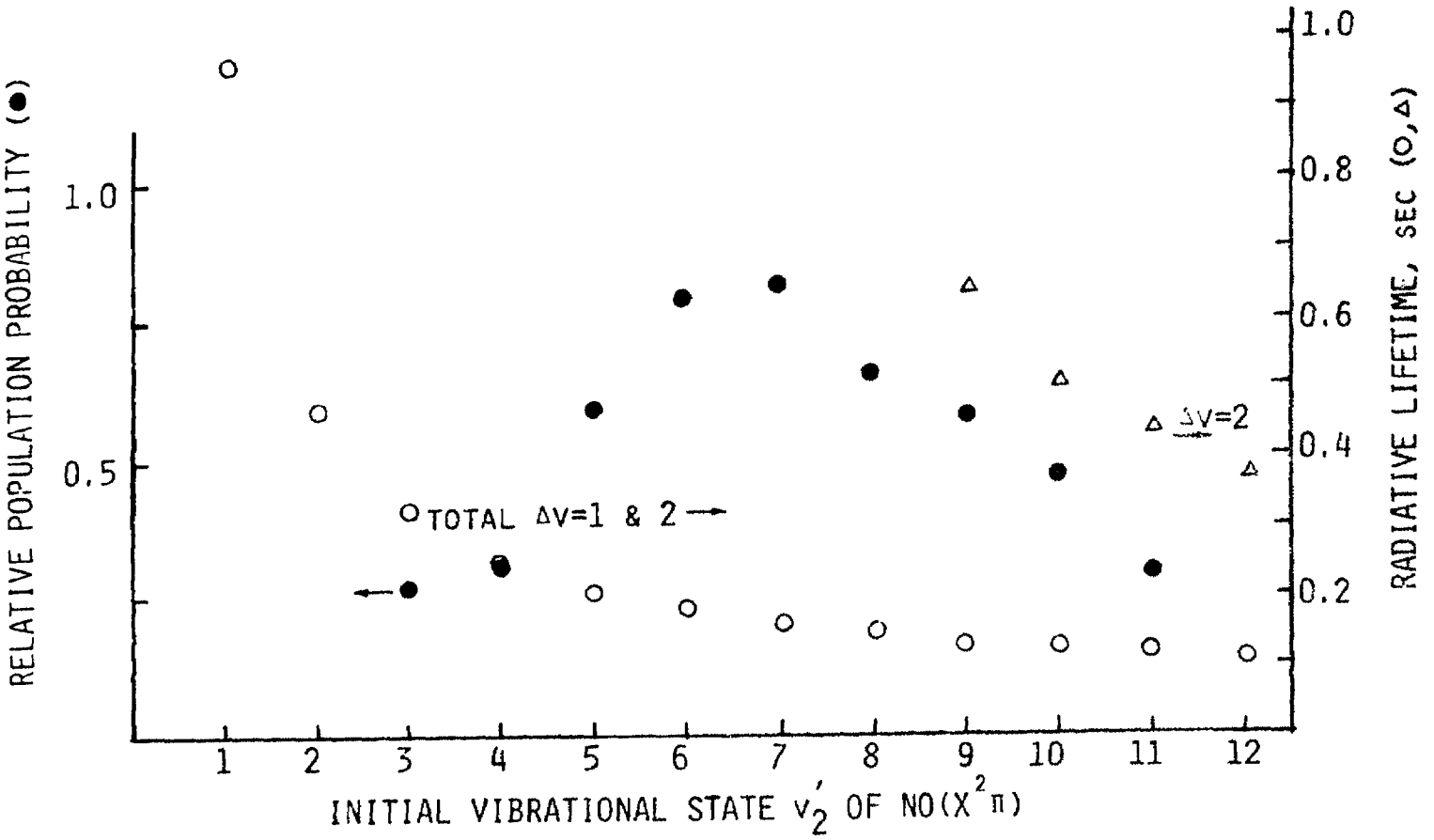

Figure 3.1. Distribution of population in vibrational states of NO(X), and radiative lifetimes.

in the ensuing cascade. As noted immediately below, the long radiative lifetimes of vibrationally-excited nitric oxide can in fact result in some further redistribution of the vibrational state populations by collisions with the atmosphere's atoms and molecules, which introduces further error into these estimates of the infrared yields.

Again, because of the anharmonicity of the ground electronic state potential the longer-wavelength photons within each of the two infrared sequences tend to be emitted closer to the catalytic surface than the shorter-wavelength photons. From the radiative lifetimes plotted and mean thermal-effusive velocity of the NO molecules, we find that the characteristic lengths for each unit decrease in vibrational quantum number are about 50/(upper vibrational state) m. Thus the effective volume from which the vibrational manifold is emitted extends roughly 100 m from the recombination surfaces [at altitudes where the atmosphere fails to confine and/or react with the desorbate molecules]. Since over so large a distance the $NO^{\dagger}$ "beam" from real spacecraft would exhibit substantial lateral divergence--refer again to Section 5--, the infrared photon radiances in projections perpendicular to even the largest-area surfaces would be substantially less than the UV (β-band) radiances; expressed in energy units, the relative IR brightnesses would of course be still lower.

At low shuttle operational altitudes the radiatively long-lived desorbate molecules lose momentum in collisions with the atmosphere, so that the emission pattern is less widespread than indicated in Table 3.3. Furthermore, at low collision energies oxygen atoms quench NO vibrational states with almost gas-kinetic cross-sections; and some upward pumping can also be expected at the actual high relative translational energies. In consequence the infrared emission yields and glow volume dimensions presented here become increasingly less accurate at flight altitudes below about 240 km, where the collisional mean free path approaches the 100-m radiative path estimated in the previous paragraph.

Table 3.3. NO infrared and ultraviolet radiations

Reaction Sequence	Wavelengths	Photons / Reaction	Characteristic Outward Length
N + O $\xrightarrow{\text{Surface}}$ $NO(B^2\Pi, v_2')$;			
$NO(B) \longrightarrow NO(X^2\Pi, v_2')$	~0.24-0.4 μm	1	~1 mm
+ 3 bands:			
$NO(X, v_2') \longrightarrow NO(X, v_2'-1,-2)$	2.7 - 3.1 μm (overtone)	1 ±1/2	Several 10's m; refer to text
+ vibrational bands cascade	& 5.3 - 5.9 μm (fundamental)	5 ±1	

These calculations have been made under the assumption that the initial vibrational population distribution in NO(B) that was measured under limited laboratory conditions (polycrystalline transition metals at 293K) applies in general to recombination of atmospheric N and O atoms on the outermost surfaces of spacecraft. Nonetheless if (for example) only the zeroth vibrational level of NO(B) is initially populated--as in the frozen-matrix experiments mentioned in Section 2--, the number of fundamental-band photons per surface recombination reaction in fact changes very little. (This outcome is indicated by the potential curves in Figure 2.1.) The ratios of infrared to β-band photons estimated here of course apply only for those substrates on which the rate of surface-catalyzed recombination of N with O reaction into NO(B) is substantially greater than the rate of their direct recombination into upper vibrational levels of NO(X). Direct recombination into vibrationally-excited ground-state nitric oxide, which would of course increase the relative infrared glow intensities, can be investigated in the laboratory (and also the near-space environment) by tuned laser-pumping methods.

Radiations from O_2

As Figure 2.1 shows, the low-lying $a^1\Delta_g$ and $b^1\Sigma_g^+$ states of O_2 correspond to two O^3P (ground-state) atoms. These electronic states are believed to be populated in surface-catalyzed recombination of O, insofar as recombination into them takes place in the gas phase (for example in the earth's nightglow at altitudes near 100 km) and they appear to be intermediates in some off-surface reactions in the laboratory. However even were the excitation probabilities extremely high, the brightnesses of the resulting spacecraft glows would be low because of the long radiative lifetimes of O_2(a) and (b), 3700 sec and 12 sec respectively. (The near-infrared nighttime and twilight airglows from these metastable molecules are readily detectable because the radiating volumes fill the typically-wide sensor fields of view and the two states are

only slowly depopulated by collisions at the altitudes where they are excited.)

Any O_2 a→X radiation (Infrared Atmospheric bands, with the 0,0 at 1.27 μm) excited by spacecraft surfaces would virtually certainly be below measurement thresholds. In contrast some possibility exists that the more rapidly-emitted b→X radiation system (Atmospheric bands, whose 0,0 and 0,1 transitions are at 0.76 and 0.88 μm) could be radiometrically detectable at the lowest orbital altitudes, where the oxygen molecules are confined by collisions. The quenching probabilities are only $\sim 10^{-5}$ per collision near 300K, and if this low ratio applies also at the higher relative velocities of desorbates, the ram glow volume--containing principally backscattered $O_2(b)$ molecules--could have sufficient surface brightness to be detected. A detailed particle transport calculation would be required to assess the altitude profile of column intensity of this very near-IR glow, for assumed rates of surface recombination $2O \rightarrow O_2(b)$.

Radiation from O_3

Despite the high incident fluxes of O and O_2 and the known propensity of both species to adsorb on many materials, desorption of excited O_3 from spacecraft is improbable: as this bonding is in general greater than the 1.1-eV dissociation energy of $O_3(\tilde{X}^1A_1)$, the substrate tends to pull the molecule apart before it can escape. This is evidenced by the absence of laboratory observations of ozone production by surface catalysis: surfaces typically destroy rather than create this weakly-bound species.

If however $O_3^\dagger$ were to form on surfaces of orbiting spacecraft, the most probable excitation mode would be the asymmetric stretch (ν_3), as trajectory calculations for other triatomic molecules (Ref 30) indicate that this mode is favored in (at least) Rideal-Eley recombination processes. The radiative lifetime of O_3 (001) is 0.096 sec, and thus the radiative path for the fundamental-bands cascade (..., 003→002, 002→001, 001→000) that

extends from about 9.6 to 11.5 μm would be approximately 2 x (0.1 sec x 400 m/sec) $\approx$ 80 m. [We have again assumed equilibrated effusive desorption of the mass-48 species at typical spacecraft surface temperatures.] Overtone radiation is one or two orders of magnitude less probable. This long radiative pathlength further limits the brightnesses of any glow from $O_3(\nu_3)$ that may be excited at spacecraft ram surfaces.

(Should ozone molecules in the ground state desorb, their 6-9 eV center-of-mass kinetic energy collisions with O and N_2 would be expected to excite the few tenths-eV states of the asymmetric stretch mode. The earth limb background near 9.6 μm at 220 km tangent altitude is much lower than at 5.3 μm, $\leq 10^{-13}$ w/cm^2-ster-μm (Ref 57); the astronomical backgrounds are near those at 5.3 μm stated above.)

Radiations from N_2

Some electronic excitation accompanies the recombination of nitrogen atoms on polycrystalline metals, as is indicated by the off-surface emission of yellow-red First Positive (B$\rightarrow$A) bands of N_2 seen in the laboratory (Ref's 36, 62-64) as well as the ultraviolet Lyman-Birge-Hopfield (a$\rightarrow$X) bands identified from spacecraft (Section 4). (N also recombines into vibrationally excited $N_2(X)$ (Ref 60), which having no permanent electric dipole moment does not radiate.) The product vibrational state distribution is known to be sensitive to the structure of the laboratory recombination surface and, in particular, its impurities. The partial listing of First Positive Band heads in Table 3.4 shows that the sequences originating from up to the fifth vibrational level extend into the near infrared. However, the most intense First Positive bands observed in the above-referenced experiments were found to originate from the sixth to eighth vibrational levels of the $B^3\Pi_u$ state; in consequence little near-IR radiation would be expected from this band system itself off the catalytic surfaces that were investigated. (The spectrometers used in the laboratory work were not sensitive to the bands at wavelengths $\geq$7000 Å.)

Table 3.4. Heads of First Positive ($B^3\Pi_g \rightarrow A^3\Sigma_u^+$) bands of N_2 (in μm)*

v'/v"	0	1	2	3	4	5	6	7	8	9
0	1.05200(10)									
1	.89124(10)									
2	.77532(6)	.87223(8)	.99420(2)							
3	.68750(2)	.76262(7)	.85416(6)							
4	.61868(3)	.67886(6)	.75039(7)	.94364(3)						
5	.56327(1)	.61274(3)	.67048(8)	.73866(5)	.82048(3)	.92039(2)				
6		.55929(1)	.60697(7)	.66236(9)	.72733(3)	.80474(2)				
7			.55537(1)	.60136(7)	.65448(10)	.71648(2)	.78964(2)			
8				.55156(2)	.59060(8)	.64685(10)	.70590(2)			
9					.54785(2)	.59060(8)	.63947(9)	.69678(1)		
10						.54423(3)	.58544(8)	.63229(7)		
11							.54071(3)	.58043(7)	.62528(3)	
12							.50308	.53728(3)	.57552(7)	.61852(3)

*Approximate relative intensities in discharges appear in parentheses. Einstein coefficients are given in Ref 65.

On the other hand if the $N_2(B)$ state is excited indirectly, as expected, some infrared photons may be emitted by its precursor species. The interpretation of the laboratory experiments is that these precursor molecules transfer to the B state by collisions with the relatively dense off-surface gas. In the space environment, in contrast, the much lower ambient densities would favor transfer by radiation. Two triplet precursor states of $N_2(B)$ have been proposed: $A^3\Sigma_u^+$ with high vibrational excitation, which would result in little or no such infrared radiation; and $W^3\Delta_u$, which would produce the near-infrared Wu-Benesch (W→B) bands.

The laboratory off-surface glow was initially interpreted (Ref 36) as due to direct association of two $N(^4S)$ atoms into the long-lived $N_2(A)$ state. (Refer again to the potential diagram in Figure 2.1.) Collisions then convert these molecules to $N_2(B, v \approx 6\text{-}8)$, which having closely 6 μsec lifetime move about 2 mm on the average (at room temperature) before radiating. In the space environment $N_2(A)$ in vibrational states ≤ 8 would radiate the ultraviolet A→X (Vegard-Kaplan) bands, in lifetimes about 2 sec and thus pathlengths about 1 km (as noted in Section 2). From higher vibrational states, the near-infrared A→B (Reverse First Positive) bands are expected on theoretical grounds (Ref 65); the radiative lifetimes range from 2 sec at $v = 9$ to 1/6 sec at $v = 12$ to an extrapolated (from Ref 65) $\sim 10^{-3}$ sec at vibrational levels near the dissociation limit. These N_2 A→B bands, however, have so far not been observed in the laboratory. Furthermore, if very high vibrational states of $N_2(A)$ are populated by recombination at spacecraft surfaces these long radiative lifetimes would result in low brightnesses of this putative Reverse First Positive glow.

The more recent laboratory emission spectra (Ref 63) were interpreted as due to $N_2(B)$ formed from off-surface collisions of $N_2(W)$ molecules that are produced in vibrational states near the eleventh by the surface reaction. (The recombination process involves potential curve-crossing from the $^5\Sigma_g^+$ state; see again Figure 2.1.) In near-space where this collisional transfer is highly improbable these $N_2(W)$ molecules would radiate (principally)

Wu-Benesch bands, at the infrared wavelengths and with the lifetimes shown in Table 3.5. (The band locations are estimated from a compilation made in connection with a Defense Nuclear Agency project (Ref 66)). The off-surface extents of this near- and short wavelength-infrared W→B glow would be about 5 cm, which [again assuming effusion at the surface temperature] is about the same as that of both the ultraviolet N_2 (a→X) glow (Section 4) and the visible pseudocontinuous glow from desorbed NO_2^*.

Additionally, as Table 3.5 shows, if $N_2(W, v \approx 11)$ molecules are produced at spacecraft surfaces most of the ensuing B→A radiation (which as noted above is emitted within a very few mm of the W→B) would originate from the fourth, fifth, and sixth vibrational levels. As is shown in Table 3.4, some of the First Positive Bands from these upper states are at very near-infrared wavelengths.

To summarize: --if 2N → desorbed $N_2(W, v \approx 11)$, the resulting triplet cascade emission will consist of 1) near- to short wavelength-infrared (W→B) bands; 2) very near-infrared (B→A) bands (both 1) and 2) extend out about the same distance as the ultraviolet N_2 and visible NO_2 glow regions); and 3) the much more widespread ultraviolet Vegard-Kaplan (A→X) bands.

The sole evidence for N_2 B→A radiation off ram surfaces comes from Spacelab I spectrographic data (Ref 67), which are identified as provisional and furthermore lack a reference spectrum of the underlying natural atmospheric airglow. The wavelengths of the individual emission peaks in these published spectra have at best only a fair correlation with the First Positive bands expected (see in particular Figure 5 of Ref 67). Furthermore, the resolution-degraded spectral distribution is more representative of that from electron impact on N_2 in the ground state--which produces a redder glow, as pointed out in Ref 1--than from gas-phase recombination of N atoms. This suggests that the B→A radiation observed may be due to dayglow (which is excited largely by impact of photoelectrons). Still further, banded structure has not been resolvable below the NO_2^* pseudocontinuum in other spacecraft glow spectra (Ref 17),

Table 3.5. Computed radiative lifetimes* (μsec, upper entry) and estimated bandhead wavelengths** (μm, lower entry) of N_2 Wu-Benesch bands

v" =	2	3	4	5	6	7	8	To all states
v'=9	950	370	308	703	12000	140000		118
(Low)†	0.9	1.32	1.70	2.33				
v'=10	1627	500	284	340	1240	140000		101
(Moderate)		1.	1.37	1.82	2.50			
v'=11	3154	768	328	256	436	2800	300000	89
(High)			1.	1.43	1.95	2.70		
v'=12	6000	1282	441	254	268	657	9500	80
(Low)				1.1	1.48	2.09	2.94	

*Inverse of Einstein coefficient from Ref 65.

**Extrapolated from data for v'=0-7, v"=0-8 provided by Ref 66. The third figure is uncertain.

†Relative probability of surface excitation from Ref 63.

which indicates that it has at least a factor 5 less mean intensity. In consequence the presence of N_2 First Positive bands and--should excitation of the B state be through the W state of N_2--the longer wavelength infrared Wu-Benesch bands, remains hypothetical.

Summary

Applying the assumptions that the initial population in excited states from spacecraft surface-catalyzed formation of NO_2 is that of the NO + O + M reaction (largely justified by the close similarity of the pseudocontinuous visible spectra), and of NO is that of the N + O reaction on laboratory metal surfaces (plausible on the basis of the inferential data presented here and in Section 2), we find that about 5 SWIR-MWIR photons are emitted following each recombination. Tables 3.2 and 3.3 identify the infrared rovibrational bands of the two odd-nitrogen species, from a review of the literature on their spectroscopy and excitation in laboratory gas-phase reactions. The absolute radiances from NO_2 can be reliably estimated from the existing spacecraft glow data. In contrast estimates of absolute intensities in the NO fundamental and overtone bands await measurement of the yields of β-band radiation in orbit (or at a minimum, in the laboratory). The relatively long lifetimes of NO(X, v) lead to alterations of the spatial pattern of the IR emission from these excited molecules at very low orbital altitudes, where they are collisionally scattered and deexcited/reexcited by the atmosphere.

The longer radiative lifetimes of vibrational states result in much further outward extents of these infrared glows than of glows in most visible or ultraviolet electronic bands. Thus (following Section 5) the infrared radiances are generally lower; and conversely, the IR-emitting volumes are considerably larger. A sample calculation shows the perceived highest-radiance infrared feature of NO_2 or NO--the NO_2 ν_3 bands centered near 6.2 μm--to be brighter than both most astronomical backgrounds and the atmosphere's limb at the typical operational altitudes of space

shuttle. [We have assumed throughout this Section that the excited molecules desorb effusively at typical spacecraft-surface temperatures.]

Laboratory experience definitely does not preclude the possibility that the ground electronic states of these two species can be directly populated by surface recombination, at subsets of active sites chemically different from those from which the principal desorbate exit channel produces the NO_2 $^2B_2$ or $^2B_1$ or NO $^2\Pi$ states that we have considered. Such direct excitation of vibrational states would of course increase the ratios of infrared to visible or ultraviolet glow brightnesses that are estimated in Tables 3.2 and 3.3; however such a process would not dramatically change the spectral distributions and ratios of total intensities of rovibrational IR features.

We have also considered the infrared radiations from recombinant O_2^* and $O_3^\dagger$, which would be weak because of the long radiative lifetimes and perceived low rates of surface reaction respectively; and from N_2^*, which laboratory experience suggests could be modestly strong. In particular, the N_2 Wu-Benesch bands (Table 3.5) may like the Lyman-Birge-Hopfield bands (Section 4) be excited by recombination of the atmosphere's nitrogen atoms; if so, the near- and short wavelength-infrared glow would have closely the same off-surface extent as the N_2 Lyman-Birge-Hopfield and NO_2^* pseudocontinuum glows, and in addition would be accompanied by some near-infrared emission in the N_2 First Positive bands. As this surface recombination process is still speculative (and so far not directly detected, or inferrable from the spacecraft data at visible wavelengths), we have not attempted to estimate the infrared radiances in these bands of the nitrogen molecule triplet cascade.

SECTION 4

EXCITATION OF NITROGEN LYMAN-BIRGE-HOPFIELD BANDS EMISSION AT SURFACES OF ORBITING SPACECRAFT

Background

On the basis of the limited preliminary nadir vacuum ultraviolet spectra from AFGL's polar-orbiting S3-4 satellite (Ref 68), we hypothesized that the N_2 Lyman-Birge-Hopfield radiation (LBH, $a^1\Pi_g$ [low v']$\rightarrow X^1\Sigma_g^+$) seen at night at latitudes other than where aurora occur is an artefact of the passage of this spacecraft through the thermosphere (Ref 1). We postulated that the excitation process is excitative recombination of ambient $N(^4S)$ atoms catalyzed by the exposed ram surfaces, in analogy with the recombination of NO with O that produces the visible-continuum spacecraft glow from NO_2^* (Ref's 1, 17).

A recent analysis (Ref 22) of the radiant intensities measured in further orbits of S3-4 verified that the glow is indeed an experiment artefact, and interpreted this contaminant emission as due to high kinetic-energy impacts of atmospheric N_2 on the fast-moving spacecraft surfaces or on other N_2 molecules physisorbed on them. (In the interim the optical signal had been identified as due to season-dependent midlatitude airglow, with interaction between the vehicle and atmosphere expressly ruled out as its cause (Ref 69)). Spectrally-similar glows, readily identifiable as LBH bands, were measured from Spacelab 1 in a circular orbit at 1/3 to 2 scale height lower ambient density than the S3-4 measurement range (Ref 23); in contrast this emission was undetectable in a single spectrum from a Shuttle Orbiter at about two further scale heights lower total air density (Ref 70), or in the various past sounding rocket measurements of the VUV radiations from the night-time non-auroral thermosphere.

In this Section, we show that the relative population of $N_2(a)$ vibrational states that was measured from S3-4 and Spacelab 1 is

indeed consistent with the population resulting from recombination of ground-state nitrogen atoms in the gas phase, and furthermore that the kinetic energy available from the 7.8-7.9 km/sec mean velocity of the atmosphere relative to the very low altitude-orbiting spacecraft is insufficient to excite $N_2(X)$ to $N_2(a)$ directly. The heterogeneous (surface-catalyzed)--and most probably, Langmuir-Hinshelwood--reaction is analogous to the homogeneous reactions that produce the well-known VUV afterglow of "active nitrogen" in the laboratory. We also review possible causes of the observed very strong dependence of the nadir LBH-system intensities on the ambient density of $N(^4S)$, which change by almost two orders of magnitude over the data range while [N] varies over only about a factor 2 (refer to Figure 4.1). The most promising explanations include promoting/interfering surface-reaction processes involving the much more abundant other incident aeronomic species (which have the effect of "conditioning" the surface); generation of excess concentrations of N by gas-phase reactions of reflected N_2 or O with incident O or N_2; and undocumented systematic changes in the space vehicle's orientation to the airstream.

Data from S3-4 and Other Sources

The 96½°-inclination S3-4 satellite (Ref 68) crossed the equator at 2230 LT (ascending) and 1030 LT, in an approximately 270 x 160 km orbit with apogee at an unspecified high southern latitude. (The altitudes are known to have varied among orbits over the data period.) Particulars of the vehicle's surface configuration and materials have not been made available, as its mission was performed principally for purposes other than remote characterization of the atmosphere. Furthermore, despite the nominal three-axis stabilization of the spacecraft, constancy of its orientation to the airflow has not been verified. In consequence the artefactual spectral radiance data reported preliminarily in Ref 68 and in more detail in Ref 22 represent a set of empirical observations rather than results of a controlled,

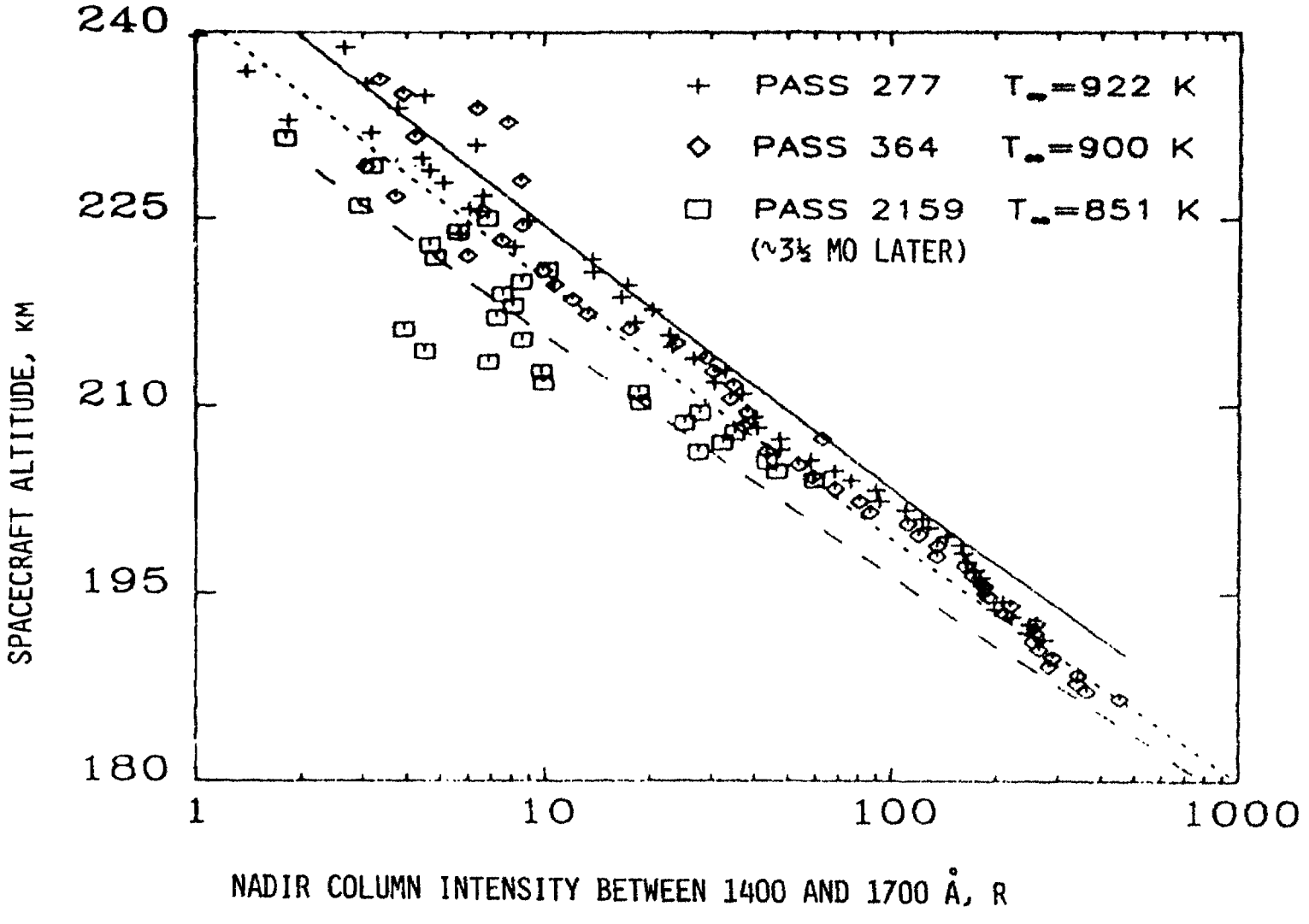

Figure 4.1. Nadir spectral intensities summed between 1400 and 1700 Å from three nighttime passes of S3-4. T_∞ is the MSIS-83 model exosphere temperature, and the three straight lines plot [model N_2]^3 x (3.3 x 10^{-27}) (adapted from Ref 22)

dedicated experiment. Additionally, while a diagram of the spectrometer's baffled sunshield is available (Figure 1 in Ref 68), the absence of information about the geometry of the host vehicle and its other payload elements within a few LBH-radiative pathlengths from this instrument's field of view---20 cm if the $N_2(a)$ molecules desorb at surface-thermal (effusive) velocities--precludes quantification of the absolute radiation "yields" at known incident fluxes of N and the more-abundent other atmospheric species: that is, the radiation output per "arriving" air particle can be only estimated.

The data set analyzed in Ref 22 consists of

1) nadir photon intensities summed between 1400 Å and 1700 Å, which are reported for four orbit segments through tropical and then northern middle latitudes as the instrument's altitude was decreasing from 239 to 183 km (three of these profiles are in Figure 4.1); and
2) the spectral distribution (at ~25 Å resolution) between 1400 Å and 1650 Å, averaged over 23 such passes in the four months after the northern-hemisphere vernal equinox.

As Figure 4.1 indicates, the scale heights of the column intensity 1) are near 10 km above ~195 km, and become about 20% larger when the instrument was below that altitude; this increase is in the direction of that of the scale height of $[N^4(S)]$. The altitude profiles in Figure 4.1 were interpreted in Ref 22 as showing that the absolute magnitudes and scale heights of this clearly not aurora-associated LBH emission increase with the exosphere temperatures calculated from the MSIS-83 atmospheric model, and thus with the density of the thermosphere in which S3-4 was orbiting.

A closer inspection of Figure 4.1 shows, however, that the LBH-band intensities at the two higher temperatures that were inferred (i.e., calculated from the measured geophysical parameters flux of 10.7-cm solar radiation, global magnetic activity index, solar zenith angle, and latitude/longitude/time) are indistinguishable at spectrometer altitudes below 200 km and above 220 km; and that the data for the third (lowest) exosphere temperature are not

only very noisy and confined to an only 26-km range of measurement altitudes, but were taken after the spacecraft had been exposed to the orbital environment for a further 3½ months--during which the composition and microstructure of its outermost surfaces may have changed enough to account for the different profile. (No mention of a change in emission spectrum distribution over the data period appears in Ref 22). In any case, the order of any dependence of column intensity on the concentrations of upper-atmospheric species that were calculated using the inferred exosphere temperature--all of which would be expected to increase with this temperature--cannot be reliably determined from the data presented in Figure 4.1 and elsewhere in Ref 22.

At the about-average 900K exosphere temperature the scale heights of [O], [N_2], [O_2], and [NO] are closely 45, 26, 24, and 24 km respectively; and the scale height of [$N(^4S)$] is 50-60 km above 195 km and increases below that altitude as the N-atom concentration approaches the profile maximum. ([N] at fixed altitudes becomes larger as the satellite moves westward nearer to local sunset [see for example Ref 71], where fewer N atoms have been consumed by reacting with the atmosphere's O_2 molecules. However the small change in longitude of the satellite over the relatively low-latitude data periods of S3-4 results in only a minor such "diurnal" increase.) Thus within their experimental variability the scale heights of the wavelength-integrated nadir spectral radiances can be fit by

$[N_2]^2 \cdot ([N_2]$ or $[O])$, or even

$[N_2]^2 \cdot ([NO]$ or $[O_2]$ or $[N])$, as well as by

$[N]^2 \cdot ([NO]$ or $[O_2])$, or even

$[O]^4$

and other products of concentrations of ambient species instantaneously incident on the spacecraft. The highest total LBH system intensities are about 1 kilorayleigh or 10^9 photons/cm^2-col-sec (see Figure 4.1; about half the model system photons lie within the 1400-1750 Å range of the data) where the flux of N atoms to surfaces normal to the velocity vector is ~10^{13}/cm^2-sec or a

factor 10^4 higher; thus the rate of arrival of N atoms may be considered sufficient to support the measured column brightnesses at all spectrometer altitudes. (More on this important issue later.) However if the rate-limiting step were to involve only nitrogen atoms, the altitude dependence would be represented by $[N]^{5 \text{ or } 6}$, a high reaction order that has not been previously observed in laboratory experiments involving surface-catalyzed recombination of a single incident species.

Fits to synthetic spectra in Ref 22 showed that while most of the LBH radiation arises from low vibrational levels of $N_2(a)$, there is still significant excitation of v' = 4 and 5 (one-quarter of all v's), and--equally important--that the initial-state population does not decrease monotonically with v'. The orbit-averaged VUV spectrum does not have sufficient resolution to rule out 5-10% v' = 6, whose population was in fact identified in the initial report on the UV radiation observed at midlatitudes from S3-4 (Ref 68). This vibrational distribution differs markedly from that resulting from impact of ~keV's electrons on low-pressure nitrogen or air (where the average v' is higher), and thus the midlatitude glow would not be caused by precipitating electrons. Further, the LBH spectrum shows no effect of Schumann-Runge-band attenuation by the atmosphere's O_2 molecules, which would be evident if the $N_2(a)$ molecules were excited at altitudes more than a few 10's km below the spacecraft.

A limited set of VUV data from Spacelab 1's nadir- or limb-pointing "ISO" spectrograph that has been reported (Ref 23) also indicates the presence of artefactual LBH-band radiation. The relevant observation from the five equatorial plus midlatitude nighttime sequences now available is a similar enhanced population of low vibrational states, with individual bands having v' up to only 6 well resolved in the spectra. The total (wavelength-integrated) column brightnesses show an inconsistent dependence on the tangent intercept altitude of the instrument's field of view, and furthermore the intensities of LBH bands originating from the same v' show no clear pattern of Schumann-Runge absorption by O_2

between the atmosphere's nightglow layers and Shuttle Orbiter's position; these two observations provide further evidence that this VUV radiation is also an artefact of the vehicle's passage through the thermosphere.

The limb spectral intensities measured from Spacelab suggest a diurnal effect of the type that would be caused by the aforementioned change in [N(^{4}S)] with longitude at the 250-km orbital altitude. Average radiances between 1600 Å and 1700 Å were 50 R/Å near 2000 LT (Figure 4 of Ref 23), 25 R/Å near 2030 LT (Figure 5), and decreased to 10 R/Å near 0330 LT (Figure 3). In contrast no consistent trend can be identified in the two nadir spectra, which like the others are relatively noisy. However, the total LBH system column intensities from Spacelab are as much as three orders of magnitude higher than would be derived by simply extrapolating the altitude profiles shown in Figure 4.1. This discrepancy may perhaps be explained by the provisional status of the data reported from the relatively-untested "ISO" spectrograph, or alternatively it may be due to the mechanism for creating excess nitrogen atoms near spacecraft discussed later in this Section.

This midlatitude VUV emission was not detectable (Ref 70) in the spectrum from later space shuttle Columbia (STS 61-C, January 1985), which was orbiting at 370 km. (The local time of this measurement was not reported.) The instrument had nominal threshold sensitivity 1 R/10 Å, and was pointed at a MgF_2-coated parabolic focusing mirror directly exposed to ram. This result would be expected if the column intensities from S3-4 could be extrapolated to Columbia's higher altitude and applied to the undoubtedly-different configuration of the surfaces of its spectrometer and the structures near it.

Previous Interpretation of the LBH Glow

The approximate fit of LBH intensity to (instantaneous) $[N_2]^2$·([N_2] or [O]) and the preponderance of low upper vibrational states in the composite emission spectrum, form the basis for Ref 22's interpretation of this glow as a direct result of the

translational energy of ambient N_2 molecules relative to either ram surfaces or other N_2 molecules weakly adsorbed on these surfaces. (Physically-reasonable reaction rates in a three-step excitation process are recognized in Ref 22 as falling short by very many orders of magnitude of being able to account for the observed mean glow intensities.) Assuming the atmosphere's N_2 molecules to be at rest, this "relative kinetic energy" would be ¼ eV at apogee of S3-4 and ½ eV at its perigee above the 8½-eV threshold for exciting v' = 0 of $N_2(a)$. (The vibrational spacing below v' = 6 in this electronic state is closely 2/10 eV; refer to Figure 2.1.)

The kinetic energy available for internal excitation in reactive scattering must of course be figured in the center-of-mass system of the collision participants. We consider first impacts of atmospheric $N_2(X)$ on $N_2(X)$ adsorbed on ram surfaces. (The weak bonding of nitrogen molecules to all but a very few special catalysts--principally metals--would in any case lead to low fractional dinitrogen coverage.) While physisorption or chemisorption have the effect, in simple terms, of forming complexes with somewhat higher "effective mass" than gaseous N_2, the median energy available for chemical reaction is still only a little more than <u>half</u> the translational energies stated in the previous paragraph. The natural thermal motion of the atmosphere's atoms and molecules increases or decreases their kinetic energy in the spacecraft's rest frame (as has been noted in the context of vehicle glow in Ref 72). However, the fraction of the arriving N_2 molecules that have more than twice 9 eV energy at 185 km with 900K exospheric temperature is only about 10^{-12}. (This calculation from the Maxwell velocity distribution neglects the (variable) meridional-wind velocity, the effect of which would be small.) Even in the extremely implausible event of complete monolayer adsorbate coverage, the cross section for collisional excitation to $N_2(a)$ at this essentially thermoneutral condition would have to be 10^4 geometric to produce the observed total LBH system intensity [assuming that the two quantities (column emission rate in the nadir direction) and (particle flux to the ram surfaces) can be

directly compared]. Such a cross section is several orders of magnitude higher than would be inferred from the experimental and theoretical results on electronic excitation in collisions of N_2 on N_2 (Ref 73) and between neutral species having other interaction potentials (as reviewed in Section 6). In consequence the proposed idea that ramming molecules can directly collisionally excite adsorbed $N_2(X)$ to $N_2(a)$ can be discarded out-of-hand.

Similarly, when molecules impact on solids a substantial fraction of this translational energy is unavailable for their internal excitation because it is expended in exciting oscillation modes of the lattice or is shared (as noted above) with surface complexes and contaminants. (The dynamics for hypervelocity atoms striking simplified-model--atomically clean, crystalline--materials, which turns out to be a complex issue, was recently reviewed in Ref 74.) Further, air species impinging on solid surfaces with most probable relative translational energy as high as 5 eV (O_2 and NO) or 10 eV (CO_2) above their dissociation threshold--which in absolute terms is about twice this barrier height--have not been found to become broken apart (Ref 75). This energy partitioning casts serious doubt on the validity of invoking such impact dissociation of post-threshold N_2 (Ref 72) as a step in the chemistry of spacecraft glows, as well as on the hypothesis that measurable energy would appear in the $N_2(a)$ exit channel. (Their neglect of energy partitioning in collisions also calls into question earlier interpretations of visible-near UV spacecraft radiation--for example, that purported to be from $OH^\dagger$ (Ref 76)--as due to "relative kinetic energy".)

Nonetheless, since the effective masses of the many possible types of surface complex cannot be quantified, the possibility that the requisite fraction of the high-velocity Maxwellian tail of the N_2 molecules reflects with 8½ to 9½ eV internal excitation can not be dismissed solely on the simple grounds of energy availability (unlike the "biomolecular" collision process discussed in the second paragraph above). The expected distribution in internal energy, however, would not result in the observed nonmonotonically-

and slowly-varying population of upper vibrational states. Heavy-body inelastic cross sections generally increase with [(available energy)-(barrier potential)]$^{-2}$ just above threshold (see Section 6), which would lead to a monotonic, relatively fast decrease of the initial population with increasing v'. The flux of N_2 incident per unit energy interval falls off very rapidly with energy; for example, the ratio of 15 ± 0.1 eV to 14 ± 0.1 eV molecules is 1/200 in the model atmosphere we applied above. Thus the kinetic energy distribution in the center-of-mass system would result in a much lower relative population of v' as high as 4 and 5 than the 1/4 deduced from fitting the orbit-averaged S3-4 spectrum. (The same argument applies to population of $N_2(a)$ by the rapid, 3¼ eV-exoergic atom interchange reaction of N with NO.)

Surface-Catalyzed Exothermic Recombination

The measured spectral distribution in the LBH bands is similar to that from active nitrogen (Lewis-Rayleigh) afterglows, whose origin is homogeneous recombination of ground-state nitrogen atoms (Ref's 77-79). In post-discharge nitrogen gas at low pressures (≤2 Torr) this radiation is excited by inverse predissociation into v' = 6 of $N_2(a)$ through the shallow $^5\Sigma_g^+$ state (refer to Figure 2.1), after which $N_2(a, v')$ is collisionally relaxed by $N_2(X)$; the volume emission rates are proportional to $[N(^4S)]^2$ (Ref's 78, 80). At higher pressures, lower vibrational states (≤3) of $N_2(a)$ are initially populated by (high cross-section) collisions of $N(^4S)$ atoms on $N_2(B^3\Pi_g)$ molecules, at least some of which themselves are formed by kinetically-complex association processes; the volume emission rates vary with $[N(^4S)]^3$ (Ref 78). (The well-known energy-pooling reaction of two $N_2(A)$ molecules (Ref 81) does not produce $N_2(a)$, and furthermore $N(^4S)$ rapidly attacks $N_2(A)$; in consequence a dependence of LBH intensity on $[N]^4$ is not found in the laboratory experiments.) N + N recombination would appear to be the dominant process on spacecraft surfaces because 1) LBH bands with v' = 4 and 5--and in view of the higher-resolution "ISO" spectra and the aforementioned previously-published S3-4

data, v' = 6--are present; and 2) the $N_2(B)$ molecules that are seen in the laboratory are produced in the off-surface gas from a precursor formed on the substrate materials so far investigated (Ref's 63, 82), rather than by direct surface catalysis.

Heterogeneous recombination into the $N_2(a)$ state could of course be proceeding by a "direct" mechanism not involving this crossing of potential curves, as has been postulated for $N + O \rightarrow NO$ (B, with no [detectable] A or C) (Ref 34; see also the discussion of this process in Section 2). Nevertheless, the observation that the highest v' in the artefactual emission corresponds to the first dissociation limit of N_2 in itself supports attribution of this spacecraft glow to Langmuir-Hinshelwood reactions of ground state N atoms thermally accommodated on the desorption surface. Other electronically-excited recombinant species have also been found to desorb from surfaces with lower average vibrational excitation than when they are formed in the gas phase: $SO_2(^3B_1, {}^1B_1)$ (Ref's 83, 84), NO ($B^2\Pi$) (Ref 34), and NO_2 ($^2B_1$, $^2B_2$) (Ref's 64, 85). (Similar results reported for $O_2(A^3\Sigma_u)$ and $N_2(B^3\Pi_g)$ are due to secondary processes involving precursors.) The pseudocontinuum from NO_2^* off low earth-orbiting spacecraft is also distinctly "redder" than from homogeneous laboratory recombination of NO with O (Ref's 1, 7). The laboratory NO_2^* (Ref 64) and SO_2^* spectrum shifts are interpreted as due to partial vibrational relaxation by the surface of these electronically-excited triatomic molecule before they desorb; this may be taken to be the process that results in the high relative population of low v's in the on-orbit emission spectra from $N_2(a)$--a species that is known from laboratory experience to be more rapidly quenched vibrationally than electronically by molecular collisions at temperatures near 300K.

Dependence on Spacecraft and Atmosphere Parameters

The VUV intensities reported in Ref 22 were measured over ~20-min periods starting ~10 min after the near sun-synchronous S3-4 satellite passed near the south geographic pole into the dark

hemisphere. That is, the LBH glow data (such as those in Figure 4.1) were always taken in the same sequence, with the spacecraft moving toward higher air densities over sensibly the same span of latitudes and local times. The apparent very strong dependence of these nadir intensities on the density (or ram flux) of nitrogen atoms noted above could thus be primarily due to one or both of the following spacecraft-associated effects.

1a) Some systematic change in orientation of the recombination surfaces relative to the airflow, or a change in their physical figure, is recurring during these regular data-taking periods.

1b) The temperature of these (unidentified) surfaces is similarly subjected to regular varying change.

Alternatively, the strong variation with [N] could be a real effect of the surface chemistry, describable as follows.

2) The rate limiting step in the chemiluminous reaction involves incident species other than, and not directly the instantaneous rate of arrival of, nitrogen atoms.

A still further explanation has recently been postulated (in Ref 86).

3) Excess $N(^4S)$ is being produced by an atom interchange reaction between reflected N_2 and incident O (or vice versa) in the ram gas, from where some of these nitrogen atoms impinge on the windward surfaces.

We consider here these potential sources of the small intensity scale heights illustrated in Figure 4.1.

Before proceeding, we note that some atmospheric air particles strike inner walls of the grating spectrometer's sunshade (illustrated in Figure 1 of Ref 68) even when this instrument points to the nadir, since the atoms and molecules have a finite velocity in the direction of its optic axis. Specifically, their mean thermal scalar velocity components at 200 km and 900K exosphere temperature are roughly 1/15 the instrument's orbital speed (the less abundant N_2 molecules moving somewhat more slowly). Thus some of the ambient air flows onto a small surface area inside the outer lip of

the open baffle structure, from which desorbed $N_2(a)$ molecules created as discussed above would move directly into the spectrometer's field. Were they to effuse at the surface temperature ($\approx$ 300K) the average radiative mean free path of the mass-28 molecules would be

$$\text{(mean normal effusion velocity)} \times \text{(radiative lifetime)} = (3[\text{Boltzmann constant}]300/28)^{1/2} \times (120\ \mu\text{sec}) \approx 6\ \text{cm}.$$

In practice, as we noted earlier, the exit velocities from some associative desorption can be much higher than surface-thermal (and the angular distribution of the desorbed molecules is commonly more strongly peaked forward than Lambertian); this effect has been amply demonstrated in Ref 16. That is, the exposed surface areas on which $N_2(a)$ is formed can lie a substantial fraction of a meter away from the field of view of the S3-4 or Spacelab 1 instrument.

Discussion

The actual airflow into the sunshade would depend on the vehicle's pitch angle relative to the optic axis. Even more important, if the stated stabilization of the space vehicle about its yaw (vertical) axis refers to other than a fixed direction relative to its horizontal velocity vector, the changing angle to ram of its exposed surfaces within a few 10's cm of the spectrometer's field of view would result in a systematically recurring modulation of the optical signal. Such variations in column intensity due to orbit-related changes in the vehicle's aspect would of course reflect the ambient air densities, and so be consistent with the stated--albeit by no means unequivocal, as discussed above--dependence of column emission rates and scale heights on calculated exosphere temperature. Similarly, other regular but undocumented changes with latitude or altitude in the host vehicle's physical configuration--made in connection with other elements of its mission--could render the reported VUV altitude profiles partially or completely artefactual.

Turning now to effect 1b) above, we note that the temperatures of the spacecraft's previously sunlit recombination areas would tend to decrease by radiative cooling during the data period. An increased temperature can either increase or decrease surface reaction rates at constant external densities of reactants, as the rates of both physi- or chemisorption (which generally decrease) and on-surface desorptive reactions (which generally increase) play a part in the overall process. The rates of production of the precursors of $N_2(B)$ and $O_2(A)$ on laboratory polycrystalline metals are found to increase with decreasing surface temperature in the 400K-300K range (Ref 64); and the rate of reaction of O with NO to electronically-excited NO_2 on shuttle's protective tiles and purposefully exposed engineering materials (Ref 5), as well as to all states of NO_2 on the metal walls of mass spectrometers (Ref 42), is also larger at low surface temperatures. (The fractional coverage of ram surfaces in the low earth orbital environment, where the O-atom fluxes are of the order of 1 monolayer/sec, is expected to be much higher than in the laboratory experiments, where the achievable beam fluxes tend to be lower.)

In contrast the probability of formation of NO_2^* on 300K-325K Cu at low fractional participant coverage has a small positive temperature dependence (Ref 64). Further, and perhaps most apposite to the S3-4 observations, the recombination probabilities of N atoms (to all states) on several metals at higher temperatures show complex, nonmonotonic behavior (Ref 87; these may be associated with changes in structure of the surface or bulk material). Surface temperature changes could also alter the spectral distribution within the LBH system, by changing the rates of accommodation of vibrational energy and of desorption of $N_2(a, v')$. While no differences in the artefactual VUV spectra over the data period are reported in Ref 22, the limited sets of spectral distributions may not have sufficient intensity resolution to address this issue.

If the small intensity scale heights reflect a real surface-chemistry phenomenon in which only ambient N atoms participate (and

are not principally due to effect 1a) above, changes in vehicle aspect or shape), the rate limiting step 2) would be the creation/destruction of recombination-promoting active sites by the approximately 100x higher-flux other thermospheric species. Classical surface-reaction theory (see for example Ref 88) indicates that the order of the dependence of the excitation rate on [N] at high fractional site occupations need not be integral or constant, or even positive. The intensity of the orange-red off-ram surface emission from Atmosphere Explorers (Ref 21), should it--like shuttle glow--be due to NO_2^*, is similarly essentially independent of the density of the lower-concentration participant species NO; that is, it is zero-order in the flux of nitric oxide molecules to spacecraft surfaces. Further, while the excitation rate of this visible glow off Atmosphere Explorer is first-order in [O] above 180 km (Ref 21), it can be interpreted as being about third-order in [O] at lower altitudes.

Among the applicable examples of reaction interference in the laboratory is the quenching of O_2^* emissions when NO is added to the O-atom gas flowing to a Ni surface, as NO_2^* grows in (Ref 85), and--in particular--the enhancement on teflon and strong, hysteresis-suggesting ("conditioned") depression on quartz of the probability of recombination of N atoms in the presence of O_2 molecules (Ref 32). When other species are present in much higher concentrations, varying the density of active sites on the surface, the simple kinetics involving only the recombining species themselves (or itself) does not of course apply. In spaceborne mass spectrometers a qualitatively similar--and temperature-dependent--surface conditioning, which is interpreted as buildup of O (and NO) adsorbate, is found to play a critical part in the reactions of incident N atoms (Ref 43). These changes in the reaction rate are due to creation or occupation of active surface sites, which in the context of catalysis would be known as activation or poisoning.

The regularity of the data-taking sequences on S3-4 is thus consistent with the idea that the commonly-observed, but usually

not completely understood, phenomenon of conditioning of the substrate is playing a part in the high apparent order of the VUV-chemiluminous reaction. Such a surface alteration would depend on the fluences of one or more precursor (for example O) or participant species over some as yet-undefined previous characteristic adsorption/desorption/reaction period. The column intensities would thus only in part reflect the instantaneous fluxes--which have heretofore been considered as controlling the intensity of the artefactual LBH glow.

The nitrogen atom-enhancement mechanism 3) proposed in Ref 86 would proceed as follows. Ambient N_2 (or O) energy-accommodates on ram surfaces and then desorbs into the generally anti-ram direction at effusion velocities, which as we have seen are typically ½ km/sec. Some of the N_2 (or O) then collides with incident O (or N_2) in a volume whose side is comparable in length with the characteristic dimension presented by the spacecraft--that is, in the "snowplow" windward volume. The resulting mean relative kinetic energy available in the center-of-mass system of N_2 and O is 3.8-3.9 eV, which is above the 3.27-eV endothermicity of the atom exchange reaction $N_2 + O \rightarrow NO(X, v = 0) + N(^4S)$. The momentum-transfer dynamics in these reactive collisions is such that the new NO and N particles move toward the spacecraft surface, thus increasing the incident fluxes and (presumably) surface densities of both species.

Ref 86 adopts a reaction cross section extrapolated from laboratory shock tube data that were taken at about 1/10 the relative energy in the above low earth orbit scenario. (Refer to Table 6.10.) This figure leads to a higher flux of nitrogen atoms to S3-4 than comes directly from the ambient atmosphere at altitudes below 220 km, and a scale height and mean LBH-bands intensities that are in qualitative agreement with the spectrometer data. (In addition since the enhancement of N-atom fluxes increases with the characteristic dimension of the ram surface--because the snowplow volume from which atoms may intercept the surface extends farther forward of it--, the VUV radiances from

~33 x 7 m Shuttle Orbiter are predicted to be higher than from ~2 x 2 m S3-4, as appears to have been observed.) However the reliability with which the cross section for the atom exchange reaction at ~6/10 eV above the endothermicity barrier can be extrapolated from the laboratory results at much lower reactant energies is questionable (as we note in Section 6), and furthermore other assumptions in Ref 86 are still unverified. Additionally, this atom interchange process would affect all previous mass-spectrometric measurements from low earth orbiting satellites of the ambient densities of both N and NO, which in fact are by and large consistent with atmosphere models and species-concentration data taken by other means. In consequence the contribution to the LBH glow intensities from energetic N_2 + O reactions in the off-surface ram gas--that is, by creation of new $N(^4S)$ (and NO)--can not at present be reliably assessed.

Concluding Comments

The VUV column emission rates measured from S3-4 are numerically a maximum of about 10^{-4} times the fluxes of $N(^4S)$ atoms incident on surfaces of the spacecraft oriented normal to the airflow, and considerably less at the higher orbital altitudes. As noted, these two quantities are not directly comparable with one another because the excitation/detection geometry is not known. However if the glow volume underfills the nadir-directed field of view of the spectrometer--as would be expected--, the yield of LBH radiation would be higher than this 10^{-4} figure. Nitrogen atom recombination probabilities range between 10^{-5}-10^{-3} on inhibiting laboratory insulators (Ref 32) and 10^{-1}-1 on many metals (Ref 87). Most of the N atoms entering spaceborne neutral mass spectrometers with metal walls combine with O atoms (see for example Ref's 15, 27, and 42), with the fraction that associates with the less abundant other N atoms undetectable against the much higher natural-atmospheric concentrations of N_2 molecules. In view of this competing consumption process and the known low branching into the $N_2(a)$ exit channel in homogeneous 2N recombination (Ref's

77, 80), the surfaces responsible for catalyzing the VUV spacecraft glow are most probably metallic.

As discussed in Section 3, results of a recent laboratory study (Ref 63) were interpreted as showing that on nitrided polycrystalline Co and Ni at room temperature, $N(^4S)$ associates to $N_2(W^3\Delta_u, v' \approx 11)$. The lifetimes in these high-average vibrational energy upper states of $N_2(W)$ are close to that of $N_2(a)$ (near 100 μsec, Table 3.5). Thus if this 2N recombination reaction also takes place on exposed spacecraft materials, and should $N_2(W)$ desorb with the same mean velocity as $N_2(a)$, the resulting short wavelength infrared W→B (Wu-Benesch) and cascade yellow-red B→A (First Positive) bands would be emitted from approximately the same volume of space as the ultraviolet a→X radiation. (Neither longer-wavelength band system has as yet been reliably identified in the optical glows generated by low earth-orbiting spacecraft.)

A similar surface-catalyzed Lyman-Birge-Hopfield bands chemiluminescence has not (to our knowledge) been reported from any of the many laboratory studies of the Lewis-Rayleigh afterglow. This is in all probability because the walls of laboratory reaction chambers are explicitly designed to inhibit recombination and deexcitation, so as not to interfere with the gas-phase reactions being investigated. In addition, since none of the relatively few experiments performed to date on surface recombination of nitrogen atoms have employed photometers or spectrometers sensitive to the VUV, emission of the N_2 LBH system from laboratory surfaces has not been reported. Clearly, the spacecraft results discussed here give considerable scope to laboratory experimentation on heterogeneous reactions of N in the presence of the other principal thermospheric species O, N_2, and O_2.

SECTION 5

VIEW PROJECTIONS FOR MEASURING INTENSITIES OF SPACECRAFT GLOWS

Introduction

We calculate here the scaled volume emission rates and radiances in molecular bands (and atomic lines) excited by recombination into metastable states and other chemiluminous reactions at ram-directed spacecraft surfaces. The purpose of these calculations is to provide a rational basis for maximizing the signal/noise of measurements on contamination glow features through design of points-of-projection and angular fields-of-view of spectroradiometers that can be mounted on the space vehicle itself (for example Shuttle Orbiter) or spatially-separated sensor platforms (such as SPAS), to exposed surfaces of opportunity (such as Orbiter's body and vertical stabilizer) or material structures specially deployed for investigating the phenomenology of these optical radiations (as are currently being planned).

Background

The distance that a glow volume extends to windward is proportional to the lifetime of the upper excited state of the radiating species, which can vary over many orders of magnitude. Specifically, outboard extents may be expected to range from much less than 1 mm (for electric dipole-allowed transitions, with radiative lifetimes $\sim 10^{-7}$ sec, such as some of those in the UV in Section 2) to 100 m (for many vibrational transitions, typically of order 1/10 sec, as discussed in Section 3) to even hundreds of km (for long-lived metastable molecules, such as the aforementioned ~1-hr O_2 $^1\Delta_g$). The ratio of this radiation pathlength to the characteristic dimension of the exposed surface that catalyzes (or may provide a participant for) the chemiluminous reaction is a natural parameter in computing column inten-sities of the resulting emission feature(s), as is

applied below.

Simply stated, the question of maximizing optical signal against noise from the sky and/or instrument and/or signal-statistics reduces to 1) whether to point the sensor normal or parallel to the exposed surface, and 2) how wide an angular field to employ. The product of this solid angle and the clear area of the objective lens is the instrument's etendue (or throughput) that produces irradiance at the detector; that is, this product determines the magnitude of the signal from both vehicle-induced optical glows and unwanted light from the background star and zodiacal field or atmosphere. Practical problems arise in pointing parallel to emitting layers that are thin compared with the diameter of the sensor's entrance aperture, as the photons scattered from astronomical and terrestrial sources by solid surfaces (and in the infrared, their gray-body radiation) would lower signal/noise at most wavelengths if they reach the photodetector.

We have set up the problem for calculation of glow radiances--the quantity measured by narrow-field sensors (including cameras), such as AFGL's Arizona Imager/Spectrometer --in arbitrary view projections. These radiances can be summed across finite instrument angular fields to compute irradiances, the quantity measured when the scene brightness varies across this field. The background noise from randomly-distributed skylight sources would increase with the square root of the field solid angle; however, since individual bright stars are not "statistically" distributed in elevation and azimuth, wide fields tend to damp the noise from these sources. Noise from the detector itself (and amplifier) would in general be independent of the scene. When the dimensions of the spacecraft glow are known and the background brightness distribution is understood, spectroradiometer fields can be "shaped" to maximize the ratio of (irradiance signal)/(fluctuations in this terrestrial and celestial background).

We have in addition made sample calculations of the

radiances that would be measured in the two aforementioned principal view geometries, perpendicular and parallel to outer surfaces--including Orbiter's body itself. Irradiances from projected instrument fields can be readily computed from these radiances, should they be needed. The model results apply in selecting angular fields and physical locations (points of projection) of optical sensors--such as the AI/S--that produce the combination of optical signal/noise and spatial resolution needed to characterize the anticipated spacecraft-induced glows identified in Section 2, 3, and 4.

In practice, to achieve a balance between usefulness and complete generality of the equations some physically-reasonable simplifying assumptions must be applied. For example we have not considered the case of cascade radiations (such as would come from NO (X, v > 1)), or the spatial redistribution or quenching that would result from collisions of excited species with the atmosphere or one another (to which we have called attention in Sections 2 and 3). Each of these assumptions is called out in the development that follows, and all are summarized in the Conclusions.

Definitions

The desorbed metastable molecules or atoms are taken as having the properties represented by the following symbols.

τ = radiative lifetime, assumed to be unique (i.e., the particles have a single upper excited state, with no radiation-producing cascade from the lower state of the initial transition).

v = speed, average value $\bar{v}$.

S = pathlength (distance) traveled from the point on the surface at which the particle was excited.

$S_o \equiv \bar{v}\tau$ = average distance traveled by the particle before it radiates. (S_o is assumed to be much less than the mean free path of the species for elastic or inelastic collision with the atmosphere; that is,

most of the particles radiate before scattering or being de-excited/re-excited by ambient atoms and molecules. As noted previously, at 250 km altitude this collisional mean free path is of the order of 1 km in the fixed atmosphere's reference frame.)

F_o = total hemispheric flux (= $\int[\partial F/\partial\Omega]d\Omega$)--that is, the number of desorptive excitation events per unit time per unit exposed area--, where

$\partial F/\partial\Omega$ = angular distribution of desorbate flux leaving the surface (Ω refers to solid angle and F to photon flux);

$d\Omega$ = solid angle increment $2\pi \sin\Theta\, d\Theta$, where

Θ = angle between the velocity vector and surface normal.

The desorbed species flux is thus implicitly taken as uniform in azimuth.

The <u>excitation surface</u> is described by

a = total area;

X, Y = coordinates in its plane, measured from its center. (The surface is assumed to be flat; calculating volume emission rates off curved surfaces involves a straightforward generalization of the procedure. We consider later the radiances in one simple cylindrical-symmetry geometry, and off Orbiter's body.)

Z = coordinate in the direction of the surface normal, i.e., component of outboard distance perpendicular to the area of spacecraft at which radiative states are populated.

Figure 5.1 illustrates this geometry. Note that

$\cos\Theta = Z/S$.

In the specific source geometries that we consider below

r = radius of a circular excitation area, and

L = length of a side of a square excitation area.

Also

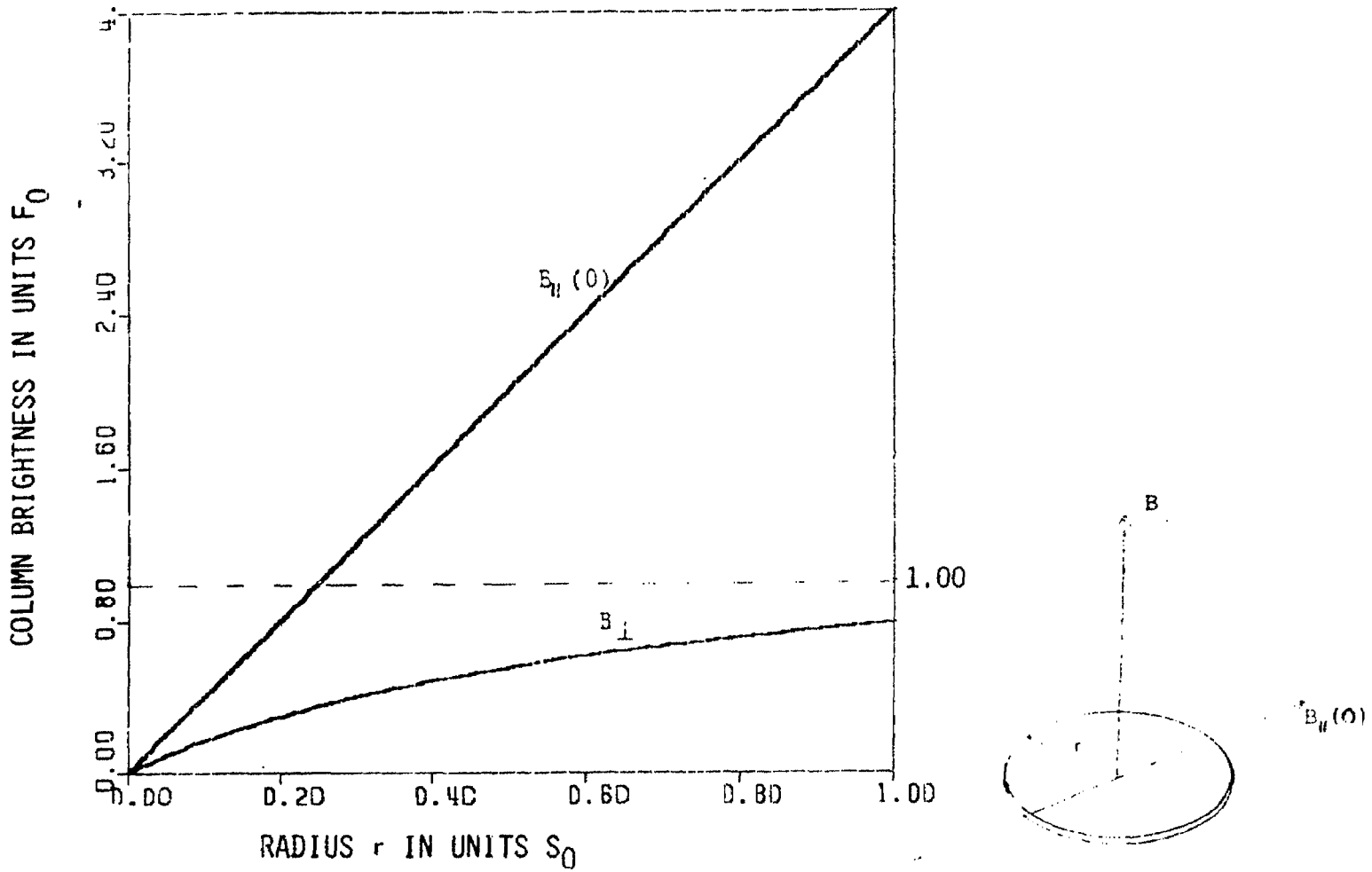

Figure 5.1. Column brightnesses viewing perpendicular from the center of a circular excitation surface ($B_{\perp}$) and parallel to the surface at near-zero tangent intercept distance ($B_{\parallel}(0)$). F_o is the total (Lambertian-distributed) flux of excited species from each surface area element, and S_o is the radiative pathlength of this species. (The area occupied by the aperture of the optical sensor is neglected; see text.)

η = spatial density of emitters at X, Y, Z or S, Ω;

$\dot{\eta}$ = volume emission rate = η/τ.

General Treatment

The number of excited molecules or atoms emitted into $d\Omega$ within speed interval dv from surface area element da is

$$(\partial^2 F/\partial\Omega\partial v)\, d\Omega\, dv\, da.$$

The number of particles per unit path along solid angle element $d\Omega$ from da at S with speed v, neglecting for the moment loss by radiation in the distance traversed S, is

$$v^{-1}(\partial^2 F/\partial\Omega\partial v)\, d\Omega\, dv\, da.$$

The density η of particles at S, $d\Omega$ with speed v is

$$v^{-1}(\partial^2 F/\partial\Omega\partial v)\, d\Omega\, dv\, da/S^2\, d\Omega.$$

Then taking into account the fractional loss of excited desorbate by radiation along pathlength S ($= 1 - \exp[-S/v\tau]$)

$$\eta(S,\Omega) = \int_0^\infty \int_{(area)} (\partial^2 F/\partial\Omega\, dv)\, v^{-1} S^{-2} \exp[-S/v\tau]\, dv\, da.$$

(Henceforth we write $\int_{(area)}$ as $\int_a$.)

We make the further assumption that the velocity distribution of the particles does not depend on their desorption angle Θ, which holds when they are thermally accomodated to the surface (more on this momentarily). We also define a velocity distribution f(v) (the probability of [always-positive] velocity v) such that $\int_0^\infty f(v)\, dv = 1.0$. Then

$$\partial^2 F/\partial\Omega\partial v = f(v)\, \partial F/\partial\Omega.$$

The density of emitters between S and S + dS in solid angle $d\Omega$,

originating from surface area element da, is then

$$\eta(S,\Omega)\ da = (\partial F/\partial\Omega)S^{-2}da\int_0 f(v)v^{-1}\ \exp[-S/v\tau]\ dv.$$

We make the further assumption that the angular distribution of desorbate flux is Lambertian (or Knudsen-like), that is,

$$\partial F/\partial\Omega = \pi^{-1}\ F_o\ \cos\Theta.$$

This behavior is expected when the desorbate is thermally accomodated, and when only a negligible potential barrier against desorption is present--that is, when effusion at the surface temperature describes the desorption process and determines the particle velocity and angular distributions. In some laboratory recombination experiments on smooth metallic crystals, forward peaking and non-Maxwellian velocity distributions are observed (Ref 16), which are interpreted in terms of high-lying subsurface barriers; the extent to which this may occur on the microscopically-rough engineering materials of spacecraft surfaces is not known.

For computational simplicity and tractability we next replace the actual distribution of velocities of the desorbed particles with a single velocity $\bar{v}$, so that $f(v) = \delta(v-\bar{v})$. $\bar{v}$, which when the distribution is Maxwellian is 171 $[T/M]^{1/2}$ m/sec (the magnitude of the spread of Maxwellian velocities is also of the order of $\bar{v}$), can be taken as the mean departure speed of translationally-accommodated molecules or atoms having molecular weight M from a surface at temperature T. Again, in the near-surface reaction circumstances discussed in Ref 16 the mean velocity could be considerably higher than predicted from the purely thermodynamic, classical "surface"-accommodation arguments commonly applied.

Since $S_o = \bar{v}\tau$,

$$\eta\ da = (\pi\ \bar{v}\ S^2)^{-1}\ F_o\ \cos\Theta\ \exp[-S/S_o]\ da,$$

and the volume emission rate $\dot{\eta}$ ($= \eta/\tau$) becomes

$$\dot{\eta}(S,\Theta)\ da = (\pi S_o S^2)^{-1}\ F_o \cos\Theta \exp[-S/S_o]\ da.$$

For finite flat surfaces of area a this can be expressed as

$$\dot{\eta}\ (X,Y,Z) = (\pi S_o)^{-1}\ F_o \int_a S^{-2} \cos\Theta \exp[-S/S_o]\ da$$

$$= (\pi S_o)^{-1}\ F_o\ Z \int_a S^{-3} \exp[-S/S_o]\ da.$$

If we take $da = dX_o\ dY_o$ in the plane of the surface, then the desorbate pathlength S is given by

$$S^2 = (X-X_o)^2 + (Y-Y_o)^2 + Z^2.$$

Volume emission rates at X, Y, Z or S, Θ are calculated by evaluating the above integral over the [flat] source area. Column brightnesses of the glow volume can be calculated from these volume emission rates by summing all the $\dot{\eta}$'s along the optical sensor's sight path (as in aurora/airglow computations). This last step applies the further assumption that this volume of space is optically thin to its own radiation, which would indeed be valid for the recombination glows that we have considered in Sections 2-4 (with the possible example of the resonance lines of H and O atoms mentioned in Section 2).

Solutions for Conditions of Direct Interest

The two view projections of most immediate practical interest are (as noted)

-- perpendicular to excitation surfaces, that is, directly into ram: column brightness $B_\perp$;

-- parallel to surfaces at tangent distance Z, intercepting the normal at the center of the circular or square excitation area: column brightness $B_\parallel$.

The latter projection will be recognized as that anticipated for

forthcoming infrared measurements from space shuttle, off a specially-deployed flat plate by a variable-wavelength filter radiometer (whose angular field is not finally specified).

We have evaluated the integrals-over-excitation-area (which as can be seen in general to involve exponential integral forms) by a combination of analytical and numerical methods. We present first the results for $B_\perp$, neglecting for the moment the finite fraction of the recombination surface area occupied by the entrance aperture of the optical sensor itself.

Figure 5.1 shows the perpendicular brightness $B_\perp$ viewed from the center of a circular plate in units of total hemispherical desorbate flux F_o as a function of the plate's radius r in units of mean radiative pathlength S_o. When $r \gg 1$ (physical radius large compared to pathlength, as for the ~10-cm yellow-red glow from Shuttle Orbiter's surfaces), the axial-perpendicular column brightness approaches F_o. This result--that the column intensity viewing outward is equal to the surface excitation rate--is just that expected. At the other extreme, when $r \ll 1$ --long radiative pathlength, as for the 0.16 sec-lifetime O_2 Herzberg I bands--, the perpendicular brightness asymptotically approaches $2r \times F_o$. For example from a 1 m radius surface this blue-UV O_2 radiation, whose pathlength is ~80 m ($= \tau \bar{v}$ = 0.16 sec x 500 m/sec), would exhibit a perpendicular column brightness of 2 (1/80) x (rate per unit surface area at which the O_2 $A^1\Sigma_g^+$ upper state is being excited); refer again to the developmentof a "nominal" absolute brightness in this feature in Section 2.

Analogous $B_\parallel$ results for square excitation plates with three scaled side dimensions L are shown in Figure 5.2. When $L = 1 \cdot S_o$, $B_\parallel \approx 0.6 \cdot F_o \cdot 1 = 0.6\ F_o$. This radiance (as expected) is very close to that in Figure 5.1 produced by a circular disk of scaled radius ½ S_o (that is, diameter $1 \cdot S_o$). When $L = (1/5) S_o$, $B_\parallel$ falls to approximately (0.9) 1/5 F_o = (0.18) F_o; that is, when the square's side L is as small as 20% of the radiative pathlength S_o, the perpendicular column brightness is

only slightly less than 20% of the hemispherical desorbate flux. Then as $L/S_o \to 0$, $B_\perp \to (L/S_o) \cdot F_o$; that is, $B_\perp$ becomes proportional to $1/S_o$ in the limit of very large radiative pathlength (as was the case above for small r). (The in part-unexpected result that $B_\perp$ depends on only the <u>first</u> power of S_o is due to the fact that when $S_o \gg L$ the integral of density of excited desorbate over an outward-directed view column depends principally on the $(1/S^2)$ divergence of the desorbate flux, rather than on the exponential radiative decay.)

The <u>parallel</u> brightness $B_\parallel$ as $Z \to 0$ can be seen in Figure 5.1 to become equal to $4r\ F_o$ (r is in units of S_o). This result comes about because the small falloff outward of volume emission rate can be neglected when the excitation surface from which desorption takes place is large compared with Z. In evaluating the column integral $\dot{\eta}$ then becomes $2F_o/S_o$, and the brightness is $\dot{\eta} \cdot 2rS_o = 4F_o\ r$, or $4\ F_o \cdot$ ([physical radius of the excitation surface]/ [pathlength]). This apparent gain in glow radiance can of course only be realized at intercept distances considerably smaller than S_o, that is, well within a radiative pathlength. Note that the absolute brightness in this parallel projection is inversely proportional to S_o, just as in perpendicular projections.

Figure 5.2 shows $B_\parallel$ as a function of intercept distance Z (with a comparison to $B_\perp$) for the ratios $L/S_o = 1$ and $L/S_o = 1/5$. Results for the limiting case $L/S_o \to 0$ lie close to those for 1/5. When radiative pathlength $S_o \gg L$ the brightnesses may be presented in closed form:

$$B_\parallel\ (Z) = (4\ F_o L/\pi S_o)\ \arctan\ (L/2Z),$$
$$B_\perp\ (Z) = (4\ F_o L/\pi S_o)\ \ln\ (1 + \sqrt{2}).$$

The parallel column brightness can be seen to approach $2F_oL/S_o$ when the sight path grazes the excitation surface, in agreement with the result from a circular area. If $S_o \doteq L$, $B_\parallel$ is greater than $B_\perp$ when $Z \leq 0.4\ L$, and then decreases rapidly at greater

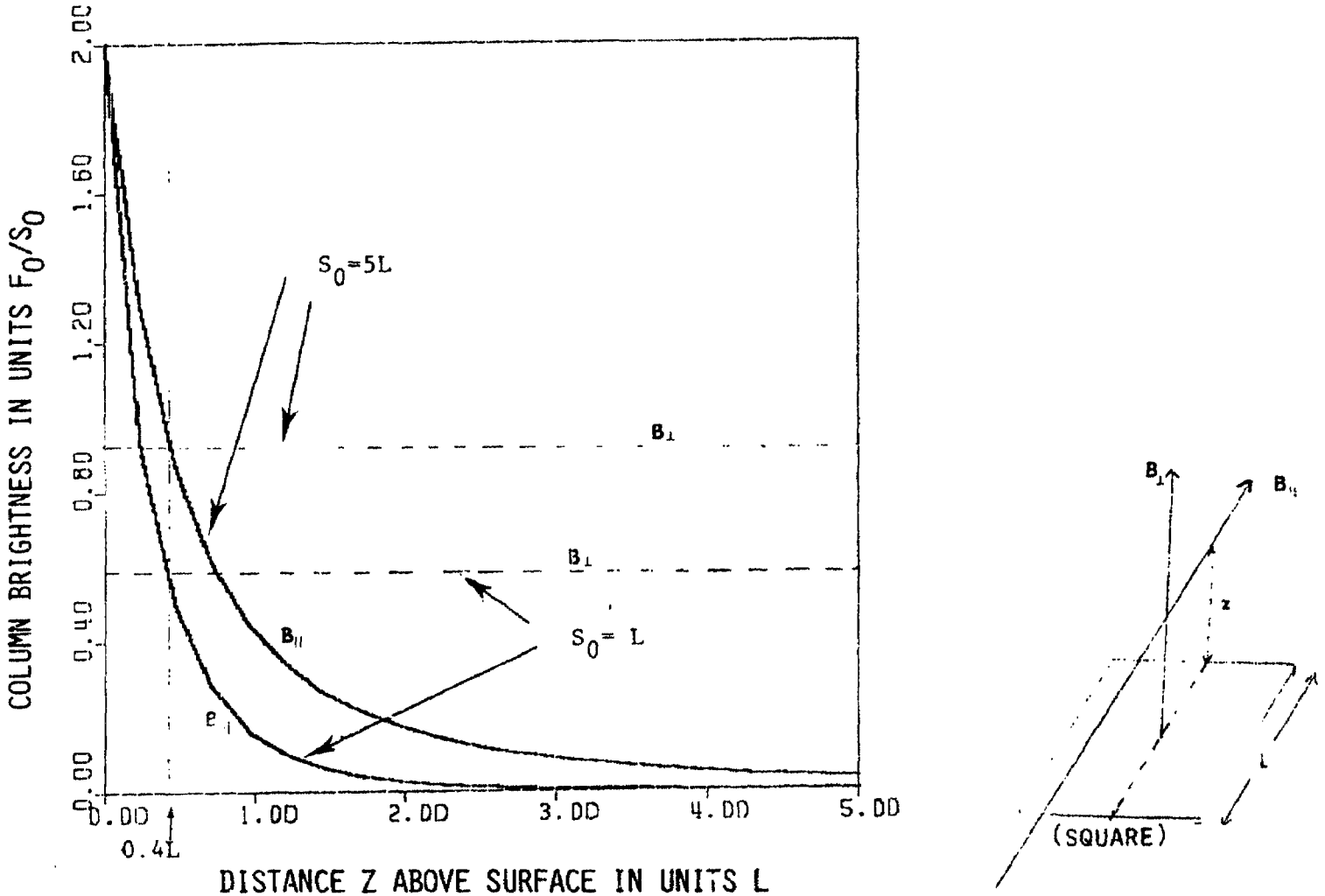

Figure 5.2. Column brightnesses viewing perpendicular from the center of a square excitation surface ($B_\perp$) and parallel to the centerline of the surface ($B_\parallel$) at tangent intercept distance Z in units of the square side dimension L, parameterized for L/S_O = 1 and 1/5. The units of column brightness are flux times L/S_O. Parallel projections intercepting at $Z/L \leq 0.4$ can be seen to provide higher radiance signal than the corresponding perpendicular projection

tangent-intercept distances. That is, when the tangent distance of the narrow sensor field-of-view is less than 0.4 times the side dimension L of the surface generating the glow, the parallel radiance is greater than the perpendicular radiance: by up to a factor of 3 when $S_o/L = 1$, falling to a factor of 2 as $S_o/L \rightarrow \infty$.

The intercept distance Z at which $B_\parallel$ becomes equal to $B_\perp$ is determined almost entirely by geometry and desorbate divergence when $S_o \geq L$, and hence is on the order of the surface dimension and (to a good approximation) independent of S_o. When $S_o < L$ the glow is confined to a region near the surface, and the tangent distance at which $B_\parallel = B_\perp$ of course becomes smaller.

Radiance of Glows from Orbiter's Body

The cross-sectional shape of Shuttle Orbiter's fuselage is essentially a somewhat rounded rectangle (more so than a cylinder). To within the accuracy of the calculation model here, for emission features whose radiative pathlength S_o is greater than the length (~33 m) or width (~7 m) of this body $B_\parallel$ viewing from a spatially-separated platform (such as SPAS) can be estimated from Figure 5.2. L would be taken as $(33 \cdot 7)^{1/2}$ m viewing parallel to Orbiter's long axis, and 7 m viewing across its fuselage. This approximation obviously neglects the not-insubstantial contribution from Orbiter's wing surfaces, which could be added in when the vehicle's orientation to its trajectory vector places these large flat areas facing to windward.

Calculation of volume emission rates becomes rather more complex for viewing into ram from the open payload bay, as the various materials exposed present a mix of (largely-unknown) catalytic-excitation probabilities. Calculation of $B_\perp$ in this geometry would involve breaking up the surface into local areas of estimated excitation efficiencies, computing $\dot{\eta}$'s from each of these areas, and then summing these volume emission rates along the optical sensor's sight path.

Effect of the Finite Area of the Sensor Aperture

$B_\perp$ in the examples above refers to a measurement geometry in which the sensor's entrance aperture is at the geometric center of the (idealized) excitation surface. If S_o is less than the sensor aperture's radius r_A, this exclusion of part of the source of radiation has a significant effect on the measured brightnesses [if the flux of metastable desorbate particles from the exposed sensor material is different from that from the surrounding excitation-surface material].

Consider again a circular surface, with no desorbate molecules emanating from this centrally-positioned aperture itself. The perpendicular column brightness can be readily shown to be $B_\perp(r) - B_\perp(r_A)$, where the $B_\perp$'s are as given by Figure 5.1. As an example, when r = 1 m, and r_A = 1 cm and S_o = 10 cm (such as for the NO_2^* spacecraft glow), the occlusion from the central sensor area results in a 17% reduction from the result $B_\perp = F_o$ calculated above. When S_o is as small as 1 mm (as for the NO β bands) the reduction factor in this geometry is of the order of 10^{-5}; this outcome would be expected, as virtually all of the desorbate molecules radiate before they move far enough to enter the sensor's (ideally-sharp) field of view. Thus for emission features with $S_o \leq 1$ cm viewed in perpendicular projections, most of the radiation measured is being excited at exposed surfaces of the sensor itself.

Practical Considerations

When the radiative pathlength of a glow feature is short compared with the characteristic dimension of the surface at which it has been excited--an example is the NO_2^* visible pseudocontinuum relative to Orbiter's vertical stabilizer--, the intuitive conclusion that radiance signal/noise is improved by viewing nearly parallel to long surfaces is valid. But as S_o becomes smaller (as noted above) difficulties arise in achieving sufficient instrument throughput to realize significant gain

along parallel sight paths--particularly since the solid surface must for almost all wavelengths of interest be excluded from the effective field to avoid albedo contamination of the induced measurements of spacecraft-glow. (For example the ~1 mm-thick glow of the NO β bands that result from N + O recombination on surfaces would require a long flat lens to be sensed in parallel projections.)

The physical situation is qualitatively different for those emissions whose pathlength exceeds the realistically achievable dimensions of excitation surfaces (a few m). These include virtually all infrared vibrational bands, and also radiations from species in metastable electronic states with lifetimes greater than about 5 msec (see Ref 1). As shown above, pointing within less than 0.4 L of the excitation surface provides an improvement in radiance of a factor up to perhaps 3 over that viewing directly into ram (Figure 5.2); this radiance again increases linearly with the length dimension L. However the achievable irradiance--the signal at the detector of optical systems viewing over a finite solid angle--might be larger in simple perpendicular projections, depending on S_o/L (as further discussed immediately below). Furthermore, the experiment problem of baffling the instrument against stray light from surfaces lying close to its field of view is obviously much less troublesome when the axis of this field is to be pointed outward.

In practice, the irradiance viewing perpendicular to the surface would increase almost linearly with the solid angle subtended by the radiometer's field of view up to about 30^o half-angle, for all S_o. This comes about because the radiance viewing outward at angle Θ from the normal falls off only with $\sim\cos\Theta$ [for the Lambertian-distributed desorbate flux that we have assumed]. That is, the total perpendicular near-axial irradiances measured would be $B \cdot \pi (\text{half-angle of the sensor})^2$. The wide-field irradiances in parallel projections in which the radiance varies with Z, and/or in instrument projections with

the optic axis at arbitrary angles to the excitation surface(s), can be calculated starting from the equation for volume emission rate given above.

Summary, Conclusions

The results on relative glow brightness given here were derived with the following simplifying, physically-plausible assumptions:

-- unique radiative lifetime τ (single upper state, no cascade)
-- single desorption velocity $\bar{v}$ (the natural velocity spread is neglected), independent of Θ
-- Lambertian ($\cos \Theta$) angular distribution of desorbate flux (i.e., thermal accomodation to the [rough] surface), with no dependence on azimuth angle
-- optically thin glow volume (and air path to the sensor) to the radiation emitted
-- negligible probability of direction-changing or quenching/repopulating collisions of desorbates with the atmosphere or one another and
-- parallel viewing through a line extending from the center of, or perpendicular viewing from the center of, flat circular or square excitation areas as in Figures 5.1 and 5.2 (with no species that had been excited at other space vehicle surfaces radiating within the sensor field).

The first of these restrictions simply limits the treatment here to desorbates having a single radiative lifetime. The effect of the second is expected to be small, although as noted $\bar{v}$ could be higher than surface-thermal (i.e., "effusive"). The third condition is violated on some flat crystalline surfaces (Ref 16), from which $\bar{v}$ is greater than would be predicted from a Maxwellian distribution at the surface temperature. (That is, the angular and velocity distributions of the desorbing particles are found to be coupled.) However, the amorphous,

rough engineering surfaces of spacecraft tend to make desorbed fluxes Lambertian. The predicted recombination-glow features would indeed be optically thin (fourth condition); and those excited species with radiative pathlength so long that they collide before radiating would in most cases produce brightnesses much lower than those of the sky or atmosphere (a possible exception is $O_2(b)$, as described in Section 3), and thus would not result in detectable signal/noise in achievable sensor integration times.

Excited species from other spacecraft areas exposed to ramming air could drift into the fields of optical instruments designed to view glow off specially-deployed surfaces, whether these fields are oriented parallel or perpendicular to these surfaces. For example, infrared photons from NO_2 ($\nu_1\nu_2\nu_3$) and NO ($v > 0$), which are emitted over pathlengths ~1-100 m (Section 3), would be expected to arise from molecules excited at areas distributed over the spacecraft; each of these surfaces has a potentially different angle to the airstream and efficiency with which its material catalyzes excitation of these vibrational bands.

The fluxes of such experiment-degrading radiating species into the sensor's field could be reduced by fashioning the specially-deployed recombination area into a "shielding" half-cylinder of length comparable with that of the spacecraft and with its open end directed into windward, and pointing the field of the sensor along its central (long) axis. The radiance signal from the area would at the same time be slightly improved by the natural focusing of the desorbate particles: if S_o is greater than three times the radius of the half-cylinder, this novel geometry results in a radiance increase of about 30% over that of a flat plate of the same length and with width equal to the cylinder diameter (that is, with the same projected area to ram).

In planning remote sensing of glows induced by low earth orbiting spacecraft, a distinction must be made between emission

features with expected radiative pathlength S_o greater than and less than the excitation surface's characteristic length dimension L (or 2r). When $S_o < L$, for all emission bands and lines to which the sensor responds, parallel views produce higher radiances--that is, larger photocurrents in optical instruments with instantaneous transverse-field-of-view-at-the-glow $<< S_o$. These include imaging systems such as the cameras that photographed NO_2^* radiation off Orbiter's tail, and the Arizona Imager/Spectrometer. When $S_o > L$, B_η varies with L/S_o; that is, it is inversely proportional to the radiative path and (as expected) linearly proportional to the view pathlength. Thus relative band intensities in emission spectra would be inversely proportional to the relative lifetimes of the upper radiating states; where the probabilities of excitation at the surface are equal, the longer-lived species produce weaker optical signals.

When S_o is greater than L, parallel projections at tangent intercept distances ≤ 0.4 L provide a small (factor-2 or -3) improvement in glow radiance over direct (perpendicular) projections into ram. Some further improvement may result because no part of the excitation area is blocked by the aperture of the optical sensor. Increasing the sensor's etendue to improve the irradiance--the source of signal amplitude in instruments with finite angular fields--appears practical when $S_o >> L$, provided that light scattered off outer surfaces is kept out of the optical field. In the intermediate case that S_o is only a few times L, more detailed irradiance calculations--starting with the equation for volume emission rate η presented here--can be applied to optimize the design of glow-sensor fields.

Whether widening the sensor's field of view improves signal over noise from the earth's atmosphere or celestial sources depends, of course, on its view projection. In general wide fields dampen the effect of individual bright stars, but could bring atmospheric airglow or zodiacal light into the background.

SECTION 6

RADIATION FROM SPECIES EXCITED BY COLLISIONS OF SHUTTLE ENGINE EXHAUST PRODUCTS WITH THE ATMOSPHERE

Introduction

We review here the information available about ultraviolet and visible chemiluminescence from reactions between the major components of space shuttle's control rockets' exhaust and the principal atmospheric species present at its orbital altitudes. The reactions addressed become exothermic as some of the ~1-10 eV relative kinetic energy of the colliding participants goes into overcoming potential barriers. We consider only atom-exchange processes, as non-adiabatic (T→E) collisions appear to be about two orders of magnitude less probable (as further discussed below); vibrational excitation [only], which produces principally infrared photons, is not explicitly reviewed. We also briefly discuss elastic scattering, since 1) in practice a single large-angle deflection event lowers the kinetic energy of the exhaust particle to near or below the thresholds of most reactions that can result in population of an electronic product state, and 2) its physics provides some insight into these more complex inelastic-scattering processes.

The purpose of this technical review is to identify those electronic transitions most likely to produce UV and visible radiations useful in remote passive surveillance of powered missiles traversing the thermosphere. The survey is therefore restricted to the principal perceived reactions of the most abundant combustion species that result in products in short-lived upper states (refer to Figure 6.1); the principles outlined of course also apply to exhaust reactions that are not directly addressed here, and to similar reactions of spacecraft contaminant-outgas species. Insufficient information is available for reliable estimation of state-specific collision

cross sections: the review serves principally to isolate the most probable UV-visible emission features.

The spatial and spectral distributions of radiance of the exhaust plume-interaction volumes are at present modeled by DoD computer codes (such as CHARM, Ref 89), which apply particle transport calculations with partial excitation cross sections of the type reviewed here to generate predictive "scenes" for use in designing optical surveillance systems. The results of this study also apply in planning measurements of the actual ultraviolet and visible signatures of the exhaust plumes from space shuttle's control engines. (These are scheduled to be made in 1990 with Air Force Geophysics Laboratory's specially-designed 0.12 to 1.1 μm-sensitive [Arizona] Imager/Spectrograph.)

Exhaust and Target Species

At shuttle's orbital altitudes (~225-350 km), where the kinetic temperature is very close to the typically-1000K neutral exospheric temperature, the average scalar velocities of the atmosphere's oxygen atoms and nitrogen molecules in the direction of the spacecraft's translational motion are 0.5_6 and 0.4_2 km/sec respectively. The mean free paths at the typical ambient density of $10^9/cm^3$ and effective collision diameter of 3 Å (more on this latter point in the subsection below on elastic scattering), would be about 3 km. In the ram direction these mean free paths of exhaust (or desorbed) particles are reduced by a factor (spacecraft velocity)/(mean air particle |velocity|), which in view of the typically 7½ km/sec orbital speed is about 10. (This issue is discussed in Ref 90.) If the density of exhaust gas exceeds the ambient air density, these simple (free-molecular-flow) arguments of course do not hold; but for the purpose of assessing the cross sections for excitative reactions it is sufficient to consider the collisions as occurring independently and between two bodies--: energetic exhaust molecule and ambient thermospheric O atom or N_2 molecule.

The total ion densities at orbital altitudes, which vary between about 10^5 (night) and $10^6/cm^3$ (day), are a factor 10^3-10^4 lower than the neutral densities. Furthermore, the rocket exhaust-composition models predict relative ionizations of only about 10^{-8} in the exhaust gas. Since the cross sections for ion-neutral reactions are in general not as much as 10^3 higher than the neutral-neutral cross sections at the typically 10 km/sec relative velocities (more on this point also below), we consider only reactions of neutral species. We also neglect collisions on the atmosphere's O_2 molecules because their concentrations are less than one-tenth those of N_2 or O, and on the even less abundant other species O^1D and N^2D and ^4S, H, N_2 (v>0), NO,... present at orbital altitudes.

Shuttle Orbiter has 38 main thrusters and a vernier system of six rockets. All of these use monomethylhydrazine (MMH, $N_2H_3CH_3$) fuel and N_2O_4 oxidizer (Ref 91), as do many DoD vehicle propulsion-and-control systems. Relative concentrations of the thruster exhaust species have been calculated using the model program CONTAM III (Ref's 92, 93), which assumes thermodynamic equilibrium in the exhaust plume (and does not take into account chemical reactions which might take place outside the exhaust nozzle). The calculations of Ref 92 predict a uniform exhaust gas velocity of 3.5 km/sec, based upon a kinetic temperature of 3000K.

Table 6.1 lists the relative compositions of neutral species in the exhaust gas predicted by Ref's 92 and 93. (The much smaller expected mole fractions of ions--such as NO^+--are expressly omitted.) The table also includes the species identified in the experiments reported in Ref 94, in which the exhaust from a 10 newton MMH/N_2O_4 rocket engine operated in a large evacuable test chamber was mass-spectroscopically analyzed; this model engine has ~1/10 as much thrust as the smaller (vernier) shuttle engine. If the reaction between a stoichiometric mixture of MMH and N_2O_4 were complete, the only combustion products would be N_2, H_2O, and CO_2:

Table 6.1. Predicted and observed shuttle engine control rocket exhaust species

Species	Molecular Weight	Predicted Mole Fraction		Observed[†]
		*	**	
H_2O	18	0.328	0.337	Yes(High)
N_2	28	0.306	0.314	Yes(High)
H_2	2	0.17	0.151	?
CO	28	0.134	0.126	Yes
CO_2	44	0.036	0.041	Yes(High)
H	1	0.015	0.029	?
$MMH-NO_3$	108	0.002	-----	Yes
O_2	32	0.0004	0.0009	?
OH	17	-----	0.0009	?
O	16	-----	0.0006	?
NO	30	-----	0.0019	Yes
N_2H_2	30	-----	-----	Yes
NO_2	46	-----	-----	Yes
MMH	46	-----	-----	Yes
CH_2	14	-----	-----	Yes
CN_2H	41	-----	-----	Yes

*from Ref 92 **from Ref 93 †from Ref 94

$$4\ N_2H_3CH_3 + 5\ N_2O_4 \rightarrow 9\ N_2 + 12\ H_2O + 4\ CO_2,$$

in ratios invariant with angle from the exhaust nozzle axis.

In practice little experimental information exists to verify these predicted concentrations of species within the exhaust plumes of operational rocket engines. In one measurement with a mass spectrometer located within shuttle's payload bay and thus well away from the primary exhaust volumes (Ref 95), the mass-28 and mass-30 peaks were found to be enhanced when the vernier engines were operated. This mass-28 signal could be either N_2 or CO, both of which are predicted to be present at high concentrations in the exhaust. The mass-30 peak was attributed to NO, which the model indicates to be a very minor exhaust component. These shuttle data suggest that the NO concentration is approximately as high as one-half that of N_2 + CO, which species are predicted to constitute 44% of the total exhaust gas (see Table 6.1).

In other reports (Ref's 93, 94) the relative concentration of nitric oxide is unusual in that its angular distribution extends much further from the plume axis than that of the other exhaust gases; in addition the $[NO]/[N_2]$ and $[H_2O]/[N_2]$ ratios rise during the engine operation cycle, with [NO] varying from 1/3 to 3 $[N_2]$ (in approximate agreement with Ref 95). These observations strongly suggest that NO is associated with non-equilibrium conditions in the plume. More recently, mass spectrometry of species collected on a cold copper plate exposed to the plume of the 10 newton-thrust (i.e., small) engine in a vacuum test chamber identified not only NO but also several other unexpected molecules: N_2H_2, NO_2, CH_2, and CN_2H (Ref 94). However, the gas-phase densities of these species are not easily estimated from these laboratory data; and the analysis is further complicated by the fact that the masses of some primary ions from neutral pairs, such as N_2/CO, N_2H_2/NO, and MMH/NO_2, were not experimentally resolvable.

In addition, unburned fuel and oxidizer may be exhausted into the atmosphere. The laboratory study of Ref 93 estimated the concentrations of such products during various engine operating periods; the results indicate that in steady-state operation, the fuel expelled as droplets reaches 1¼% of the total (which is in agreement with the prediction by CONTAM III). Most of the droplets are confined to within ±15° of the exhaust plume axis, with the larger ones having narrower angular distributions. It appears (Ref 94) that they consist mainly of MMH-NO_3 dissolved in water, which in the laboratory experiments evaporates leaving brown-yellow crystals of MMH-NO_3 (which sublimes at higher temperatures). At 3000K N_2O_4 is virtually totally dissociated into NO_2 under equilibrium conditions, and at this high temperature NO_2 can in turn decompose into NO. However, since the mass spectrometer data of Ref 95 show very little mass 46 (NO_2; this species also appears at mass 30), the NO in the plume presumably results more from incomplete combustion of MMH to N_2 than directly from decomposition of some of the unused oxidizer. In any case, sufficient evidence exists for the presence of NO to justify its inclusion among the potentially chemiluminescence-producing exhaust molecules.

Energy Considerations

The kinetic energy E available for the reaction between an ambient species of mass m_A and an exhaust species of mass m_B is

$$E = \tfrac{1}{2} \mu \, |\vec{v}_A - \vec{v}_B|^2$$

where $\mu = m_A m_B/(m_A+m_B)$ is the reduced mass and $\vec{v}_A$ and $\vec{v}_B$ are the particle velocities in the rest frame. Shuttle Orbiter's speed in low earth orbit is near 7.3 km/sec, and as noted earlier the approximate directed velocity of the exhaust gas stream with respect to the vehicle is 3.5 km/sec. Thus the maximum and minimum mean velocities of the exhaust gas relative to stationary atmospheric molecules or atoms would be 10.8 and 3.8

km/sec, the instantaneous value depending on the angle between the engine axis and shuttle's trajectory vector.

In addition these velocities have a standard deviation due to the aforementioned thermal (Maxwell-Boltzmann distributed) translational motion of the ~1000K atmosphere and ~3000K exhaust gas. For the light exhaust species H_2O on the atmosphere's O atoms, for example, this standard deviation turns out to be as much as 1.2 km/sec. However in view of 1) the uncertainty in the actual directed velocity and (to a lesser extent) kinetic temperature of the rocket exhaust gas; 2) the fact that only about 1/6 of the collisions take place at relative velocities more than one standard deviation above the mean; and 3) the about factor-two lower standard deviation for heavier collision partners (such as CO on N_2), a more apposite "limit" to the relative velocities would be 0.6 km/sec above and below the above-mentioned maximum and minimum $|\vec{v}_A - \vec{v}_B|$. (The neutral atmospheric wind speed, typically 0.05-0.15 km/sec in a seasonally-and diurnally-variable direction, is small enough to be neglected.) We therefore adopt the relative velocity range 11.4 km/sec to 3.2 km/sec for this review of electronically excitative reactions. Tables 6.2 and 6.3 list E for collisions of the exhaust species in Table 6.1 on oxygen atoms and nitrogen molecules, at these limiting velocities.

These energy extremes are of course "soft", in that the tails of the Maxwell-Boltzmann velocity distribution (and highly abnormal thermospheric wind conditions that can result from geomagnetic storms) will result in some collisions with up to a few eV more energy. This point will become more clear in our discussion below of the behavior of the reactive scattering cross sections near the reaction barrier threshold. Electronic and in particular vibrational excitation of the nominally-3000K (~¼ eV) exhaust molecules could also enhance the reaction cross sections, insofar as the "intermediate" chemical species that can be formed depends on the initial atomic/molecular configurations, for instance; as is briefly discussed later,

Table 6.2. Available relative kinetic energy E calculated for O in collisions with exhaust species

Species	μ, amu	E_{max}, eV	E_{min}, eV
H_2O	8.47	5.74	0.45
N_2	10.2	6.91	0.55
H_2	1.78	1.20	0.092
CO	10.2	6.91	0.55
CO_2	11.7	7.92	0.62
H	0.941	0.64	0.050
$MMH-NO_3$	14.0	9.48	0.74
O_2	10.7	7.25	0.57
OH	8.27	5.60	0.44
O	8.00	5.42	0.43
NO	10.4	7.04	0.55
N_2H_2	10.4	7.04	0.55
NO_2	11.9	8.06	0.63
MMH	11.9	8.06	0.63
CH_2	7.47	5.07	0.28
CN_2H	11.5	7.79	0.61

Table 6.3. Available relative kinetic energy E calculated for N_2 in collisions with exhaust species

Species	μ, amu	E_{max}, eV	E_{min}, eV
H_2O	11.0	7.45	0.59
N_2	14.0	9.48	0.74
H_2	1.87	1.27	0.099
CO	14.0	9.48	0.74
CO_2	17.1	11.6	0.91
H	0.966	0.66	0.052
$MMH-NO_3$	22.3	15.2	1.19
O_2	14.9	10.1	0.79
OH	7.68	5.20	0.41
O	7.47	5.06	0.40
NO	14.5	9.82	0.77
N_2H_2	14.5	9.82	0.77
NO_2	17.4	11.8	0.93
MMH	17.4	11.8	0.93
CH_2	9.33	6.33	0.35
CN_2H	16.6	11.3	0.89

vibrational energy is well known to be more effective than translational energy in overcoming the potential barriers of many chemical reactions. However in view of the uncertain initial excited state populations in the exhaust gas--which would not in general be accurately characterized by a Boltzmann distribution, much less one at the nominally-3000K kinetic temperature--, and the small body of information about reactions of vibrationally-excited species at ~5 eV translational energy, we have considered reactions involving only exhaust species in ground electronic and vibrational states.

Excitative Reactions Considered

This and some further limitations to the reaction set reviewed are summarized in the flow chart of Figure 6.1. We present at this point an introductory overview of why we applied these restrictions, whose physical basis we justify in further detail near the end of this Section.

First, we consider only those exhaust species that CONTAM III and related rocket engine chemistry-flow models indicate are present in mole concentrations greater than 1% of the total (see Table 6.1), plus the nitric oxide that the above arguments strongly indicate to be "frozen in". Less abundant species would obviously produce less intense optical emissions, were their reaction cross sections comparable. The chemical principles outlined here can of course be applied later to these other molecular exhaust products (and unburned fuel/oxidizer, and outgas species), should this be indicated.

Second, we assume the molecules of the exhaust gas are all in their lowest electronic and vibrational states [as noted directly above], and react only with ground-state oxygen atoms and nitrogen molecules. This simplification omits consideration of the internal energies of both the exhaust products and the two target species, and of collisions with the aforementioned less abundant ambient atoms and molecules. Only two body-two (or three-) body (momentum-conserving) reactions would proceed

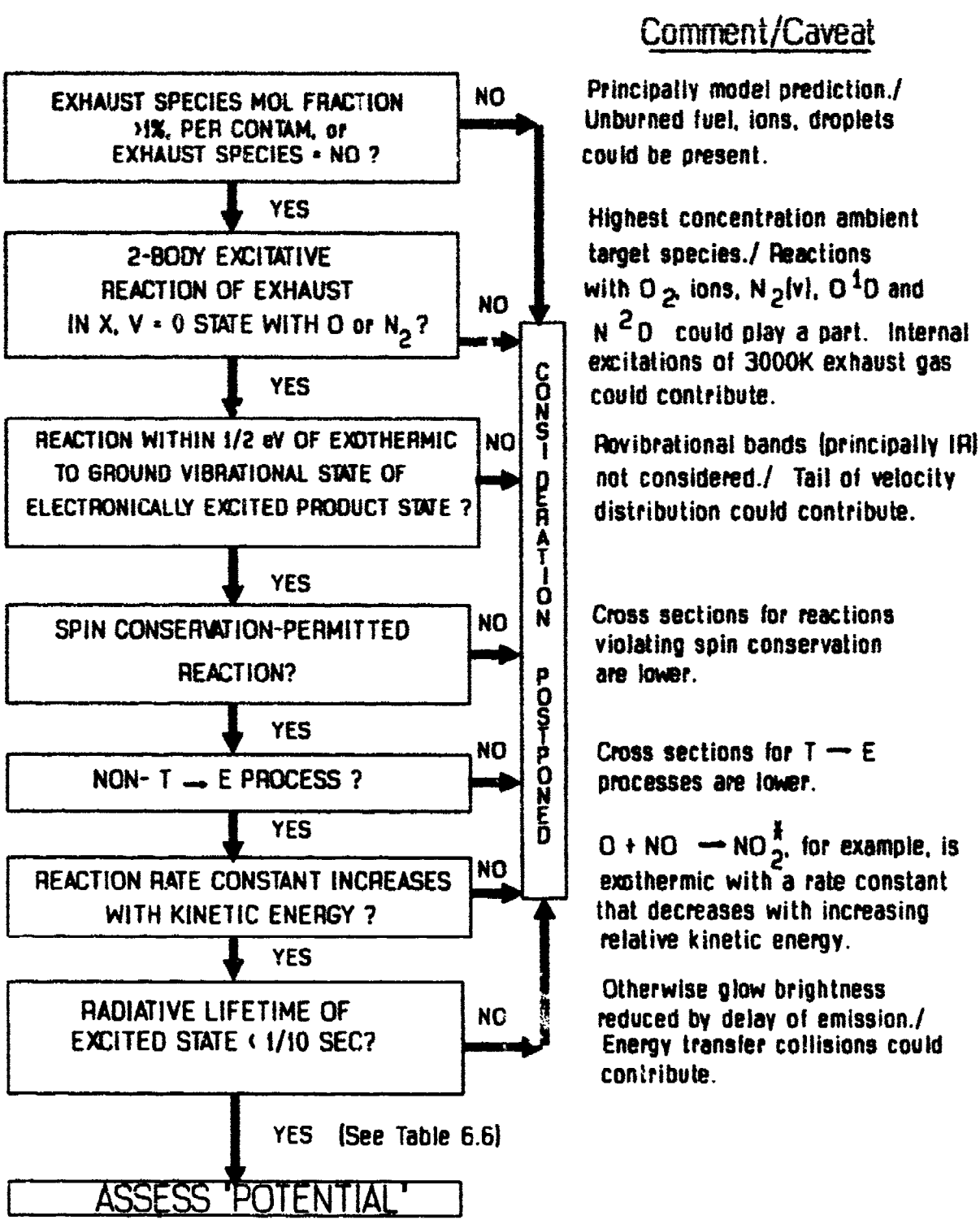

Figure 6.1. Restrictions to the set of excitative reactions between exhaust and atmospheric gas

at sufficiently high rates to merit consideration.

Third, we limit the review to those reactions that are within one-half eV of exothermic to the ground vibrational level of the electronically excited product, for the maximum available kinetic energy. The extra ½ eV allows some leeway for the higher-energy collisions of those exhaust molecules whose relative velocity in the direction of their coherent flow is more than one standard deviation above the mean. As noted, we do not consider vibrationally excited reaction products, which produce principally infrared radiation (an exception is OH (X, $v \geq 4$), whose not-improbable high-Δv transitions lie in the visible).

Fourth, we focus on reactions in which the spin angular momentum vector is conserved, which proceed more rapidly than spin-forbidden reactions. Fifth, we eliminate electronically non-adiabatic processes, that is, collisions without chemical change that leave one of the participants in an excited state (T→E); as pointed out later, these cross sections are estimated to be small compared with those of other collision processes. Sixth, we exclude exothermic reactions whose rate constants are known to decrease with increasing relative kinetic energy, for the simple reason that they become much less likely in the high energy range of interest (a prime example is $NO + O \rightarrow NO_2^*$)--and conversely proceed as persisting chemiluminescence as the exhaust is cooled by collisions.

Seventh, we restrict the review to product excited states with less than ~1/10-sec lifetimes against spontaneous radiation, which is comparable with the time during which the exhaust volumes from the 7.3 km/sec-velocity spacecraft cross their own width (expected to be of the order of 1 km). The persistence of radiation from species in longer-lived upper states has the effect of reducing the mean surface brightness of the glow while increasing its projected area. (That is, an afterglow tail would follow the vehicle's trajectory path.) Excitation transfer by collisions of long-lived species

generally requires longer than 1/10 sec at orbital altitudes; therefore neglect of this transfer of potential energy to a possibly shorter-lived radiative state (an example is $N_2(A)$ with lifetime 2 sec to NO(A) with lifetime 10^{-8} sec, the upper state of the familiar NO γ bands) is not a significant factor in evaluating the plume radiation that could be applied in surveillance. (Similarly, quenching of excited species is not important when the 1/10-sec upper limit is applied.)

This "filtering" of the reactions between exhaust molecules and O and N_2, which are listed in Tables 6.4 and 6.5, leads to the eight reactions most likely to produce such visible and UV emission listed in Table 6.6. We stress once again that this short list is not intended to be definitive, but is merely the result of applying the initial (in part effort-controlling) tests summarized in Figure 6.1; --in particular, some reactions of the highly-reactive unburned fuel and involving the hydrogen atoms present at the higher orbital altitudes (which may, for example, produce $OH^{\dagger}$ by reacting with exhaust H_2O) may turn out to be not significantly less probable. As mentioned above, the ideas presented here would of course apply directly to an expanded list of reactions/excited product species.

Elastic Scattering

Cross sections for elastic scattering near 5 eV are of theoretical interest because they provide upper limits for inelastic scattering rates while giving some insight into the interaction process, and of practical interest because all but the most glancing (small deflection-angle) elastic collisions reduce the kinetic energy of the exhaust species below the barrier heights of the chemiluminous reactions in Table 6.6. (That is, the fraction of exhaust gas molecules that produce optical emissions is in effect the ratio of their excitative cross section to the sum of their elastic plus all other collisional cross sections.)

Table 6.4. Energetically allowed/spin permitted reactions of $O(^3P)$ with principal exhaust gas species (all v"=0)†

Reactants	Products	E_o, eV	E^*, eV	E_{th}, eV	E_{max}, eV
$O(^3P)+H_2O(\tilde{X}^1A_1)$	$OH(X^2\Pi)+OH(X^2\Pi)$	0.73		0.80	5.74
	$OH(X^2\Pi)+OH(A^2\Sigma^+)^*$	4.78	4.05	----	
	$O_2(X^3\Sigma_g^-)+H_2(X^1\Sigma_g^+)$	-0.12			
	$HO_2(^2\tilde{X})+H(^2S)$	2.98			
$O(^3P)+N_2(X^1\Sigma_g^+)$	$NO(X^2\Pi)+N(^4S)$	3.26		3.27	6.91
	$NO(X^2\Pi)+N(^2D)^*$	5.64	2.38	----	
	$NO(X^2\Pi)+N(^2P)^*$	6.83	3.57	----	
	$O(^3P)+N_2(A^3\Sigma_u^+)^*$	6.22	6.22	----	
	$O(^3P)+N_2^*(B^3\Pi_g)^*$	7.39	7.39	----	
$O(^3P)+H_2(X^1\Sigma_g^+)$	$OH(X^2\Pi)+H(^2S)$	0.09		0.39	1.20
$O(^3P)+CO(X^1\Sigma^+)$	$O_2(X^3\Sigma_g^-)+C(^3P)$	5.97		----	6.91
	$O_2(X^3\Sigma_g^-)+C(^1D)^*$	7.23	1.26	----	
	$O_2(a^1\Delta_g)^*+C(^3P)$	6.95	0.98	----	
$O(^3P)+CO_2(X^1\Sigma_g^+)$	$O_2(X^3\Sigma_g^+)+CO(X^1\Sigma^+)$	0.33		2.28	7.92
	$O_2(A^3\Sigma_u^+)^*+CO(X^1\Sigma^+)$	4.72	4.39	----	
	$O_2(B^3\Sigma_u^-)^*+CO(X^1\Sigma^+)$	6.50	6.17	----	
	$O_2(X^3\Sigma_g^+)+CO(a^3\Pi_r)^*$	6.37	6.04	----	
	$O_2(X^3\Sigma_g^-)+CO(a'^3\Sigma^+)^*$	7.25	6.92	----	
	$O_2(X^3\Sigma_g^-)+CO(d^3\Delta_1)^*$	7.91	7.58	----	
$O(^3P)+NO(X^2\Pi_r)$	$O_2(X^3\Sigma_g^-)+N(^4S)$	1.38		1.68	7.04
	$O_2(a^1\Delta_g)^*+N(^4S)$	2.36	0.98	----	
	$O_2(b^1\Sigma_g^-)^*+N(^4S)$	3.02	1.64	----	
	$O_2(c^1\Sigma_u^+)^*+N(^4S)$	5.48	4.10	----	
	$O_2(A^3\Sigma_u^+)^*+N(^4S)$	5.77	4.39	----	
	$O_2(B^3\Sigma_u^-)^*+N(^4S)$	7.55	6.17	----	
	$O_2(X^3\Sigma_g^-)+N(^2D)^*$	3.76	2.38	----	
	$O_2(X^3\Sigma_g^-)+N(^2P)^*$	4.95	3.57	----	

† E_o is the endothermicity of the reaction and E_{th} the measured barrier height; E^* is the electronic energy of the excited species identified by an asterisk, and E_{max} is the maximum available relative kinetic energy from Table 6.2. The asterisk after the state identification indicates that it is excited.

Table 6.5. Energetically allowed/spin permitted reactions of $N_2(X, v=0)$ with principal exhaust gas species (all v"=0)†

Reactants	Products	E_o, eV	E^*, eV	E_{th}, eV	E_{max}, eV
$N_2(X^1\Sigma_g^+)+H_2O(X^1A_1)$	$NH_2(X^2B_1)+NO(X^2\Pi_r)$	5.60	0.80		7.45
	$NH_2(A^2A_1)^*+NO(X^2\Pi_r)$	6.87	1.27	----	
	$N_2O(X^1\Sigma^+)+H_2(X^1\Sigma_g^+)$	3.36		----	
$N_2(X^1\Sigma_g^+)+N_2(X^1\Sigma_g^+)$	$N_2(X^1\Sigma_g^+)+N_2(a'^1\Sigma_u^-)^*$	8.45	8.45	----	9.48
	$N_2(X)+N_2(a^1\Pi_g)^*$	8.59	8.59	----	
	$N_2(X)+N_2(w^1\Delta_u)^*$	8.94	8.94	----	
$N_2(X^1\Sigma_g^+)+H_2(X^1\Sigma_g^+)$	No reactions - insufficient energy			----	1.27
$N_2(X^1\Sigma_g^+)+CO(X^1\Sigma^+)$	$NO(X^2\Pi_r)+CN(X^2\Sigma^+)$	6.55		----	9.48
	$NO(X^2\Pi_r)+CN(A^2\Pi_r)^*$	7.70	1.15	----	
	$NO(X^2\Pi_r)+CN(B^2\Sigma^+)^*$	9.74	3.19	----	
	$CN_2(X^3\Sigma_g^+)+O(^3P)$				
	$NCO(\tilde{X}^2\Pi_i)+N(^2D)^*$	7.94	2.38	-----	
	$NCO(\tilde{X}^2\Pi_i)+N(^2P)^*$	9.13	3.57	-----	
$N_2(X^1\Sigma_g^+)+CO_2(X^1\Sigma_g^+)$	$NO_2(\tilde{X}^2A_1)+CN(X^2\Sigma^+)$	8.89		----	11.6
	$NO_2(A^2B_1)^*+CN(X^2\Sigma^+)$	10.75	1.86	----	
	$NO_2(X^2A_1)+CN(A^2\Pi_2)^*$	10.04	1.15	----	
	$NO_2(X^2A_1)+CN(B^2\Sigma^+)^*$	12.08	3.19	----	
	$NO(X^2P_r)+NCO(X^2\Pi_i)$	7.8			
	$NO(X^2P_r)+NCO(A^2\Sigma^+)^*$	10.62	2.82		
	$NO(X^2P_r)+NCO(B^2\Pi)^*$	11.74	3.94		
	$NCN(\tilde{X}^3\Sigma_g^-)+O_2(X^3\Sigma_g^-)$	13.38			
$N_2(X^1\Sigma_g^+)+NO(X^2\Pi_r)$	$N_2O(\tilde{X}^1\Sigma_g^+)+N(^2D)^*$	7.21	2.38	----	9.82

† E_o is the endothermicity of the reaction and E_{th} the measured barrier height; E^* is the electronic energy of the excited species identified by an asterisk, and E_{max} is the maximum available relative kinetic energy from Table 6.3.

* further indicates excited states

Table 6.6. Exhaust gas reactions meeting the tests illustrated in Figure 6.1

Reactants	Products	E_{th}, eV	E_{max}, eV	$\sigma(E_{max})$, Å^{2}†	Emission System†††
$H_2O(X)+O(^3P)$	$OH(A)^*+OH(X)$	4.83	5.74	0.19	~2400-3500 Å
$CO_2(X)+O(^3P)$	$O_2(A)^*+CO(X)$	6.67	7.92	0.10	Herzberg I, ~2400-4900 Å
	$O_2(B)^*+CO(X)$	8.45			Schumann-Runge, <1900 Å
$NO(X)+O(^3P)$	$O_2(A)^*+N(^4S)$	6.07	7.04	0.06	Herzberg I, ~2400-4900 Å
	$O_2(B)^*+N(^4S)$	7.85			Schumann-Runge, <1900 Å
$CO(X)+N_2(X)$	$CN(A)^*+NO(X)$	≥7.70††	9.48	-----	Red, ~4400-15000 Å
$CO_2(X)+N_2(X)$	$NO_2(A)^*+CN(X)$	≥10.75††	11.6	-----	Yellow-green-IR continuum (see Sec. 3)
	$CN(A)^*+NO_2(X)$	≥10.04††		-----	~4400-15000 Å

† Estimated as described in the text.
†† These figures are the endothermicities E_o of the reactions. No information on the barrier threshold is available.
††† To ground state (X) of excited molecule.

The first-approximation description of scattering between two non-reacting atoms or molecules is the "hard sphere" model (see for example Ref 96), which assumes that the interaction potential V_h at mean radial separation r is spherically symmetric and given by

$$V_h(r) = 0 \text{ for } r > d$$
$$V_h(r) = \infty \text{ for } r \leq d.$$

[Some of the symbols used here of necessity repeat those used in Section 5; each is clearly defined in both Sections.] The simple hard-sphere model is obviously independent of relative energy, in contradiction to most experimental observations. d defines a distance of closest approach, which for spherical colliding partners would equal the sum of their radii. The total cross section σ_h for scattering into all angles is then πd^2, and the resulting rate constant k_h assuming a Maxwell-Boltzmann velocity distribution of both species at the same temperature T is

$$k_h(T) = \sigma_h \bar{v}' = \pi d^2 (8K_B T/\pi\mu)^{1/2}.$$

Here $\bar{v}'$ is the mean relative velocity and K_B is the usual Boltzmann constant. d is customarily approximated (Ref 96) as the Lennard-Jones parameter d_L, which is very nearly equal to the distance of the potential minimum in the so-called "6-12" potential of the two participants. Some values of this parameter, derived from second virial coefficients, are given in Ref's 97 and 98.

When these coefficients are not known for the interaction between chemically different species A and B, an averaging approximation

$$d_L(A \leftrightarrow B) = \tfrac{1}{2} [d_L(A \leftrightarrow A) + d_L(B \leftrightarrow B)]$$

is used (Ref 96, p. 47). Table 6.7 gives hard-sphere diameters and cross sections calculated from this recipe for collisions of the major rocket exhaust species on O and N_2. As d_L of atomic oxygen is not known we used the value for Neon, which is the nearest noble gas atom in the periodic table. (For NO_2 and MMH, which are included only for completeness, we have used values similar to those of CO_2 and $CH_3CH{=}CH_2$ respectively.) Table 6.7 shows that the total elastic hard-sphere cross sections lie within the relatively narrow range ~20-50 $Å^2$ for the species of interest.

This simple model ignores both long-range attractive forces and the finite repulsive force at small separations of the collision participants, whose effects would depend on the initial relative kinetic energy. In the "hard spheres with attraction" model (Ref 96), the potential V_a is assumed to be of the power-law form

$$V_a(r) = Eb^2/r^2 - Cr^n \quad \text{for } r > d$$
$$V_a(r) = \infty \quad \text{for } r \leq d.$$

Here C (whose value will become apparent in the next paragraph), the exponent n (≥ 1), the mean available kinetic energy E ($= \frac{1}{2}\mu\bar{v}'^2$) and b are constants specific to the colliding pair. The impact parameter b is defined as the distance of closest approach in the absence of any interaction. The first (repulsive) term in the expression applying when $r > d$ is the "centrifugal potential", which reflects the possibility that some of the translational motion can be transformed into rotation.

The attractive interactions between exhaust and atmospheric species can be electrostatic or dispersive. "Electrostatic" interactions of the non-polar O atoms and N_2 molecules are with those exhaust species that have permanent dipole moments, such as H_2O. In these dipole-induced dipole collisions, the induction energy averaged over angles of the dipole relative to

Table 6.7. Cross sections for elastic collisions of O and N_2 with species A based on the "hard sphere" model, with d_L (O→O) = 3 Å (see text)

	-Collisions with O-			-Collisions with N_2-	
Species	$d_L(A \leftrightarrow A)$, Å	$d_L(A \leftrightarrow O)$, Å	σ_h, Å^2	$d_L(A \leftrightarrow N_2)$, Å	σ_h, Å^2
H_2O	2.3	2.7	23	3.0	28
N_2	3.7	3.4	36	3.7	43
H_2	2.9	3.0	28	3.3	34
CO	3.8	3.4	36	3.8	45
CO_2	4.1	3.6	41	3.9	48
NO	3.2	3.1	30	3.5	38
NO_2	4.1	3.6	41	3.9	48
MMH	5	4	50	4.4	61

Table 6.8. Average polarizabilities α, dipole moments M', and ionization potentials I of reactants

Species	α, Å^3	M', 10^{18}esu cm	I, eV
H_2O	1.45	1.85	12.6
H_2	0.80	0.11	15.4
CO	1.95	0	14.0
CO_2	2.6	0	13.8
NO	1.7	0.16	9.26
NO_2	3.0	0.32	9.8
O	~ 0.8	0	13.6
N_2	1.75	0	15.6

Table 6.9. Induction and dispersion energies calculated for interactions between O and exhaust species

Species	r = d_L, Å	ϕ_{ind}, eV	ϕ_{dis}, eV
H_2O	2.7	4.4×10^{-3}	2.9×10^{-2}
N_2	3.4	0	9.9×10^{-3}
H_2	3.0	0	9.5×10^{-3}
CO	3.4	3.9×10^{-6}	1.0×10^{-2}
CO_2	3.6	0	9.9×10^{-3}
NO	3.1	1.4×10^{-5}	1.2×10^{-2}
NO_2	3.6	2.4×10^{-5}	9.4×10^{-3}

the trajectory direction is (Ref 98, p. 987)

$$\phi_{ind} = - \alpha_A M'_B{}^2 / r^6,$$

where α_A is the polarizability of (target) species A and M'_B the dipole moment of exhaust species B. Exhaust molecules having zero permanent dipole moments interact through dispersion (Van der Waals) forces; an approximate form is (Ref 99)

$$\phi_{disp} = - \frac{3 \; I_A I_B}{2(I_A + I_B)} \cdot \alpha_A \alpha_B / r^6,$$

where the I's and α's are ionization potentials and polarizabilities. Both the dispersion and induction interactions can be seen to have inverse sixth-power dependence on the "mean" separation distance r of the exhaust and target species.

The three-direction-averaged polarizabilities, dipole moments, and ionization potentials of these species (from Ref 97) are restated in Table 6.8. (The polarizability of O is taken to be one-half that of O_2.) The induction and dispersion energies between O and several other molecules calculated from these parameters and evaluated at the "hard-sphere" distances in Table 6.7, are listed in Table 6.9. The calculated dispersion and induction energies are on the order of 0.01 eV or less. These energies of attraction between neutral species are thus much smaller than the directed translational energies of the exhaust products.

With this material as background, we return to the contribution of attractive potentials to the elastic scattering cross sections. The largest value of the impact parameter b is that required to surmount the potential barrier. The general form of b_{max} for attractive potentials of the form $-Cr^{-n}$ is derived in Ref 96 (p.71); for n = 6 the cross sections are

$$\sigma_a(E) = \pi d^2 \left[1 + (6.75\ E_d/E)^{1/3}\right] \qquad E \leq 6.75\ E_d$$
$$\sigma_a(E) = \pi d^2 \qquad E > 6.75\ E_d,$$

where E_d is the attractive energy at the hard sphere diameter d. In the present application, E is typically 1-10 eV (except for H_2 (Tables 6.2, 6.3)) and E_d is on the order of 0.01 eV (Table 6.9). The exhaust gas interactions are thus in an energy regime in which the attractive forces considered in this second-approximation model are not significant.

A third approximation, the "variable hard sphere" model, takes into account the repulsive forces between the energetic colliding particles (Ref 100). The cross sections for elastic collision are assumed to depend inversely on a power P of the relative kinetic energy that turns out to vary between 0.2 and 1.2 for exhaust-ambient species pairs. The cross section at E is then heuristically fitted relative to standardized "reference" values σ_{ref} and E_{ref}

$$\sigma_v(E) = \sigma_{ref}\ (E_{ref}/E)^P.$$

These reference values are determined for individual species from measurements of the temperature dependence of gas viscosity (and data from molecular beam experiments), and the values for collision pairs are then interpolated by weighting/modeling. Using σ_{ref}'s, E_{ref}'s and P's derived for and applied in CHARM (Ref 89), we calculate variable hard-sphere elastic cross sections of 7 $Å^2$ and 14 $Å^2$ for H_2O + O and H_2O + N_2 collisions respectively at the maximum relative velocity of 11.4 km/sec. These are about 1/3 and 1/2 of the "hard-sphere" cross sections in Table 6.7 (which are known to be overestimates at these relatively high relative translational energies).

In summary, we find that the cross sections for elastic collisions of the most energetic exhaust species with air are of the order of 10 $Å^2$. This figure should be kept in mind as a

reference for evaluating the inelastic-collision cross sections for thei- relative production of optical emissions.

Inelastic Scattering: Background

Table 6.6 lists the eight exhaust reactions meeting the criteria stated in Figure 6.1; the threshold energy E_{th} of these excitative reactions, estimated by the simple procedure of adding the internal energy E^* of the product electronic state to the barrier height for production of the ground electronic state determined from the available laboratory reaction-rate data (in the way described below); the maximum kinetic energy E_{max} available in collisions with O or N_2, repeated from Table 6.2 or 6.3; and, in the second to last column, an estimate of the excitative cross sections at that maximum relative energy made by extrapolating the chemistry-laboratory rates at much lower "temperatures" as also described below. These estimated cross sections should be regarded as approximate, as they represent a far extrapolation from classical "bulk" (or "bulb") furnace or shock-tube experiments that determine reaction rate coefficients--in effect, cross sections averaged over the velocities and (comparably important) the internal-excitation states of the reactants and products. A critique of the procedure applied in deriving these cross sections appears in a later subsection.

State-specific cross sections can also be measured directly by the more technologically demanding method of crossed molecular beams, usually with laser-based and/or mass-spectrometric diagnostics of the products (and in some cases selection of internal states of the reactants). Because of the difficulty of producing sufficiently high-brightness atomic and molecular beams with energies of a few eV, only a few endothermic reactions have been investigated by this method near threshold, and in virtually none of these have the internal excitation states of the product species been identified; refer to Table 6.11. Unfortunately none of the reactions between

rocket exhaust gases and atmospheric O or N_2 in Table 6.6, even those producing products in ground electronic states, have been studied by this method; nor have the reverse (exothermic) reactions been investigated. Nonetheless the information developed for "analogous" endothermic atom-interchange reactions provides some basis for estimating the dependence of the partial cross sections on translational energy above the reaction barrier, as is also discussed below.

Additionally, cross sections for reactive scattering can in principle be calculated from intermolecular potentials in a straightforward (if computationally very complicated) manner. However only a limited number of reliable quantum-mechanically computed potential curves or surfaces are available, and these are so far confined to a few two- or three-atom systems with relatively few orbital electrons, e.g., H_2, HF, H_3, and FH_2 (and do not include the interacting species in Table 6.6). The procedure is to solve the electronic Schroedinger equation for "fully-specified" interactions at a fixed relative velocity, and then average over the experimentally-uncontrollable collision parameters such as dipole orientation and impact parameter b. The unreliability of the potentials of the reactants-intermediates (i.e., transition states)-products of interest here, along with the sheer volume of effort required to perform these calculations with adequate output accuracy, makes this ab initio approach a cost-ineffective enterprise of questionable absolute accuracy.

The theory of reactive scattering does, however, provide some basis for understanding the behavior of partial cross sections in terms of the underlying intermolecular potential surfaces. For instance, classical collision theory using only rudimentary potentials (Ref 96, pp.70-72 and 78-84) is able to show that, quite generally, cross sections for collisions dominated by long-range attractive interactions decrease with increasing kinetic energy, while those for reactions dominated by short-range repulsive forces increase monotonically above

threshold to approach kinetic cross sections asymptotically at high energies. Furthermore, detailed trajectory calculations on more sophisticated potential surfaces (Ref 101) have shown that, where the reactive potentials are free from local minima, direct collision dynamics prevails, i.e., no true transition complexes are formed, and dividing surfaces along reaction paths are rarely crossed more than once. (This finding has direct bearing on a fundamental postulate of Transition State Theory, to be briefly discussed below.) Other detailed studies of these potential surfaces (Ref 102) have also shown that, for highly exothermic reactions, the potential barrier lies "early" on the reactants' side (entrance channel), and most of the energy is released as the reactants approach, preferentially into vibrational modes. As the exothermicity is decreased (other parameters staying the same), the barrier moves further along the reaction path, and energy is released late in the process and channeled principally into relative translational motion of the separating products. (In a later subsection, we shall come back to these ideas in a converse form--preferential enhancement of endothermic reactive cross sections by vibrational excitation of reactants.)

Table 6.10 presents "bulk" reaction-rate data from the critical (principally, Ref's 103) and original literature for several endothermic reactions of oxygen atoms at temperatures up to a few thousand K, including three with rocket exhaust products listed in Table 6.6. (Some of these rate data were derived by applying detailed-balance arguments to the reverse bulk reaction.) In these experiments, as noted, the excitation states of the product species are not identified, nor is the role of internal excitation of the reactants--which is not insubstantial at these high temperatures--clarified. The provisional estimates of excitative atom-interchange cross sections in Table 6.6 are based on this laboratory data set. We have not found similar rate data for endothermic reactions between exhaust gas species and N_2, which is well known to be

much less reactive than $O(^3P)$, a free radical with two unpaired electrons available for bonding.

The rate constant k(T) for reactive collisions at initial (large-separation) relative kinetic energy $E = \frac{1}{2}\mu v^2$ is as usual the average over the relative velocity distribution of the (translational velocity-specific) rate coefficient. That is, $k(T) = \langle v\sigma(v)\rangle$, where $\sigma(v)$ is the bimolecular reaction cross section averaged over all quantum states of the reactants and products. Thus (as derived in Ref 96, for example) if the kinetic energies of the reactants are Maxwell-Boltzmann-distributed at temperature T, then

$$k(T) = (\pi\mu)^{-\frac{1}{2}} (2/K_BT)^{3/2} \int_0^\infty \sigma(E)\, E \exp(-E/K_BT)\, dE.$$

This equation, which has the form of a Laplace transform, can be inverted to obtain the energy dependence of the cross section using the method of steepest descent (Ref 104). If the laboratory reaction-chamber and shock-tube data show a dependence of the form

$$k(T) = k_o(K_BT)^{n'} \exp-[E_{th}/K_BT]$$

--as has been fitted to those reactions of Table 6.6 for which we have found experimental results--, then the result of the inversion is (Ref's 104, 105)

$$\sigma(E) = [(\pi\mu/8)^{\frac{1}{2}} k_o/\Gamma(n'+ 3/2)][(E - E_{th})^{n'+\frac{1}{2}}/E],$$

where Γ is the usual gamma-function. This relationship obviously holds only for relative collision energies greater than the threshold energy E_{th}, which is at least equal to, and in most cases greater than, the endothermicity (see Table 6.4). Note that the cross section depends on a power of the energy above this barrier $E - E_{th}$, so that it increases relatively sharply with available energy before its slope decreases (or if

n'<1, it begins to decrease) due to the E^{-1} term. That is, the cross section for producing visible or UV radiation will be sensitive to the angle between the exhaust axis and Orbiter's trajectory vector, as well as to the actual (not accurately known) directed velocity of the gas.

Measured reaction rate constants and the cross sections at maximum relative energy derived from them for reactions of exhaust gas species with $O(^3P)$ applying this formalism, are listed in Table 6.10. For products in excited electronic states--which are the only ones of interest here--we made the assumption that the same functional form of σ (and thus $k(T)$) holds, with E_{th} equal to the sum of the threshold energy for ground-state products plus the energy of the excited state. That is, we assumed that the chemical process that results in the exit channel involving the specific excited state is "similar" to that forming ground-state products only. (We return to this important point later.)

In addition, we adjusted the partial rate coefficient k_o to reflect the difference in statistical factors relative to those for products in ground states. This correction to the predicted cross sections is most likely small compared with the inherent error in extrapolating these typically ¼-electron-volt temperature collision data to the near-monochromatic several eV of exhaust-air collisions (more on this also below). We derived these statistical factors, which are also listed in Table 6.10, from the correlation rules for spin angular momentum and orbital symmetry as given by Ref 96. For a three-atom system, the symmetry is C_s at all times during the reaction; in this point group electronic states have symmetry A' or A", i.e., the electronic wavefunctions are either symmetric or antisymmetric with respect to reflection in the plane containing the three atoms. Terms for the molecular states of products and reactants in C_s symmetry were obtained by forming all possible combinations of allowed spin and orbital states. From these correlations, we define the "statistical factor" for each

Table 6.10. Cross sections for exhaust gas species with $O(^3P)$ estimated from laboratory data

Reactants	Products	Statistical Factor	k(T), cm^3/molecule sec	Ref	T, K	$\sigma(E)$, A^2	E_{th}, eV	E_{max}, eV	$\sigma(E_{max})$, A^2	E_{max}/E_{th}
$O(^3P)+H_2O(\tilde{X})$	$OH(X)+OH(X)$	4/3	$1.1\times10^{-10}\exp(-9240/T)$	103a	300-2000	$2.31(E-E_{th})^{1/2}/E$	0.80	5.74	0.89	7.2
			$7.6\times10^{-15}T^{1.3}\exp(-8605/T)$	107	400-2000	$6.2\ (E-E_{th})^{1.6}/E$	0.74		50	
	$OH(X)+OH(A)^*$	2/3					4.83		0.19	
$O(^3P)+N_2(X)$	$NO(X)+N(^4S)$	2/3	$1.3\times10^{-10}\exp(-38000/T)$	103b	2000-5000	$3.00(E-E_{th})^{1/2}/E$	3.27	6.91	0.83	2.1
	$NO(X)+N(^2D)^*$	10/3					5.65		2.44	
	$NO(X)+N(^2P)^*$	2					6.84		0.41	
$O(^3P)+H_2(X)$	$OH(X)+H(^2S)$	2/3	$3.0\times10^{-14}T\exp(-4480/T)$	103a	400-2000	$2.22(E-E_{th})^{3/2}/E$	0.39	1.20	1.35	3.1
			$1.6\times10^{-11}\exp(-4570/T)$	103d	298- 830	$0.15(E-E_{th})^{1/2}/E$	0.39		0.12	
			$1.8\times10^{-20}T^{2.8}\exp(-2980/T)$	107	298-2500	$4.19(E-E_{th})^{3.5}$	0.26		1.74	
$O(^3P)+CO_2(\tilde{X})$	$CO(X)+O_2(X)$	1/3	$2.8\times10^{-11}\exp(-26500/T)$	103c	1500-3000	$0.69(E-E_{th})^{1/2}/E$	2.28	7.92	0.21	3.5
	$CO(X)+O_2(A)^*$	1/3					6.67		0.097	
	$CO(X)+O_2(B)^*$	1/3					8 45		0	
	$O_2(X)+CO(a)^*$	2/3					8.32		0	
$O(^3P)+NO(X)$	$N(^4S)+O_2(X)$	1/6	$2.5\times10^{-15}T\exp(-19500/T)$	103b	1000-3000	$0.45(E-E_{th})^{3/2}/E$	1.68	7.04	0.79	4.2
	$N(^4S)+O_2(a)^*$	2/9					2.66		0.79	
	$N(^4S)+O_2(b)^*$	1/9					3.32		0.31	
	$N(^4S)+O_2(c)^*$	1/9					5.78		0.060	
	$N(^4S)+O_2(A)^*$	1/6					6.07		0.061	
	$N(^4S)+O_2(B)^*$	1/6					7.85		0	
	$O_2(X)+N(^2D)^*$	5/6					4.06		1.64	
	$O_2(X)+N(^2P)^*$	1/2					5.25		0.46	

E_{th} for excited states is taken to be equal to the energy of the excited states plus E_{th} for the ground-state reaction (obtained from the rate equation).

The energy-dependent cross section for reactions yielding products in excited states are taken to be the same as those for corresponding reactions yielding ground-state products except for values of the threshold energies and statistical factors.

excitative reaction as the fraction of product states which correlate with states of the reactants. (For example, in the reaction $O(^3P) + N_2(X^1\Sigma_g^+)$ the reactants can combine to give 9 states (counting multiplets): one $^3A'$ and two $^3A''$ states; and the products can combine to give 16 states: $^3A'$, $^3A''$, $^5A'$, and $^5A''$. Only 6 of the product states $^3A'$ and $^3A''$ have the same spin and orbital symmetry of the reactant states; the statistical factor calculated for this reaction is thus 6/9, shown in table 6.10 as 2/3.) The statistical factors for the O + H_2O reactions are not strictly applicable, because the atoms in the transition state (H_2O_2) are not necessarily co-planar; they are meaningful only if the reaction path strongly favors a planar configuration. (Since the ground-state CO_2 molecule is linear, the (CO_3) transition state is presumably planar.)

The above procedure results in the three maximum cross sections for chemiluminous reactions of shuttle exhaust with the atmosphere's $O(^3P)$ atoms in the next to last column of Table 6.6. These are all of order 1/10 $Å^2$, or two orders of magnitude smaller than the nominal elastic cross sections discussed earlier. In view of the "loss" of reactive species represented by most elastic collisions, this finding would indicate that only about 10^{-2} of the exhaust molecules H_2O, CO_2, and NO (which themselves comprise about half the molar abundance) would result in near-prompt emission of visible and ultraviolet photons.

The procedure would produce partial cross sections for excitation of $O_2(B)$ molecules--the upper state of the vacuum-ultraviolet Schumann-Runge system--if we selected an E_{max} above the reaction barrier E_{th} for reactions of NO with O. The corresponding barriers for the three potentially "prompt" chemiluminous reactions of exhaust species with the atmosphere's N_2 molecules, and the rate coefficients, are not known; the numbers tabulated for them in the third column of Table 6.6 are the endothermicities (which can be seen are less than the maximum available translational energy E_{max} but may be smaller than E_{th}). It is doubtful that the cross sections for the

excitative atom-exchange reactions with nitrogen molecules exceed those involving oxygen atoms.

Reliability of Excitative Cross Sections Derived from Laboratory Kinetic Data

We turn now to a brief discussion of the reliability of excitative cross sections derived by this "brute force"--albeit sole available--procedure. We start by comparing the results in Table 6.10 with the predictions of Transition State Theory (TST; Ref 96), which applies the fundamental assumptions (among others): 1) the nuclear and electronic motions can be separated (Born-Oppenheimer approximation); 2) the state populations of the intermediate as well as the reactants follow a Maxwell-Boltzmann distribution at the kinetic temperature; and 3) species in this transition state can be clearly identified as forward or reverse-moving without a need to account for recrossing of the surface dividing reactants from products. In Ref 106 TST is used to derive an expression for cross sections that, when averaged over the internal states of the products, is proportional to the ratio of density of states of the transition complex to that of the reactants at the total energy E. In the classical harmonic-oscillator, rigid-rotor approximation, the cross section takes the form

$$\sigma(E) \sim (E - E_{th})^q / E^p.$$

Thus when $E >> E_{th}$, $\sigma \sim E^{q-p}$. Values of the exponent $s = q - p + 1$ expected from TST in the limit of high E, which would be directly comparable with the exponent $n' + \frac{1}{2}$ derived above (and observed in molecular beam experiments), are given in Table 6.11 for linear and nonlinear geometries of the transition-state complex.

The results from crossed-molecular beam experiments, unlike bulk experiments, are values of $\sigma(E)$ at specific, discrete collision energies. It can be seen from Table 6.11 that s-

Table 6.11. Values of the exponent s for reactive cross sections $\sigma(E) \sim (E-E_{th})^s/E$, molecular beam and exhaust gas reactions

Molecular Beam Reaction	s	Ref	s (From TST) linear	s (From TST) non-linear	E_{max}/E_{th}
$K+HCl \rightarrow KCl+H$	1	120	2	1.5	7
$D+H_2 \rightarrow DH+H$	1	121	2	1.5	1
$Hg+I_2 \rightarrow HgI+I$	1.5	122	2	1.5	~2
$O+H_2S \rightarrow HSO+H$	1-2	123	3.5	3	1.5
$O+C_2H_2 \rightarrow CHO+H$	2-3	124		3	3
$O+C_2H_4 \rightarrow C_2H_3O+H$	2-3	124		3	5
Exhaust Gas Reaction					
$O+H_2O \rightarrow 2OH$	0.5, 1.8	103a, 107	3.5	3	7.2
$O+CO_2 \rightarrow CO+O_2$	0.5	103c	3	2.5	3.5
$O+NO \rightarrow O_2+N$	1.5	103b	2	1.5	4.2
$O+N_2 \rightarrow NO+N$	0.5	103b	2	1.5	2.1
$O+H_2 \rightarrow OH+H$	1.5, 3.3	103a,d, 107	3.5	3	3.1
$O+CO \rightarrow O_2+C$	no data		2	1.5	

values predicted by TST and observed in molecular beams are in general agreement (an exception is O + H_2S), which lends some confidence in the application of TST to exhaust species-air collisions. In contrast the s-values for exhaust reactions derived from bulk rate constants, except for O + NO and perhaps O + H_2, are all substantially lower than predicted from TST. In view of the dependence of $\sigma(E - E_{th})$ on s, this finding would imply that the actual excitative reaction cross sections are higher than those listed in Table 6.10.

This discrepancy may be due to the form of the relationship between cross section and rate constant given earlier, which restated is $\sigma(E) \sim (E - E_{th})^s/E$ where the pre-exponential temperature dependence of k(T) is of the form $T^{s-½}$. Unfortunately, it turns out that the fit to laboratory rate data over their necessarily-limited temperature ranges is much more sensitive to the highly-variable exponential term than to the power of T; in consequence values of s--and hence the energy-dependence of cross sections in the few-eV range--are subject to severe experimental uncertainty when obtained from bulk kinetic data (unlike the threshold energy of the reaction).

This qualitative finding points to a fundamental difficulty in attempting to recover $\sigma(E)$ from extrapolations of k(T), which is of the type that characteristically arises whenever one component of a transform pair (such as Laplace, Fourier) is to be obtained from the other that is not completely specified over the full--infinite--range of its variable. To illustrate the high sensitivity of cross sections to the form of k(T), we direct attention to two examples from the reaction-rate literature in Table 6.10. For O + $H_2O \rightarrow 2OH(X)$, Ref 103a recommends $k(T) \sim T^0$, yielding $\sigma(E) = 2.3\ (E - E_{th})^{0.5}/E$ or 0.9 A^2 at E = 5.74 eV; and Ref 107 recommends $k(T) \sim T^{1.3}$, yielding $\sigma(E) = 16\ (E - E_{th})^{1.8}/E$, or 50 A^2 (!) at that energy. For the O + $H_2 \rightarrow OH(X) + H(^2S)$ reaction, Ref 103a recommends $k(T) \sim T^1$, yielding $\sigma(E) = 2.2\ (E - E_{th})^{1.5}/E$, or 1.35 A^2 at 1.20 eV; and Ref 103d recommends $k(T) \sim T^0$, yielding

$\sigma(E) = 0.15\ (E - E_{th})^{0.5}/E$, or 0.12 A^2.

In this connection, we note that the higher the ratio E_{max}/E_{th} (last column of Tables 6.10 and 6.11), the larger the range of extrapolation necessary (since the kinetic data reported in these tables are all taken in temperature ranges where the peak of the Maxwell distribution is considerably less than E_{th}), and hence the larger the uncertainty in the value given for σ (E_{max}).

A second potential source of error in the extrapolation of bulk reaction rate data is neglect of the effect of vibrational (and even electronic) excitation of the reactants on the "lumped-parameter" laboratory rate coefficient. If (as discussed elsewhere in this Section) the cross sections for reactions of these excited species are substantially higher than those of the ground-state molecules, the rate coefficients for ground-state reactants in Table 6.6 would be high upper limits.

A third potential source of error, also mentioned earlier, is the assumption that the functional forms of cross sections are the same for reactions yielding products in ground and in electronically excited states, with E_{th} for the latter being the sum of the threshold for ground-state products plus the potential energy of the excited state. This assumption might not hold for the reactions of interest here. Measurements of activation energies in the chemiluminescent reactions of Sr with the halide molecules Cl_2 and Br_2 at ≤ 4 eV collision energies show both (partially) confirming examples and counter-examples (Ref 108). The difference in thresholds for yielding SrCl(A) and SrCl(C) is indeed equal to the difference in electronic energies of the two excited states of this molecule; however the analogous reactions yielding SrBr(X), (A), and (B) do not show such simple behavior. Whether the assumption used is valid or not depends on the reaction dynamics on the particular potential surfaces involved.

If the pre-exponential factors derived from rate constants are assumed to be valid for functional forms of the cross

sections having an s-dependence of 2, the calculated cross sections for producing ground-state products at the highest relative exhaust kinetic energies are on the order of 1-10 A^2. The classical trajectory calculations of both Ref's 109 and 110 for the $O(^3P) + H_2(v) \rightarrow OH(v) + H$ reaction suggest that the cross sections for H_2 (v=0) are ~2 A^2 (at low rotational quantum number J) for a relative kinetic energy of 1.2 eV. This is close to two of the values (1.35 A^2 and 1.74 A^2) obtained by extrapolating bulk rate constant data. Nonetheless, because of the sensitivity of the cross section to the form of the rate constant and the other errors inherent to the method, the estimates of excitation cross sections in Table 6.6 must be considered uncertain by factors of at least 10.

Comments on the Exhaust Reaction Set

In this concluding subsection we provide justification for, and further comments on, our paring-down of the potentially-chemiluminous reactions of exhaust molecules summarized in Figure 6.1 and discussed in a preliminary way earlier in the text.

First, we selected 1% as the cutoff of the predicted mole concentration of exhaust species because of both the steep fall-off below that fractional concentration (see Table 6.1) and the lack of a priori evidence that any of the minor exhaust products has an anomalously high probability of exciting optical radiations. The information about nitric oxide molecules in the exhaust of MMH-N_2O_4 engines, along with the known tendency of NO to be "frozen in" at greater than equilibrium concentrations when "airlike" mixtures are rapidly cooled (for example, in atmospheric nuclear explosions), was judged sufficient for their inclusion. One of the reactions of NO (with O) appears on the final list in Table 6.6. We neglected reactions involving ambient ions (relative concentrations ~10^{-4}) and exhaust ions (predicted relative concentrations ~10^{-8}) because the "Langevin" cross sections for ion-neutral reactions (Ref 96, pp. 84-85 and 189) are typically only about a factor 10 higher than hard-

sphere cross sections between uncharged particles. Similarly, the strong long-range attractive coulombic potential between ions of opposite charge, which leads generally to reactive cross sections approximately 10^3 higher than hard-sphere (Ref 96, pp. 187-188), does not compensate for the low fractional concentrations of both exhaust and target ions.

Omission of reactions with O_2, which is only about 1/15 as abundant as O at orbital altitudes, is not as readily justified. (Indeed, $[O_2]$ may be enhanced within a few spacecraft diameters by recombination of thermospheric O atoms catalyzed by exposed surfaces.) Vibrational excitation of the exhaust products is neglected principally because attempts to include it would overly complicate this initial review (little direct information is available about the vibrational enhancement of the reaction rates of these species), and because estimates of the excited-state populations in the presumably partially-relaxed exhaust gas are likely to be of low accuracy. Classical trajectory calculations on collinear atom-diatomic molecule reactions (Ref 102) show that if the potential barrier lies in the entrance channel to the reaction path (i.e., in the approach of the reactants), translational energy is more effective than vibrational energy in overcoming the barrier; and conversely that if it lies in the exit channel, vibrational energy is more effective in helping to "turn the corner" (provided of course that the vibration has the right phase). These predictions have been borne out by experiment; for example (Ref's 111, 112) the reaction of H_2 (v=1) with $O(^3P)$ to produce OH + H proceeds $\sim 10^3$ times faster at 300K than with H_2(v=0), a result in approximate agreement with trajectory calculations using both a London-Eyring-Polanyi-Sato potential surface (Ref 109) and an ab initio potential surface (Ref 110).

With the assumption that the reaction barrier $E_{th}^{\dagger}$ is lowered by an amount proportional to the vibrational energy E_v available--i.e., $E_{th}^{\dagger} = E_{th} - \gamma E_v$, γ thus being a measure of the effectiveness of vibrational quanta in overcoming the barrier

height--, Ref 113 calculated $\gamma \leq 0.3$ for the $H_2(v) + O(^3P)$ reaction. This result is in approximate agreement with the experimental $\gamma = 0.38$ (Ref 111). An entirely different approach based on information theory, the "surprisal" formalism (Ref 114), leads to the same form of vibrational enhancement of endothermic reactions as the γ-parameter method. For reactions between hydrogen or halogen atoms with hydrogen halide molecules, the "surprisal" method predicts γ ranging from 0.78 to 1.62, indicating that vibrational energy is much more effective in overcoming potential barriers. This finding would imply that these barriers lie later in the exit channel than for the $H_2(v) + O(^3P)$ reaction. On the other hand, as vibrational energy appears only as effective as translational energy in promoting the $N_2(X) + O(^3P) \rightarrow NO(X)\ \ N(^4S)$ reaction, the barrier of this reaction (which is within 1/10 eV of the endothermicity) must lie close to the "corner" of the reaction path (Ref 115). Taking into account vibrational excitation of the exhaust products--with, say, population distributions predicted from the 3000K kinetic temperature of the gas, partially relaxed by collision limiting as it expands and its density decreases--is a next logical step in assessing the chemiluminescence from the exhaust plume.

Proceeding to the third item in Figure 6.1, the relative contribution of <u>energetic exhaust molecules</u> to the overall reaction rate constant can be straightforwardly estimated as small. As shown above, the rate coefficient $k(T) \sim \int_0^\infty \sigma(E)\ E \exp(-E/K_BT)\ dE$; therefore the fractional error that would result from ignoring reactions of particles with $E > E_{max}$ is

$$\Delta = \frac{\int_{E_{max}}^\infty \sigma(E)\ E \exp(-E/K_BT)\ dE}{\int_0^\infty \sigma(E)\ E \exp(-E/K_BT)\ dE}.$$

For T = 3000K (¼ eV), $\sigma(E)$ of the form $(E-E_{th})^0/E$ (i.e., s = 0), and $E_{max}-E_{th}$ = ½ eV, $\Delta = (\int_2^\infty e^{-x}dx)/(\int_0^\infty e^{-x}dx) \approx 20\%$.

This error is small compared with the factor--10 uncertainty in the cross sections mentioned above in connection with Laplace-transforming and extrapolating laboratory rate coefficients to the much higher relative impact energies of exhaust gas. We conclude that the tail of the Maxwell-Boltzmann velocity distribution of the gas and target air does not substantively change the conclusions of our review of the chemiluminous reactions.

Fourth, spin-forbidden reactions--those for which the reactant and product electronic states do not correlate with any state of the transition complex having the same spin-orbital symmetry (see earlier discussion on statistical factors)--are omitted because it is generally believed that their cross sections are lower than those for spin-allowed transitions. (An example of a spin-forbidden reaction is $CO(X^1\Sigma_g^+) + N_2(X^1\Sigma_g^+) \rightarrow NCO\ (X^2\Pi_g) + N(^4S)$: the reactants correlate only with the singlet manifold of NCO.) The probability that the system undergoes a transition between two states of different spin multiplicity is determined by the spin-orbit coupling term, the slopes of the diabatic (non-crossing) potentials in the vicinity of the crossing, and the relative velocity during the collision (see Ref 116). Because the magnitudes of the spin-orbit interaction and the shapes of the potential surfaces are in general not known, generalized estimates for these transition probabilities cannot be made. However, since these transitions take place only insofar as spin and orbital (or electronic and nuclear) motions are coupled, a reduced probability should be expected (Ref 96).

Fifth, electronically non-adiabatic (T→E) collisions are even less probable. This conclusion is based principally on measurements and theory of the excitation of hydrogen atoms by energetic neutral atoms and molecules, and on production of ions in neutral-neutral collisions. (We have not found experimental studies of neutral ground-state atom-molecule or molecule-molecule collisions in which the molecule is left in an excited

state.) Extrapolation to 10 eV of the data from collisions of H with rare gas atoms at 1-25 keV (Ref 117) and theoretical values (Ref 117 and references therein) give cross sections of the order of 10^{-2} Å^2 to as low as 10^{-6} Å^2 for population of the H(^{2}S) and H(^{2}P) states. Similarly, the data of Ref 118 for collisions of H with NH_3 and CH_4 extrapolate to ~10^{-2} Å^2 and ~10^{-3} Å^2 respectively for populating these atomic states at 10 eV.

A less direct approach to estimating T→E cross sections involves a comparison with the more easily measured cross sections for production of ions. For example the total ionization cross sections have been measured for collisions of H with Ar in the energy range 5-20 keV (Ref 119), in connection with which approximate potential energy curves were derived for H + Ar, H^- + Ar^+, and H^* + Ar and H + Ar^*. The intersection of the H + Ar curve with those of the excited-state species pairs are shown to take place at much higher energies (~20-30 eV) than the intersections with the curves for the ionic states (~12 eV), which implies that the energetically-favored mechanism for electronic excitation in these neutral collisions may involve prior formation of ionic states. If this is indeed so, the cross section for electronic excitation would necessarily be less than that for ion formation [at relatively low impact energies]. Extrapolation to 10 eV of the $H^+ + e^-$ + Ar and H^- + Ar^+ cross sections (Ref 119) gives ion production cross sections of about 10^{-4} Å^2, so that the cross sections for internal excitation in these collisions would be even smaller. Further, the cross sections for total ion production in collisions of N_2 and CO with CO, N_2, NO, CH_4 and CO_2 (Ref 73) ranged from 3×10^{-3} Å^2 to 2×10^{-2} Å^2 at 10 eV; if the creation of "precursor" ionic states are involved in the formation of excited states in these collisions, then the T→E cross sections would be expected to be even smaller. The totality of experimental and theoretical evidence thus suggests that the excitative cross sections in the energy region of interest are less than 10^{-2} Å^2. (Omitting T→E processes means excluding,

among others, reactions of NO with O and N_2 to yield NO^* (A, B, C, D) responsible for the well-known γ, β, δ, and ϵ bands.)

Sixth, the few rate constants that decrease with increasing kinetic energy almost all apply to radiation- or third-body stabilized, and hence very slow, reactions. (The reaction of MMH with the atmosphere's O atoms, not considered because of the predicted low concentrations of unburned fuel in the exhaust, may be an exception.)

Seventh, radiative lifetimes >1/10 sec lead to low-brightness, albeit persisting, glow volumes. This restriction excludes reactions that yield N_2 ($A^3\Sigma_u^+$), N_2 ($a'^1\Sigma_u^-$) [but not N_2 ($a^1\Pi_g$), the upper state of the ultraviolet Lyman-Birge-Hopfield system; see Section 4], and CO ($a^3\Pi_r$). We have included for completeness the 0.14-0.18 sec lifetime O_2 ($A^3\Sigma_u^+$) state, which is the upper level of the ~2400-4900 Å Herzberg I bands; the remaining low-lying triplet and singlet states of O_2 shown in Figure 2.1 have much longer radiative lifetimes.

Summary

Figure 6.1 summarizes the constraints we applied in identifying the principal ultraviolet and visible radiations from the exhaust plume. Among the potentially important reactions not considered are those with atmospheric O_2 (whose concentration may be enhanced by O-atom recombination near spacecraft surfaces) and H (whose relative concentrations increase toward the higher orbital altitudes); among the exhaust species not considered is the highly reactive unburned fuel. Internal excitation of the nominally-3000K exhaust gases could also affect the actual chemiluminescent yields, as vibrational enhancement of exhaust reaction rates is known to be important under some conditions. The principles developed here of course apply to an expanded list of reactants/reactions/ products as well as to species desorbed from contaminated spacecraft and rocket surfaces (whose concentrations are enhanced in the ram cloud (Ref 90)).

Table 6.6 identifies the reactions of exhaust species with atmospheric O and N_2 that this analysis indicates are most likely to result in detectable ultraviolet and visible emission. The band systems expected and their wavelength regions are listed in the final column. Those bands that originate from the lowest vibrational state(s) of the electronically-excited species are obviously favored,and therefore the spectral distributions would not necessarily be similar to those under other excitation conditions. Cross sections for excitative collisions with the atmosphere's N_2 molecules are less well understood, but are believed to be less than those with O--which is also considerably more abundant at orbital (and most suborbital) altitudes.

The large (factor >10) uncertainty in the estimates of cross sections at the maximum available kinetic energies is due principally to: 1) extrapolation to ~1-10 eV of bulk rate data taken at fractions of an eV; 2) neglect of the fact that these laboratory rate coefficients might in part refer to reactants in excited levels; and 3) the assumption that cross sections for reactions yielding products in electronically excited states have the same functional form as the corresponding [measured] reactions that yield products in the ground state. "Best-estimates" of the cross sections of interest to optical surveillance of energetic rocket exhaust plumes are on the order of 0.1 A^2--i.e., the probabilities that collisions produce UV or visible photons are very roughly 1% those of elastic collisions, which virtually eliminate further such emission. The reactions listed in Table 6.6 obviously merit particular attention in laboratory and theoretical studies that support planning of spaceborne surveillance systems design.

SECTION 7

ANALYSIS OF GROUNDBASED INFRARED IMAGES OF SHUTTLE ORBITER EXHAUST PLUMES

Introduction

As explained in Section 6, collisions of the near-orbital velocity combustion products of thruster rocket engines with the residual atmospheric gas produce an extended self-luminous plume, which represents a potentially useful signal for remote optical sensing of exo-reentry vehicles and powered earth satellites. Images of the vibrational-bands radiations from such an exhaust interaction volume, taken with a groundbased infrared camera, provide critical information for refining this surveillance-tracking concept. We describe here the radiometric calibration and reduction of a set of such image data, which was used by Air Force Geophysics Laboratory in interpreting the plume's emission distribution and validating CHARM model (Ref 89) calculations of the transport and vibrational excitation of the rocket exhaust gases.

Experiment

The measurements were made (by an AFGL experiment group) with a cryocooled focal plane photodiode array camera in the 1.2 m-aperture reflector telescope at the Air Force Maui Optical Station (AMOS) Observatory located 3055 m above sea level in Hawaii, in connection with an orbit correction maneuver of space shuttle. The vehicle passed north of the ground site in an essentially west-to-east track at a moderately low elevation angle, in "airplane" flight aspect; thus its long axis was about perpendicular to the line of view at its closest approach, when the data described here were taken. Tracking the hard body under radar control, the camera recorded short wavelength-infrared images of 1) the pattern of sunlight diffusely scattered from its outer protective-tiles surface and 2) most of

the exhaust plume that developed from a firing of its aft Reaction Control System engines. (The fraction of the glow volume within the camera's field of view when signal/noise was highest was verified from frames taken after the vehicle had moved further away toward the horizon, when the angle subtended by its plume was smaller.) The solar elevation and azimuth at the spacecraft were 41° and 34° E of S; that is, the sun illuminated its essentially-flat side at an incidence angle of 51° (= arc cos [cos 34° cos 41°]), from behind the telescope-camera.

Figure 7.1 shows the spectral response of the detector array, the transmission of the short wavelength-cutoff filter (also cooled), and the transmission $T_a(\lambda)$ of the atmosphere between AMOS and the radiating targets. The diode response shown (photocurrent per unit irradiance) was provided by AFGL. We extended the filter's transmission characteristic to wavelengths below 2.5 μm with the assumption that it is the same as that of a similar, commercially-available design (Ref 125); in practice, error in the sensor's response to the blue of the 2.7-μm H_2O ν_1 and ν_3 bands have negligible effect on the calculated radiances of the plume, as will become clear shortly. We calculated the atmospheric transmission using LOWTRAN 5 (Ref 126), in PC TRAN mode, for standard clear midlatitude conditions with the usual 23-km sea level visibility. While water vapor concentration soundings that were made near the time of the experiment would lead to a more accurate transmission, small variations in the altitude profile of H_2O would in first approximation introduce the same change in attenuation of the spectrally-continuous referencing radiation from Orbiter's body as from the rotationally broadened vibrational-bands signal from the hot plume; thus (in view of the other errors in the data-reduction procedure) no further correction was applied. (The telescope mirror was assumed to be spectrally flat over the wavelength range in Figure 7.1.)

The diode array camera was operated at the standard video

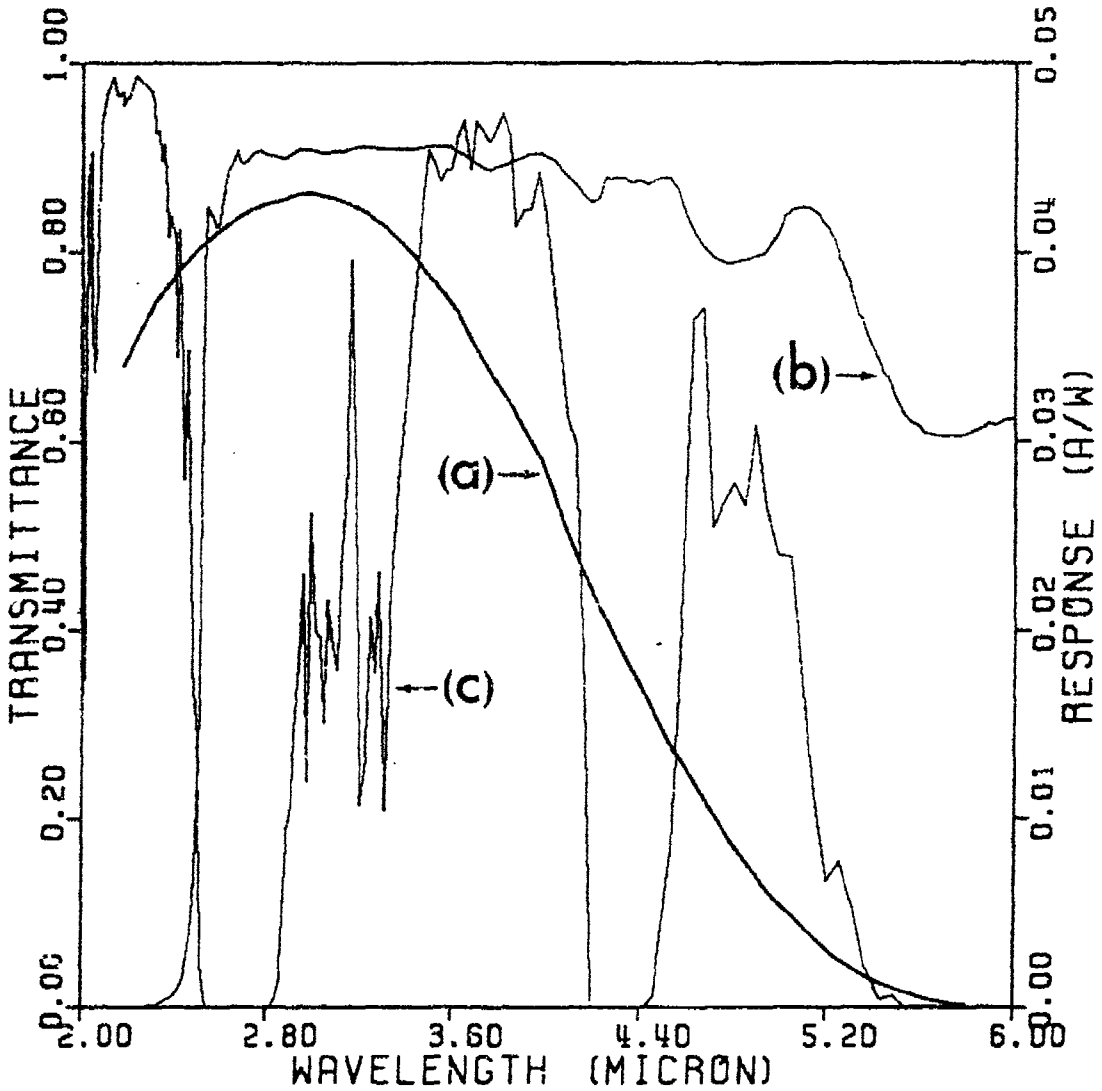

Figure 7.1. (a) Responsivity of the photodiodes; (b) transmission of the long-pass filter; (c) transmission of the intervening atmosphere $T_a(\lambda)$ (from LOWTRAN 5)

framing rate, with automatic background subtraction and compensation for nonuniformity of its response over the image field. The radiance pattern of the plume provided a direct measure of the angle between the exhaust axis and Orbiter's velocity vector, which checked satisfactorily with the known mounting angle of the aft thrusters of its Reaction Control System and its nose-up aspect angle visible in the video images.

Data Reduction

The high concentration of water vapor in the exhaust of the MMH-N_2O_4 thruster engines (Table 6.1), the strong rovibrational-bands radiation from water molecules at the wavelengths to which the groundbased sensor responds (Figure 7.2b), and the known efficient collisional excitation of water vapor at earth-orbital relative velocities (Ref 127), led to the hypothesis that this SWIR glow is due primarily to impact excitation of this species. (The contribution from the other infrared-active combustion products--principally, CO and CO_2--was treated in the final analysis of these image data.) To measure the radiances of the plume in the projection to AMOS, we normalized the telescope-camera's response to the reasonably well understood transmitted surface brightness of Orbiter's sunlit body, correcting for the differences between the emission and scattering spectra by the procedure described here. We then determined the sterance of the plume within the optical system's sensitivity band (and also over the full range of rovibrational wavelengths of hot H_2O), by planimetric analysis of the apparent brightness contours of the glowing volume, correcting for the radiating area that lies outside the camera's field of view.

We assumed the borosilicate tile material to be a Lambertian scatterer with constant albedo over the system sensitivity band indicated in Figure 7.1. The solar spectral irradiance $E_s(\lambda)$ (Figure 7.2a) and the known angle between the sun direction and the spacecraft's long axis then lead directly to the spectral radiance of the tiles $B_s(\lambda)$ outside the

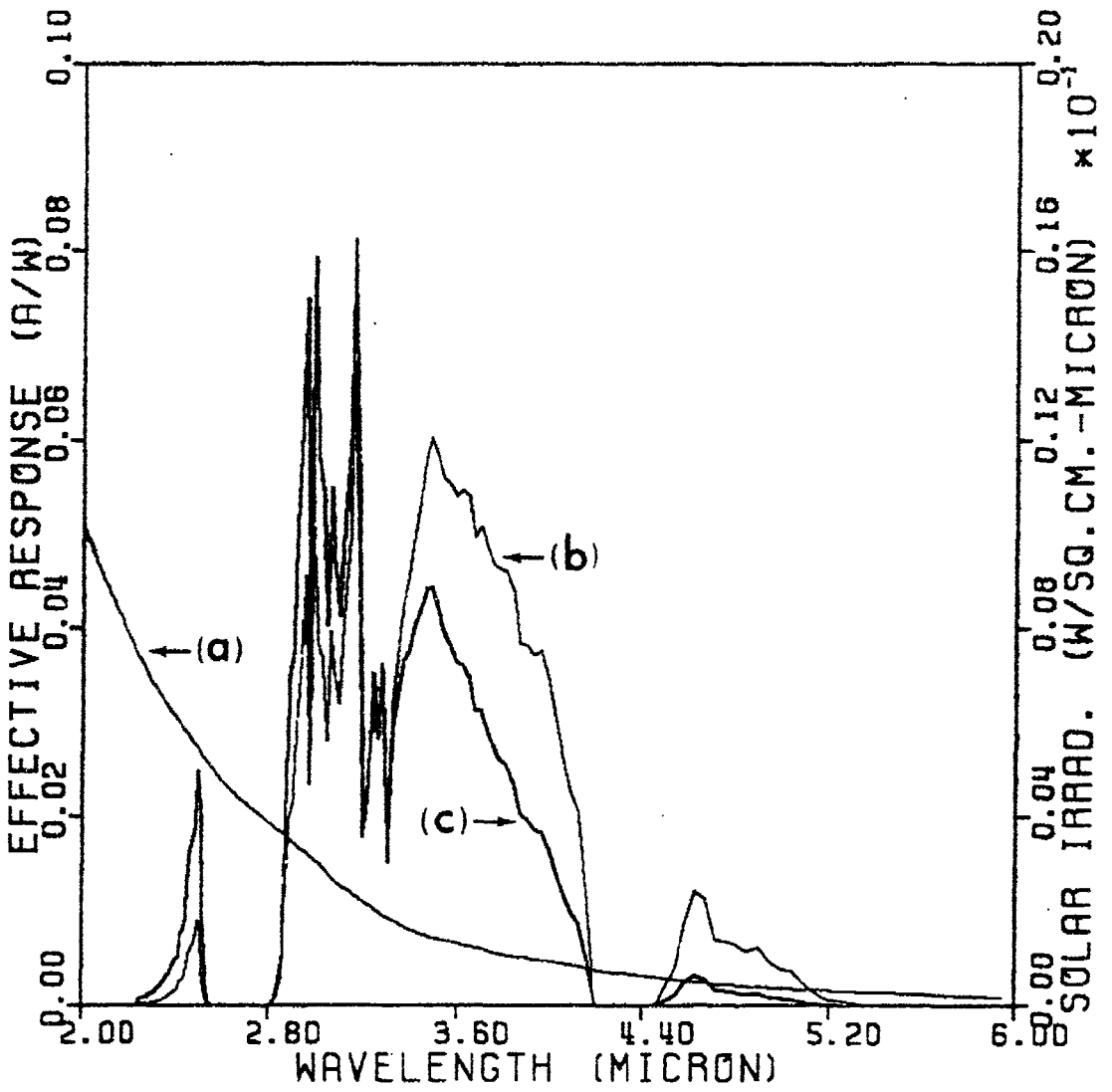

Figure 7.2. (a) Solar spectral irradiance $E_s(\lambda)$ normal to the vector from the sun, from LOWTRAN 5; (b) effective wavelength response of the sensor:--product of atmospheric transmission $T_a(\lambda)$ and sensitivity $S(\lambda)$; (c) product of (a) and (b)

atmosphere. (As expected from Orbiter's actual cross-sectional shape, isophote plots of the sunlit area showed the side of its fuselage to be better approximated as a flat plate than a section of cylinder.) Illumination of the vehicle from thermal earthshine and sunlight scattered from the earth's surface and atmosphere (calculated from LOWTRAN 5) is small compared with that from direct sunlight, except beyond about 5 μm; thus only the solar flux was considered in calculating $B_s(\lambda)$. The wavelength distribution in the signal from the spacecraft body is B_s times the product of the sensor response $S(\lambda)$ {=[photodiode sensitivity] x [filter transmission], shown in Figure 7.1a and b} and the atmospheric transmission $T_a(\lambda)$. The photocurrent from the instantaneous fields-of-view on the sunlight-scattering surface is then directly proportional to $\int B_s(\lambda)S(\lambda)T_a(\lambda)d\lambda$ over the range of wavelengths in Figure 7.2.

Corresponding spectral distributions for the water vapor of the exhaust plume at three rotational temperatures in the expected range, normalized to one another over the wavelength band shown, are in Figure 7.3. The relative emission spectra for 1000K and 3000K were derived from absorption spectra (Ref 128) at pressures near 1 atm, and thus the distributions may be somewhat broader than those from the lower-pressure plume. These data include radiation in the strong ν_2 band at 6.3 μm, $\nu_2 + \nu_3$ at 1.9 μm, and weak $2\nu_2$ (020→000) at 3.1 μm, as well as the familiar ν_1 and ν_3 bands near 2.7 μm. We derived the bands profile shown for 8000K from a (temperature)^{½}-dependence of the absorption band widths, which is both expected from the rotational-lines population development and observed in a plot of the Ref 128 data between 300K and 3000K. A straightforward calculation based on the "variable hard sphere" collision model described in Section 6 indicated that the H_2O molecules reach rotational equilibrium before radiating (their vibrational-state lifetimes are 10-100 millisec), and thus the spectral distribution within each vibrational band can be described with adequate accuracy by a "temperature".

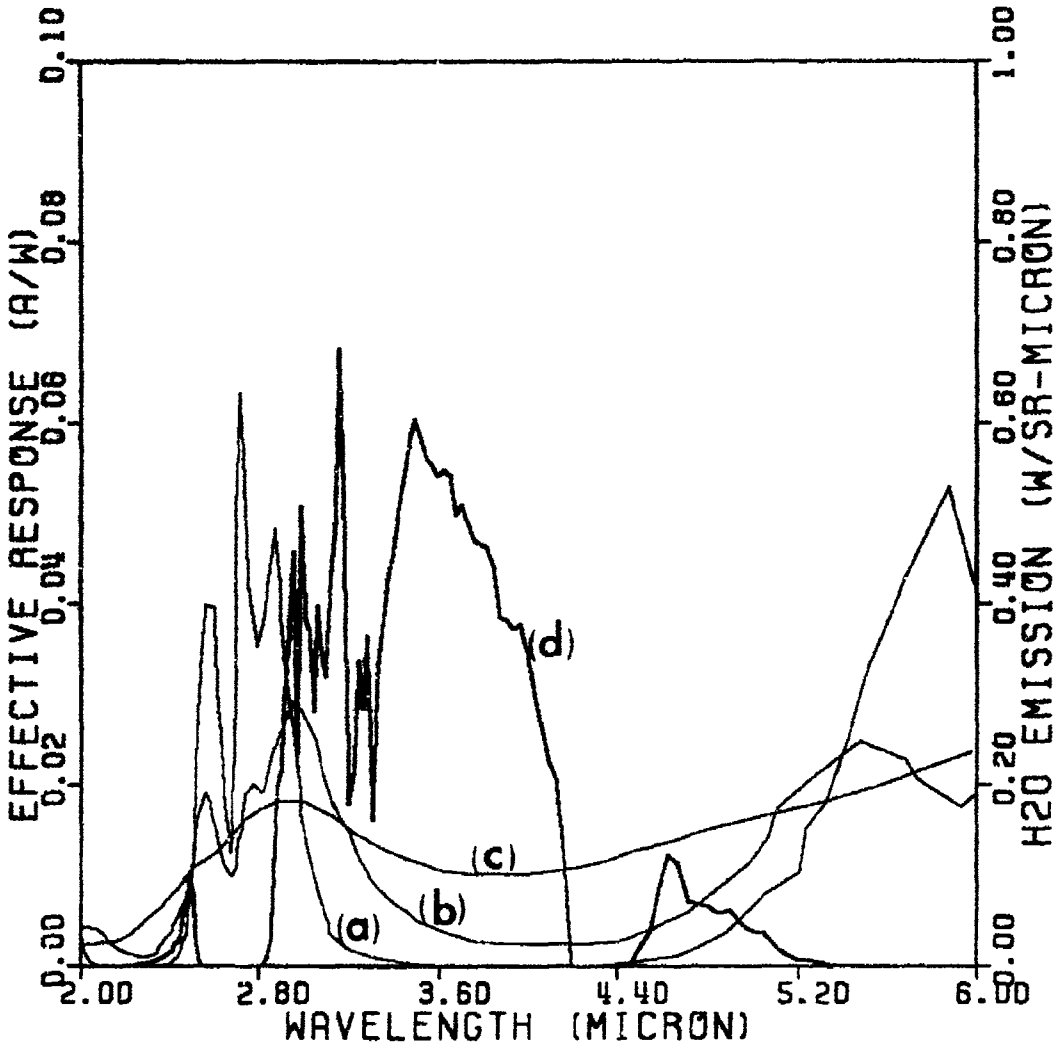

Figure 7.3. Normalized rovibrational band emission profiles of water vapor calculated from H_2O absorption spectra at temperatures (a) 1000K, (b) 3000K, and (c) 8000K, with (d) effective wavelength response $S(\lambda)\ T_a(\lambda)$ of the sensor plus atmosphere

We isolated the emission in the ν_1 and ν_3 bands from the ν_2 and $\nu_2 + \nu_3$ bands--for comparison to CHARM predictions--by manually extrapolating to zero the wings of the "2.7 μm" feature in Ref 128's plots. The resulting integrated band strengths were found to be within 10% of the known absorption strengths of the two spectrally-overlapping transitions (Ref 129) at all temperatures, which indicates the reliability of this simple procedure. We then repeated the procedure to isolate the spectrally-broadened ν_2 band (the data of Ref 128 extend to 8½ μm), adjusting the sum of the two absorption curves to the values shown in the overlap region near 4 μm.

Errors in the short wavelength wing of the "2.7 μm" emission profiles are unimportant due to the camera filter's sharp cutoff near 2.4 μm and the strong neutral-atmospheric absorption between ~2.6 and 2.8 μm. Similarly, error from uncertainty in the long wavelength wing is attenuated by the decreasing responsivity of the detector and the absorption by atmospheric CO_2 (ν_3) near 4.3 μm. We therefore judge that uncertainties in the emission profiles of these vibrational bands contribute less than 15% error to the calculated radiances of the plume outside the atmosphere [at fixed temperature]. Figure 7.4 shows the product of the effective system response $S(\lambda)$ with each of these model water vapor emission profiles.

The photocurrent (per unit etendue of the telescope-camera) that results from the plume's spectral radiance B_p is then proportional to $\int B_p S(\lambda) T_a(\lambda) d\lambda$, where B_p is the product of the wavelength-integrated (i.e., total) radiance and the normalized emission spectrum distributions [in Figure 7.4]. The total radiance (which arises from all the H_2O vibrational features) to be determined by referencing to the sunlight-scattering signal from Orbiter's body can be placed outside the integral. We constructed contour plots of the resulting radiance distribution of the plume outside the atmosphere [in the projection to AMOS] at each model temperature, applying the known relationship between video output voltage and initial photocurrent, the

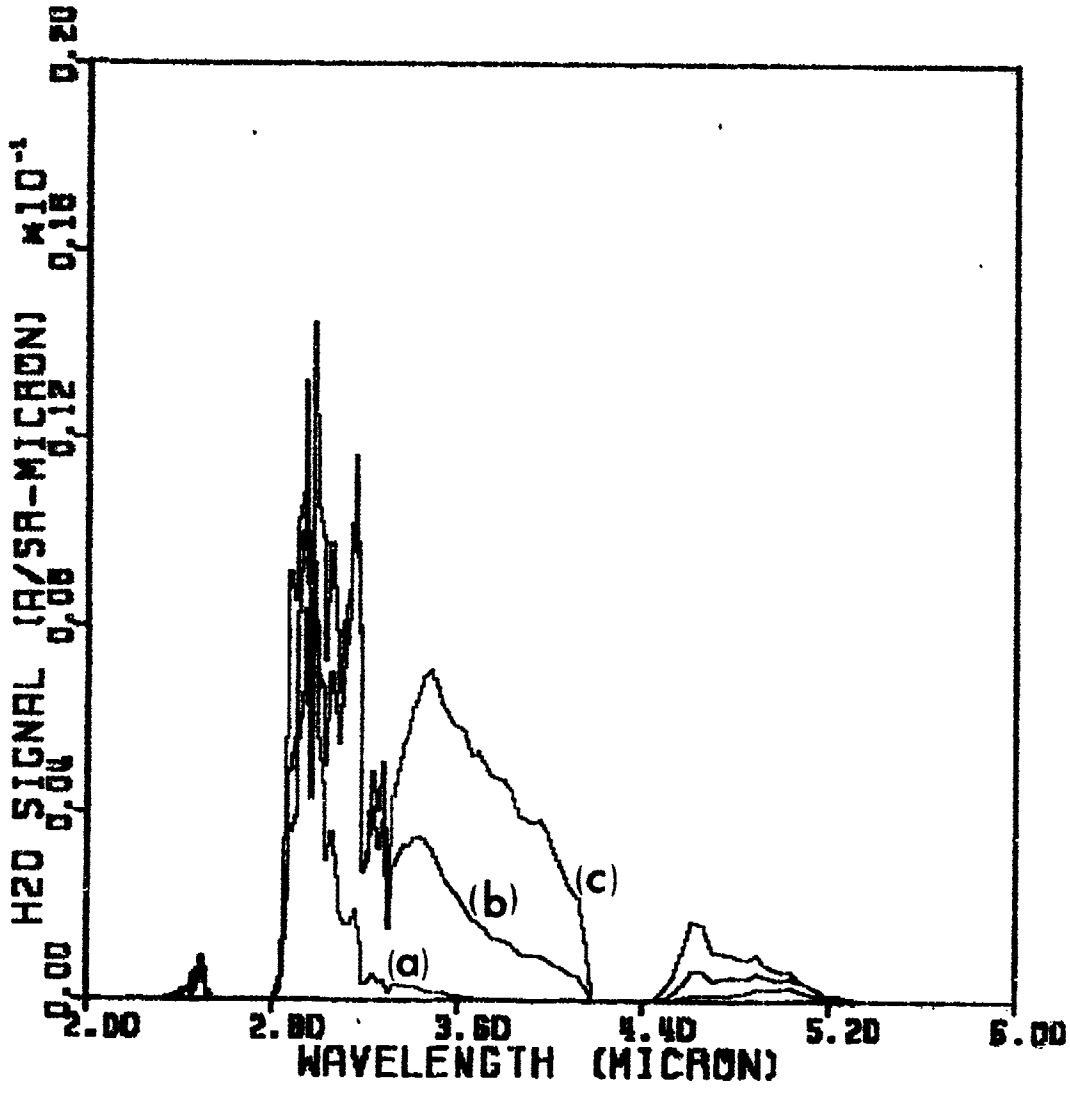

Figure 7.4. Product of effective sensor response function (Figure 7.3d) with the normalized H_2O emission profiles (Figure 7.3 a-c) at radiating temperatures (a) 1000K, (b) 3000K, and (c) 8000K

current from the pixels imaging Orbiter's body provided the absolute reference standard. We then integrated these contours spatially to determine the total sterance of the plume in these H_2O bands from within the camera's field of view, and then corrected this result for the section that lay outside the field as measured in the aforementioned video frames taken when the plume occupied a smaller angle (extending the contours manually). (This conversion from absolute surface-radiance distribution to total photon yield assumes that the exhaust plume is optically thin to its own radiation, which is expected from the relatively low column densities of water vapor.)

To compare the radiances in the 2.7 μm H_2O bands with those predicted by CHARM, we corrected the video data for the contribution from the 6.3 μm band. This involved subtracting out the "isolated" normalized emission profile derived as described above, and applying the CHARM result that these ν_2 radiances (above the atmosphere) are approximately equal to the ν_1 plus ν_3 radiances. The predicted dependence on temperature of the response of the sensor to these transmitted 2.7 μm and 6.3 μm H_2O bands (only) is shown in Figure 7.5. The calculated contribution of 6.3-μm band photons to the total video signal, expressed as a percentage of that due to the 2.7 μm-bands photons, is 5% (±2%), 11% (±5%), and 57% (±25%) for 1000K, 3000K, and 8000K plume temperature respectively. We estimated the combined ~40% error in these contributions from the uncertainties in 1) the ratio of 2.7-μm to 6.3-μm surface brightness adopted from CHARM, 2) our interpretation of the absorption data from which the band profiles were determined (as noted, the information for the ν_2 band extends only to 8½ μm), and 3) our manual assignment of band profiles in the intermediate wavelength region where ν_2 and ν_3-plus-ν_1 strongly overlap (refer to Figure 7.3). The estimated maximum error in the absolute 2.7 μm-band radiance from this source (other systematic and instrumental errors are of course also present) can be seen to be only ~30%, at the highest plume temperature.

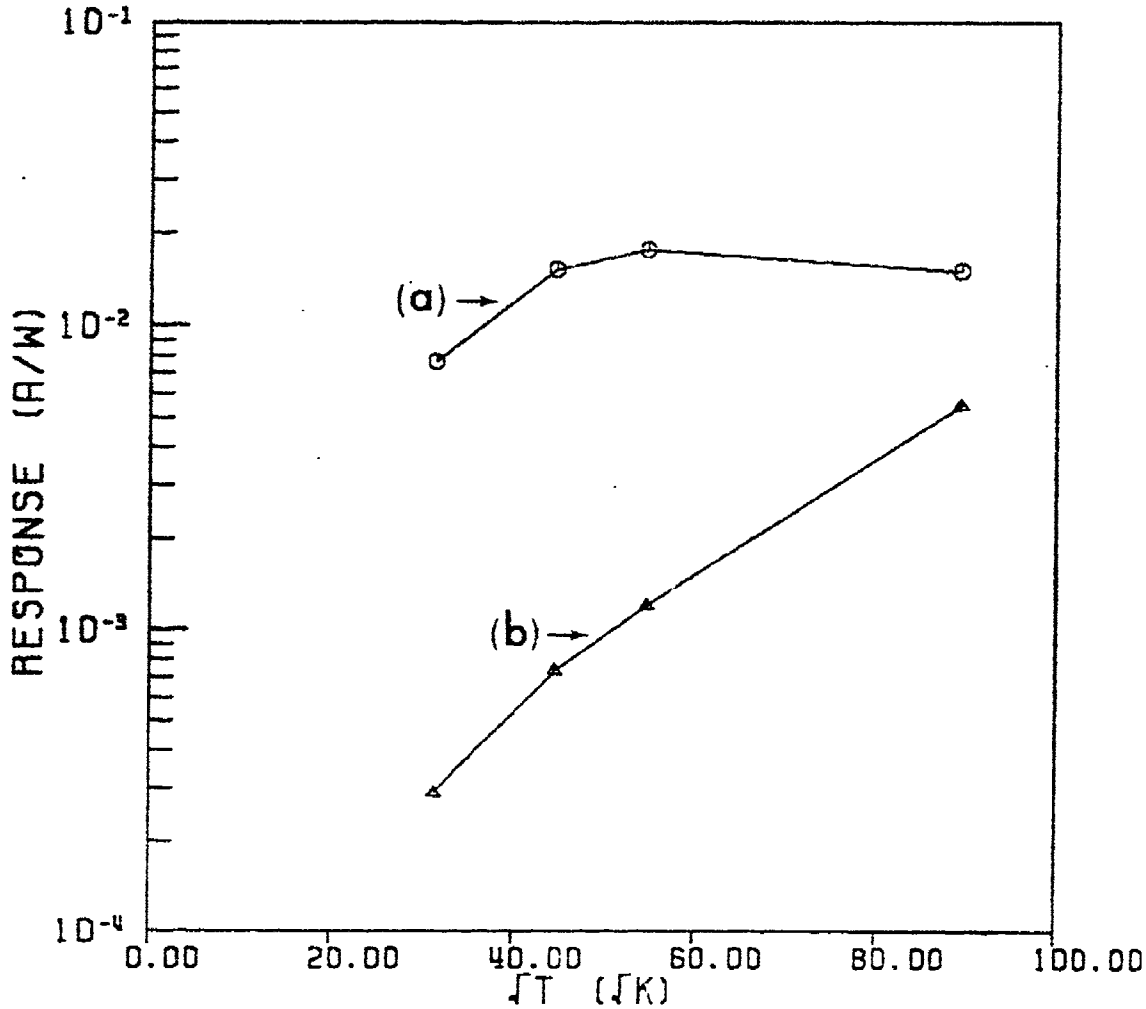

Figure 7.5. Predicted relative response of the groundbased camera to (a) 2.7 μm and (b) 6.3 μm H_2O bands as a function of the rotational temperature T of the plume

Summary

We measured the SWIR radiances and sterance in the exhaust plume of a space shuttle thruster engine imaged by a photodiode array camera in the AMOS telescope, by standardization against the sunlight reflected from Orbiter's body over the same spectral range. The data reduction assumes that the glow luminosity results principally from H_2O molecules collisionally excited in their three vibrational fundamental modes by impact on ambient N_2 and O, a reasonable approximation since water vapor is predicted to constitute 2/3 of the infrared-active combustion products (Table 6.1) and is known to be efficiently internally excited in high-relative energy collisions. Corrections for the radiation from these other species have been applied in the final analysis of these data for comparison to CHARM predictions.

REFERENCES

1. I. L. Kofsky and J. L. Barrett, Spacecraft glows from surface-catalyzed reactions, Planet. Space Sci. 34, 665-681, 1986.

2. I. L. Kofsky and J. T. Brownrigg, Spacecraft glows from surface recombination reactions in LEO, in The Effect of the Ionosphere on Communication, Navigation, and Surveillance Systems (Proceedings of the 5th Ionosphere Effects Symposium, May 1987), ed. J. M. Goodman, Library of Congress 87-619868, pp. 489-498, 1987.

3. I. L. Kofsky and J. L. Barrett, Spacecraft surface glows, Nucl. Inst. and Methods B14, 480-489, 1986.

4. S. B. Mende, G. R. Swenson, K. S. Clifton, R. Gause, L. Leger, and O. K. Garriott, Space vehicle glow measurements, J. Spacecraft Rockets 23, 189-195, 1986.

5. G. R. Swenson, S. B. Mende, and E. J. Llewellyn, The effect of temperature on shuttle glow, Nature 323, 519-522, 1986.

6. J. L. Barrett, I. L. Kofsky, and E. Murad, Ultraviolet glows from recombination on spacecraft surfaces, SPIE Proceedings 687 (Ultraviolet Technology), 28-35, 1986.

7. I. L. Kofsky and J. L. Barrett, Infrared emission from NO_2^* and NO^* desorbed at spacecraft surfaces, J. Spacecraft Rockets 24, 133-137, 1987.

8. I. L. Kofsky, Excitation of N_2 Lyman-Birge-Hopfield bands emission by low earth orbiting spacecraft, Geophys. Res. Lett. 15, 241-244, 1988.

9. I. L. Kofsky and J. L. Barrett, The NO-NO_2 system at laboratory surfaces, in NASA Conference Publication 2391 (Proceedings of the NASA/MSFC Second Workshop on Spacecraft Glow, 6-7 May 1985), ed. J. H. Waite, Jr., and T. W. Moorehead, pp. 165-168, 1985.

10. I. L. Kofsky and J. L. Barrett, Infrared emission from desorbed NO_2^* and NO^*, in NASA Conference Publication 2391 (Proceedings of the NASA/MSFC Second Workshop on Spacecraft Glow, 6-7 May 1985), ed. J. H. Waite, Jr., and T. W. Moorehead, pp. 155-164, 1985.

11. I. L. Kofsky and J. L. Barrett, Surface-catalyzed recombination into excited electronic, vibrational, rotational, and kinetic energy states: A review, in NASA Conference Publication 2391 (Proceedings of the NASA/MSFC Second Workshop on Spacecraft Glow, 6-7 May 1985), ed. J. H. Waite, Jr., and T. W. Moorehead, pp. 149-154, 1985.

12. I. L. Kofsky and J. L. Barrett, Optical emissions resulting from plasma interactions near windward-directed spacecraft surfaces, Proc. AIAA Shuttle Environment and Operations Conference, Oct-Nov 1983, paper 83-2661-CP.

13. I. L. Kofsky, A surface-chemical basis for luminescence excited by spacecraft, Paper PH-A4-4, Canadian Chemical Conference (Saskatoon, Sask.), 1-4 June 1986.

14. I. L. Kofsky, Spectroscopic consequences of Papadopoulos' discharge model of ram glows, Radio Sci. 19, 578-585, 1984.

15. K. Papadopoulos, On the shuttle glow (the plasma alternative), Radio Sci. 19, 571-578, 1983.

16. G. Comsa and R. David, Dynamical parameters of desorbing molecules, Surf. Sci. Rept's 5, 145-198, 1985.

17. G. R. Swenson, S. B. Mende and K. S. Clifton, Ram vehicle glow spectrum: Implications of NO_2 recombination continuum, Geophys. Res. Lett. 12, 97-100, 1985.

18. S. B. Mende, P. M. Banks and D. A. Klingelsmith, III, Observation of orbiting vehicle induced luminosities on the STS-8 mission, Geophys. Res. Lett. 11, 527-530, 1984.

19. J. H. Yee and V. J. Abreu, Visible glow induced by spacecraft-environment interaction, Geophys. Res. Lett. 10, 126-129, 1983.

20. J.-H. Yee, V. J. Abreu, and A. Dalgarno, Characteristics of the spacecraft optical glow, Geophys. Res. Lett. 11, 1192-1195, 1984.

21. J.-H. Yee, V. J. Abreu, and A. Dalgarno, The Atmosphere Explorer optical glow near perigee altitudes, Geophys. Res. Lett. 12, 651-654, 1985.

22. R. R. Conway, R. R. Meier, D. F. Strobel, and R. E. Huffman, The far ultraviolet glow of the S3-4 satellite, Geophys. Res. Lett. 14, 628-631, 1987.

23. M. R. Torr, D. G. Torr, and J. W. Eun, A spectral search for the Lyman-Birge-Hopfield band nightglow from Spacelab I, J. Geophys. Res. 90, 4427-4433, 1985.

24. S. Chakrabarti and T. Sasseen, Investigation of vehicle glow in the far ultraviolet, in NASA Conference Publication 2391 (Proceedings of the NASA/MSFC Second Workshop on Spacecraft Glow, 6-7 May 1985), ed. J. H. Waite, Jr., and T. W. Moorehead, pp. 108-115, 1985.

25. K. Moe and M. M. Moe, The effect of adsorption on densities measured by orbiting pressure gages, Planet. Space. Sci. 15, 1329-1332, 1967.

26. K. Moe, Density and composition of the lower thermosphere, J. Geophys. Res. 78, 1633-1644, 1973.

27. K. Moe and M. M. Moe, The roles of kinetic theory and gas-surface interactions in measurements of upper-atmospheric density, Planet. Space Sci. 17, 917-922, 1969.

28. T. G. Slanger, Deductions from space shuttle glow photographs, Geophys. Res. Lett. 13, 431-433, 1986.

29. B. D. Green and E. Murad, The shuttle glow as an indication of material changes in space, Planet. Space Sci. 34, 219-224, 1986.

30. G. D. Purvis, III, M. J. Redmon, and G. Wolken, Jr., Vibrational excitation from heterogeneous catalysis, J. Phys. Chem. 83, 1027-1033, 1979.

31. J. C. Tully, Dynamics of gas-surface interactions: Reaction of atomic oxygen with adsorbed carbon on platinum, J. Chem. Phys. 73, 6333-6342, 1980.

32. K. M. Evenson and D. S. Burch, Atomic-nitrogen recombination, J. Chem. Phys. 45, 2450-2457, 1966.

33. G. A. Somorjai, Chemistry in Two Dimensions: Surfaces, Cornell, Ithaca NY, pp. 377ff, 1981.

34. P. Caubet, S. Dearden, and G. Dorthe, The specific production of NO ($B^2\Pi_r$) from the recombination of NO on a nickel surface, Chem. Phys. Lett. 108, 217-222, 1984.

35. I. L. Kofsky, Comment on "The specific production of NO($B^2\Pi_r$) from the recombination of NO on a nickel surface" by Caubet, Dearden, and Dorthe, Chem. Phys. Lett. 120, 229-230, 1985.

36. R. R. Reeves, Jr., G. G. Mannella, and P. Harteck, Formation of excited NO and N_2 by wall catalysis, J. Chem. Phys. 32, 946-947, 1960.

37. G. G. Mannella, and P. Harteck, Surface-catalyzed excitation in the oxygen system, J. Chem. Phys. 34, 2177-2180, 1961.

38. P. Harteck and R. R. Reeves, Formation and reaction of the excited O_2 ($A^3\Sigma_u$) molecules, Disc. Faraday Soc. 37, 82-86, 1964.

39. J. Fornier, J. Deson, and C. Vermeil, Photolysis of NO trapped in a rigid matrix at 6K, J. Chem. Phys, 68, 5062-5065, 1978.

40. P. B. Hays, G. Carignan, B. C. Kennedy, G. G. Shepherd, and J. C. G. Walker, The visible airglow experiment on Atmosphere Explorer, Radio Sci. 8, 369-377, 1973.

41. R. W. Pease and A. G. Gaydon, The Identification of Molecular Spectra, Chapman and Hall, London, p. 242, 1965.

42. M. J. Engebretson and K. Mauersberger, The impact of gas-surface reactions on mass spectrometric measurements of atomic nitrogen, J. Geophys. Res. 84, 839-844, 1979.

43. M. J. Engebretson and A. E. Hedin, DE-2 mass spectrometer observations relative to the shuttle glow, Geophys. Res. Lett. 13, 109-112, 1986.

44. F. Kaufman, The air afterglow revisited, in Chemiluminescence and Bioluminescence, ed. M. J. Cormier et al., Plenum, New York, pp. 83-98, 1973.

45. M. F. Golde and F. Kaufman, Vibrational emission of NO_2 from the reaction of NO with O_3, Chem. Phys. Lett. 29, 480-485, 1974.

46. Geophysical Research Letters 12 (No. 2), Cover, Feb 1985.

47. R. D. Kenner and E. Ogryzlo, Orange Chemiluminescence from NO_2, J. Chem. Phys., 80, 1-6, 1984.

48. W. Braun, M. J. Kurylo, A. Kaldor, and R. P. Wayne, Infrared laser enhancement reactions: Spectral distribution of the NO_2 chemiluminescence produced in the reaction of vibrationally excited O_3 with NO, J. Chem. Phys. 61, 461-464, 1974.

49. P. N. Clough and B. A. Thrush, Mechanism of chemiluminescent reaction between nitric oxide and ozone, Trans. Faraday Soc. 63, 915-925, 1967.

50. K. H. Becker, W. Groth, D. Thran, The mechanism of the air-afterglow NO + O → NO_2 + hν, Chem. Phys. Lett. 15, 215-220, 1972.

51. P. N. Clough and B. A. Thrush, Vibrational emission by NO_2 in reaction of nitric oxide with ozone, Trans. Faraday Soc. 65, 23-31, 1969.

52. A. T. Stair, Jr., and J. P. Kennealy, Infrared chemiluminescence and vibraluminescence in the NO-O-NO_2 reaction system, J. Chim. Phys. 64, 124-128, 1967.

53. M. F. Golde, A. E. Roche, and F. Kaufman, Absolute rate constant for the O + NO chemiluminescence in the near infrared, J. Chem. Phys. 59, 3953-3959, 1973.

54. A. Fontijn, C. B. Meyer, H. I. Schiff, Absolute quantum yield measurements of the NO-O reaction and its use as a standard for chemiluminescent reactions, J. Chem. Phys. 40, 64-72, 1964.

55. D. E. Paulsen, W. F. Sheridan and R. E. Huffman, Thermal and recombination emission of NO_2, J. Chem. Phys. 53, 647-657, 1970.

56. G. Herzberg, Infrared and Raman Spectra, Van Nostrand, New York, p. 284, 1945.

57. T. C. Degges and H. J. P. Smith, A High Altitude Infrared Radiance Model, AFGL-TR-77-0271, 30 Nov 1977. ADA059242.

58. S. L. Bernasek and S. R. Leone, Direct detection of vibrational excitation in the CO_2 product of the oxidation of CO on a platinum surface, Chem. Phys. Lett. 84, 401-404, 1981.

59. M. Kori and B. L. Halpern, Vibrational energy distribution of CO in the oxidation of C on Pt, Chem. Phys. Lett. 98, 32-36, 1983.

60. R. P. Thorman, D. Anderson, and S. L. Bernasek, Internal energy of heterogeneous reaction products: Nitrogen atom recombination on iron, Phys. Rev. Lett, 44, 743-746, 1980.

61. F. P. Billingsley, Calculated vibrational-rotational intensities for NO, J. Molec. Spect. 61, 53-70, 1976.

62. G. G. Mannella, R. R. Reeves, Jr., and P. Harteck, Surface catalyzed excitation with N and O atoms, J. Chem. Phys. 33, 636-637, 1961.

63. W. Brennen and P. McIntyre, Vibrational relaxation and electronic mutation of metastable nitrogen molecules generated by nitrogen atom recombination on cobalt and nickel, Chem. Phys. Lett. 90, 457-460, 1982.

64. J. A. Halstead, N. Triggs, A.-L. Chu, and R. R. Reeves, Creation of electronically excited states by heterogeneous catalysis, in Gas-phase Chemiluminescence and Chemiionizations, ed. A. Fontijn, Elsevier, Amsterdam, pp. 307-326, 1985.

65. H.-J. Werner, J. Kalcher, and E.-A. Reinsch, Accurate ab initio calculations of radiative transition probabilities between the $A^3\Sigma_u^+$, $B^3\Pi_g$, $W^3\Delta_u$, $B'^3\Sigma_u$, and $C^3\Pi_u$ states of N_2, J. Chem. Phys. 81, 2420-2431, 1984.

66. F. Gilmore, private communication, 1988.

67. M. R. Torr and D. G. Torr, A preliminary spectroscopic assessment of the Spacelab 1/Shuttle optical environment, J. Geophys. Res. 90, 1683-1690, 1985.

68. R. E. Huffman, F. J. Leblanc, J. C. Larrabee, and D. E. Paulsen, Satellite vacuum ultraviolet airglow and auroral observations, J. Geophys. Res. 85, 2201-2215, 1980.

69. R. R. Meier and R. R. Conway, On the N_2 Lyman-Birge-Hopfield band nightglow, J. Geophys. Res. 88, 4929-4934, 1983.

70. P. D. Tennyson, P. D. Feldman, and R. C. Henry, Search for ultraviolet shuttle glow, COSPAR XXVI, Paper XII.2.4, 1986.

71. E. S. Oran, P. S. Julienne, and D. F. Strobel, The aeronomy of odd nitrogen in the thermosphere, J. Geophys. Res. 80, 3068-3076, 1975.

72. B. D. Green, Atomic recombination into excited molecular states -- A possible mechanism for shuttle glow, Geophys. Res. Lett. 11, 576-579, 1984.

73. N. G. Utterback and B. van Zyl, Low energy ionizing collisions between N_2 and CO beam molecules and CO, N_2, NO, CH_4, and CO_2 target molecules, J. Chem. Phys. 68, 2742-2752, 1978.

74. T. Shimazaki and M. Mizushima, Shuttle glow emissions due to radiative relaxation of highly vibrationally excited NO molecules produced by surface reflection, Proc. AIAA Shuttle and Environmental Operations Conf. II, Houston TX, 1985, paper 85-6098.

75. R. H. Prince, On spacecraft-induced optical emission: A proposed second surface luminescence component, Geophys. Res. Lett. 12, 453-456, 1985.

76. T. G. Slanger, Conjectures on the origin of the surface glow of space vehicles, Geophys. Res. Lett. 10, 130-132, 1983.

77. M. F. Golde and B. A. Thrush, Afterglows, Rept's Prog. Phys. 36, 1285-1364, 1973.

78. M. F. Golde and B. A. Thrush, Vacuum ultraviolet emission by active nitrogen I. The formation and removal of $N_2(a^1\Pi_g)$, Proc. Roy. Soc. Lond. A330, 79-95, 1972.

79. J. Anketell and R. W. Nicholls, The afterglow and energy transfer mechanisms of active nitrogen, Rept's Prog. Phys. 33, 269-306, 1970.

80. K. H. Becker, E. H. Fink, W. Groth, W. Jud, and D. Kley, N_2 Formation in the Lewis-Rayleigh afterglow, Faraday Disc. Chem. Soc. (Lond.), 53, 35-51, 1972.

81. I. Nadler and S. Rosenwaks, Studies of energy transfer processes in triplet states of N_2, I. Energy pooling by vibrationally selected $N_2(A^3\Sigma_u^+, v)$ molecules, J. Chem. Phys. 83, 3932-3940, 1985.

82. P. Weinreb and G. G. Mannella, Effect of oxygen on the surface-catalyzed excitation of nitrogen, J. Chem. Phys. 51, 4973-4977, 1969.

83. T. R. Rolfes, R. R. Reeves, Jr., and P. Harteck, The chemiluminescent reaction of oxygen atoms with sulfur monoxide at low pressures, J. Phys. Chem. 69, 849-853, 1965.

84. A. McKenzie and B. A. Thrush, The kinetics of elementary reactions involving the oxides of sulphur IV. The formation of electronically excited sulphur dioxide on surfaces, Proc. Roy. Soc. A, 308, 133-140, 1968.

85. A.-L. Chu, R. R. Reeves, and J. A. Halstead, Surface-catalyzed formation of electronically excited nitrogen dioxide and oxygen, J. Chem. Phys. 90, 466-471, 1986.

86. G. R. Swenson and R. E. Meyerott, Spacecraft ram cloud atom exchange and N_2 LBH glow, Geophys. Res. Lett. 15, 245-248, 1987.

87. B. Halpern and D. E. Rosner, Chemical energy accommodation at catalyst surfaces, J. Chem. Soc. Faraday Trans. I 74, 1883-1903, 1978.

88. K. J. Laidler, Chemical Kinetics, Chapter 6, McGraw-Hill, New York, 1950.

89. J. B. Elgin, The CHARM Monte Carlo Transition Flow Modules, Report SSI-TR-103, Spectral Sciences, Inc., Burlington MA, 1986.

90. B. A. Mirtov, Disturbances of gaseous medium caused by satellite flight, IGY Annals XII, 372-381, 1958.

91. B. D. Green, G. E. Caledonia, and T. D. Wilkerson, The shuttle environment: Gases, particulates, and glows, J. Spacecraft Rockets 22, 500-511, 1985.

92. J. S. Pickett, G. B. Murphy, W. S. Kurth, C. K. Goertz, and S. D. Shawhan, Effects of chemical releases by the STS3 Orbiter on the ionosphere, J. Geophys. Res. 90, 3487-3497, 1985.

93. H. Trinks and R. J. Hoffman, Experimental investigation of bipropellant exhaust plume flowfield, heating, and contamination and comparison with the CONTAM computer model predictions, in Spacecraft Contamination: Sources and Prevention, ed. J. A. Roux and T. D. McCay, AIAA, New York, 1984.

94. H. Trinks, Bipropellant engines surface contamination and heating effects, AIAA 21st Joint Propulsion Conference, Monterey CA, July 8-10 1985.

95. E. Wulf and U. von Zahn, The shuttle environment: Effects of thruster firings on gas density and composition in the payload bay, J. Geophys. Res. 91, 3270-3278, 1986.

96. I. W. M. Smith, Kinetics and Dynamics of Elementary Gas Reactions, Butterworths, Boston, 1980.

97. A. A. Radzig and B. M. Smirnov, Reference Data on Atoms, Molecules, and Ions, Springer-Verlag, New York, 1985.

98. J. O. Hirshfelder, C. F. Curtiss, and R. B. Bird, Molecular Theory of Gases and Liquids, pp. 1110-1113 and 1212-1215, Wiley, New York, 1964.

99. H. Eyring, J. Walter, and G. E. Kimball, Quantum Chemistry, pp. 351-355, Wiley, New York, 1961.

100. G. A. Bird, Monte-Carlo simulation in an engineering context, Proceedings of the 12th International Symposium on Rarefied Gas Dynamics 74 (Progress in Astronautics and Aeronautics), AIAA, New York, 1981.

101. M. Karplus, R. N. Porter, and R. D. Sharma, Exchange reactions with activation energy. I. Simple barrier potential for (H, H_2), J. Chem. Phys. 43, 3259-3287, 1965.

102. J. C. Polanyi, Some concepts in reaction dynamics, Accounts Chem. Res. 5, 161-168, 1972.

103. a. D. L. Baulch, D. D. Drysdale, D. G. Horne, and A. C. Lloyd, Evaluated Kinetic Data for High Temperature Reactions, Vol. I: Homogeneous Gas Phase Reactions of the H_2-O_2 System, Butterworths, London, 1972.

103. b. D. L. Baulch, D. D. Drysdale, and D. G. Horne, Evaluated Kinetic Data for High Temperature Reactions, Vol. II: Homogeneous Gas Phase Reactions of the H_2-N_2-O_2 System, Butterworths, London, 1973.

103. c. D. L. Baulch, D. D. Drysdale, J. Duxbury, and S. J. Grant, Evaluated Kinetic Data for High Temperature Reactions, Vol. III: Homogeneous Gas Phase Reactions of the O_2-O_3 System, the CO-O_2-H_2 System, and of Sulfur-Containing Compounds, Butterworths, London, 1976.

103. d. D. L. Baulch, R. A. Cox, P. J. Crutzen, R. F. Hampson, Jr., J. A. Kerr, J. Troe, and R. T. Watson, Evaluated kinetic and photochemical data for atmospheric chemistry: Supplement I, J. Phys. Chem. Ref. Data 11, 327-496, 1982.

104. S. H. Lin and H. Eyring, Calculation of the reaction cross section from a rate constant by the method of steepest-descent, Proc. Nat. Acad. Sciences 68, 402-405, 1971.

105. R. L. LeRoy, Relationships between Arrhenius activation energies and excitation functions, J. Phys. Chem. 73, 4338-4344, 1969.

106. K. Morokuma, B. C. Eu, and M. Karplus, Collision dynamics and the statistical theories of chemical reactions. I. Average cross section from transition-state theory, J. Chem. Phys. 51, 5193-5203, 1969.

107. N. Cohen and K. R. Westberg, Chemical kinetic data sheets for high-temperature chemical reactions, J. Phys. Chem. Ref. Data 12, 531-558, 1983.

108. H.-J. Meyer, U. Ross, and Th. Schulze, Observation of activation energies in the chemiluminescent reactions of Sr with Cl_2 and Br_2 at collision energies below 4 eV, J. Chem. Phys. 82, 2644-2649, 1985.

109. B. R. Johnson and N. W. Winter, Classical trajectory study of the effect of vibrational energy on the reaction of molecular hydrogen with atomic oxygen, J. Chem. Phys. 66, 4116-4120, 1977.

110. R. Schinke and W. A. Lester, Jr., Trajectory study of O + H_2 reactions on fitted ab initio surfaces. I. Triplet case, J. Chem. Phys. 70, 4893-4902, 1979.

111. G. C. Light, The effect of vibrational excitation on the reaction of $O(^3P)$ with H_2 and the distribution of vibrational energy in the product OH, J. Chem. Phys. 68, 2831-2843, 1978.

112. G. C. Light and J. H. Matsumoto, Experimental measurement of the rate of the reaction $O(^3P) + H_2(v = 0) \rightarrow OH(v = 0) + H$ at 298K, Int. J. Chem. Kinetics 12, 451-468, 1980.

113. J. H. Birely and J. L. Lyman, The effect of reagent vibrational energy on measured reaction rate constants, J. Photochem. 4, 269-280, 1975.

114. R. D. Levine and J. Manz, The effect of reagent energy on chemical reaction rates: An information theoretic analysis, J. Chem. Phys. 63, 4280-4303, 1975.

115. F. Gilmore, personal communication, 1987.

116. V. N. Kondratiev and E. E. Nikitin, Gas-Phase Reactions: Kinetics and Mechanisms, pp. 48-52, Springer-Verlag, New York, 1981.

117. J. H. Birely and R. J. McNeal, Formation of H(2p) and H(2s) in collisions of 1-25 keV hydrogen atoms with the rare gases, Phys. Rev. A5, 257-265, 1972.

118. J. H. Birely and R. J. McNeal, Lyman-Alpha emission cross sections for collisions of 1-25 keV H^+ and H with CO, CO_2, CH_4, NH_3, J. Chem. Phys. 56, 2189-2194, 1972.

119. B. van Zyl, T. Q. Le, H. Neumann, and R. C. Amme, H + Ar Collisions. I. Experimental charge-production cross sections, Phys. Rev. A15, 1871-1886, 1977.

120. J. G. Pruett, F. R. Grabiner, and P. R. Brooks, Molecular beam reaction of K with HCl: Effect of translational excitation of reagents, J. Chem. Phys. 60, 3335-3336, 1974.

121. J. Geddes, H. F. Krause, and W. L. Fite, Atom-molecule reaction D + H_2 → HD + H studied by molecular beams, J. Chem. Phys. 56, 3298-3307, 1972.

122. T. M. Mayer, B. E. Wilcomb, and R. B. Bernstein, Crossed molecular beam study of the endoergic reaction Hg + I_2 → HgI + I from threshold to 2.6 eV (c.m.), J. Chem. Phys. 67, 3507-3521, 1977.

123. A. R. Clemo, F. E. Davidson, G. L. Duncan, and R. Grice, Translational energy threshold functions for oxygen atom reactions, Chem. Phys. Lett. 84, 509-511, 1981.

124. A. R. Clemo, G. L. Duncan, and R. Grice, Reactive scattering of a supersonic oxygen-atom beam: O + C_2H_4, C_2H_2, J. Chem. Soc. Faraday Trans. 78, 1231-1238, 1982.

125. Corion Corporation (Holliston, MA), Optical Filters and Coatings, Sep 1986.

126. F. X. Kneizys, E. P. Shettle, W. O. Gallery, J. H. Chetwynd, Jr., L. W. Abreu, J. E. A. Selby, R. W. Fenn, and R. A. McClatchey, Atmospheric Transmittance/Radiance: Computer Code LOWTRAN 5, AFGL-TR-80-0067, Feb 1980. ADA088215.

127. T. J. Rieger, K. S. Tait, and H. R. Baum, Atmospheric interaction radiation from high altitude rocket exhausts, J. Quant. Spectr. Rad. Transfer 15, 1117-1124, 1975.

128. C. B. Ludwig, Measurements of the curves-of-growth of hot water vapor, Appl. Optics 10, 1057-1073, 1971.

129. T. Baurer and M. H. Bortner, Defense Nuclear Agency Reaction Rate Handbook, p.11-10, DNA-1948H-Rev 9, June 1983.